Downloaded from orbit.dtu.dk on: Mar 23, 2025

DTU Library

On the Design of Tilting-Pad Thrust Bearings

Heinrichson, Niels

Publication date:
2007

Document Version
Publisher's PDF, also known as Version of record

Link back to DTU Orbit

Citation (APA):
Heinrichson, N. (2007). *On the Design of Tilting-Pad Thrust Bearings*. Technical University of Denmark.

General rights
Copyright and moral rights for the publications made accessible in the public portal are retained by the authors and/or other copyright owners and it is a condition of accessing publications that users recognise and abide by the legal requirements associated with these rights.

- Users may download and print one copy of any publication from the public portal for the purpose of private study or research.
- You may not further distribute the material or use it for any profit-making activity or commercial gain
- You may freely distribute the URL identifying the publication in the public portal

If you believe that this document breaches copyright please contact us providing details, and we will remove access to the work immediately and investigate your claim.

Niels Heinrichson

On the Design of Tilting-Pad Thrust Bearings

Department of Mechanical Engineering
Technical University of Denmark

On the Design of Tilting-Pad Thrust Bearings

©Department of Mechanical Engineering
Technical University of Denmark
by Niels Heinrichson

ISBN 87-90416-22-8

Preface

This thesis is submitted as partial fulfillment of the requirements for awarding the Danish Ph.D. degree. The work has been carried out from August 2003 to October 2006 at the Department of Mechanical Engineering (MEK), Technical University of Denmark (DTU). The project was supervised by associate professor Dr.-Ing. Ilmar Ferreira Santos.

The experimental part of the work was carried out during a four month stay at Alstom Power (Switzerland) Ltd., Hydrogenerator Technology Center, Birr, Aargau, Switzerland. I would like to thank Alstom for the opportunity to use their test facilities. And in particular I would like to thank Dr.-Ing. Axel Fuerst and Dipl.-Ing. Kamil Matyscak for their help and for good discussions during my stay.

Technical University of Denmark
Lyngby, October 2006

Niels Heinrichson

Abstract

Pockets are often machined in the surfaces of tilting-pad thrust bearings to allow for hydrostatic jacking in the start-up phase. Pockets and other recesses in the surfaces of bearing pads influence the pressure distribution and thereby the position of the pivot resulting in the most advantageous pad convergence ratio. In this thesis, a theoretical approach is applied in the attempt to quantify the influence of recesses in the pad surfaces. The recesses may be relatively deep and enclosed as is the case with pockets designed for hydrostatic jacking. Such recesses are characterized by low friction and a small pressure build-up. As in parallel-step bearings the recesses may also have a depth of the same order of magnitude as the oil film thickness. Such recesses are characterized by a strong pressure build-up caused by the reduction of the flow area at the end of the recess.

Numerical models based on the Reynolds equation are used. They include the effects of variations of viscosity with temperature and the deformation of the bearing pads due to pressure and thermal gradients. The models are validated using measurements.

Tilting-pad bearings of standard design are studied and the influences of the bearing length-to-width ratio, pad deformation and injection pocket size are quantified. Suggestions for the design of energy efficient bearings are given. The results show that correctly dimensioned, bearings with oil injection pockets have smaller friction coefficients than bearings with plain pads. Placing the pockets in the high-pressure zones close to the trailing edges of the bearing pads causes a substantial reduction in the friction coefficient. The design of the recess sizes and positions leading to the largest improvements is studied and design suggestions for various pad geometries are given.

Parallel-step bearings theoretically have smaller friction coefficients than tilting-pad bearings. A design of a tilting-pad bearing is suggested which combines the benefits of the two types of bearings in a tilting-pad bearing with inlet pockets. This design results in a substantial reduction of the friction loss. Both this bearing and the bearing design with enclosed recesses in the high-pressure regions of the pads suffer from a higher sensitivity to the position of the pivot. The design of such bearing is therefore no trivial task.

Resumé (in Danish)

Der fræses ofte lommer i overfladerne af skoene i aksiale vippeskolejer for at muliggøre hydrostatisk bæring ved opstart af rotoren. Lommer og andre fordybninger i overfladerne af lejeskoene påvirker trykfordelingen og dermed den position af kippunktet, som giver den mest fordelagtige smørefilmskile. I denne afhandling anvendes en teoretisk fremgangsmåde i et forsøg på at kvantificere indflydelsen af fordybninger i overfladerne af lejeskoene. Fordybningerne kan være relativt dybe og indesluttede i skoens overflade, således som det er tilfældet med lommer, der anvendes til hydrostatisk bæring. Den slags fordybninger er karakteriseret ved lav friktion og en lille trykstigning. Som i Rayleigh-step lejer kan fordybningerne også have dybde af samme størrelsesorden som oliefilmstykkelsen. Sådanne fordybninger er karakteriseret ved en kraftig trykopbygning som følge af reduktionen i strømningsareal ved enden af fordybningen.

Numeriske modeller baseret i Reynoldsligningen er anvendt. De inkluderer effekterne af variationer af viskositeten med temperaturen og deformationer af lejeskoene som følge af tryk og temperaturgradienter. Modellerne valideres ved eksperimenter.

Vippeskolejer af standard design undersøges, og indflydelsen af lejernes længde-til-bredde forhold, skodeformation og størrelsen af lommer til hydrostatisk bæring kvantificeres. Forslag til design af energieffektive lejer gives. Resultater viser, at hvis sko med lommer dimensioneres korrekt, har de lavere friktionskoefficienter end sko uden lommer. Hvis lommerne placeres i højtryksområderne tæt på skoenes bagkanter, kan der opnås en betydelig mindskelse af friktionskoefficienten. Positionen og størrelsen af lommen, som resulterer i de største forbedringer bestemmes og designforslag for forskellige skogeometrier anføres.

Rayleigh-step lejer har en teoretisk lavere friktionskoefficient end vippeskolejer. Der foreslås et design af vippeskolejer, som kombinerer fordelene ved de to typer lejer i vippeskolejer med indløbslommer. Dette design resulterer i en betydelig reduktion af friktionstabet. Både dette leje og lejedesignet med indesluttede lommer i højtryksområderne af skoene lider af højere følsomhed overfor positioneringen af dens sfæriske understøtning. Designet af sådanne lejer er derfor ingen triviel opgave.

Contents

Nomenclature

Latin Symbols

B	pad mean arc length	[m]
c	oil specific heat	[J/kg/K]
d_{Hertz}	diameter of Hertzian pressure distribution	[m]
E	Young's modulus of pad material	[N/m^2]
$F_{friction}$	friction force	[N]
F_z	axial load on bearing	[N]
H	convection heat transfer coefficient	[W/m^2/K]
h	oil film thickness	[m]
h_0	oil film thickness at pivot point	[m]
h_p, h_s	pocket (recess) depth, step height	[m]
h_{le}, h_{te}	oil film thickness at leading edge, trailing edge	[m]
K	pad convergence ratio, $h_{le}/h_{te} - 1$	[-]
k, k_{pad}	oil, pad thermal conductivity	[W/m/K]
k_1, k_2	oil specific constants defining viscosity	[-]
L_{end}	minimum distance between recess and trailing edge	[m]
L_{pad}	pad mean arc length	[m]
L_{piv}	pivot position in the dir. of motion (rectangular pad)	[m]
L_{recess}	length of elliptical recess (minor axis)	[m]
$M_r, M_\theta, M_{r\theta}, M_T$	pad bending, twisting and thermal bending moments	[Nm]
M_{res}	resulting moment at pivot point	[Nm]
$\dot{m}_i, \dot{m}_e$	mass flow into pocket, mass flow out of pocket	[kg/s]
Nu	Nusselt number	[-]
p	pressure	[N/m^2]
p_{inj}	oil injection pressure	[N/m^2]
$\dot{Q}_{gen}$	bearing friction loss	[W]
$\dot{Q}_{gr}, \dot{Q}_{out}$	groove heat loss, heat flow out of the computational domain	[W]
$\dot{Q}_{oil,le}, \dot{Q}_{oil,te}$	heat flow in oil at leading edge, trailing edge	[W]
$\dot{Q}_{cond,p}, \dot{Q}_{gen,p}$	conduction into pocket from the pad, pocket friction loss	[W]
r	radial coordinate	[m]
r_1, r_2	pad inner radius, pad outer radius	[m]
r_{mean}, r_p, r_{piv}	pad mean radius, radius of circular pocket, pivot radius	[m]
Re	recess Reynolds number, $\rho U h_p/\mu$	[-]
S_T	Source term in the 2-dimensional energy equation	[W]

T	temperature	[K]
$T_0, T_a, T_c, T_p, T_{le}$	inlet oil, oil bath, collar, pocket oil, leading edge temperature	[K]
T_{bab}, T_{back}	pad babbitt, pad back temperature (used in 2D calculations)	[K]
t_{pad}, t_{plate}	pad thickness, pad plus support thickness	[m]
U	collar speed at mean radius	[m/s]
u_i, u_e	internal energy in inlet and exit oil to and from the recess	[N]
V_r, V_θ	Kirchhoff shear stresses	[N]
$\dot{V}_{inj}, \dot{V}_{oil}$	injected oil flow, cooling oil flow	[m^3/s]
v_r, v_θ, v_z	velocity components in r, θ and z directions	[m/s]
$\dot{W}_{fric}, \dot{W}_{inj}$	friction work at collar surface, oil injection work	[W]
W_{pad}, W_{recess}	pad width, width of elliptical recess (major axis)	[m]
w	deflection of pad in the direction of z_{pad}	[m]
x_{offset}	offset of pivot from nominal position	[m]
z	coordinate in the direction of film thickness	[m]
z_{pad}	coordinate in the direction of pad thickness	[m]

Greek Symbols

α_r, α_p	roll angle, pitch angle of pad	[rad]
α_{pad}	pad thermal expansion coefficient	[K^{-1}]
η	friction coefficient (Friction force / Load)	[-]
ρ	oil density	[kg/m^3]
θ	angular coordinate	[rad]
θ_0, θ_{piv}	pad angle, pivot angle	[rad]
θ_{recess}	angular position of the centre of the recess	[rad]
μ_0, μ_p	inlet oil, pocket oil viscosity	[Ns/m^2]
ν	Poisson's ratio	[-]
ω	angular velocity of collar	[rad/s]

Nondimensionalised quantities

$\overline{h}$	h/h_0
$\overline{p}$	$ph_0^2/(r_1^2\omega\mu_0)$
$\overline{\dot{Q}}$	$\dot{Q}/(r_1^3\theta_0\omega^2\mu_0)$
$\overline{r}$	r/r_1
$\overline{T}$	T/T_0
$\overline{\dot{V}_{inj}}$	$\dot{V}_{inj}/(h_0 r_1^2\omega\theta_0)$
$\overline{v}_r$	$v_r/(r_1\omega)$
$\overline{v}_\theta$	$v_\theta/(r\omega)$
$\overline{v}_z$	$v_z/(h_0\omega)$
$\overline{\dot{W}}$	$\dot{W}/(r_1^3\theta_0\omega^2\mu_0)$
$\overline{w}$	w/h_0
$\overline{z}$	z/h
$\overline{z}_{pad}$	z_{pad}/t_{pad}

$\overline{\alpha}_r$	$\alpha_r r_1/h_0$
$\overline{\alpha}_p$	$\alpha_p r_1/h_0$
$\overline{\theta}$	θ/θ_0
$\overline{\mu}$	μ/μ_0

Abbreviations

TEHD	Thermo-Elasto-Hydrodynamic Refers to a numerical model considering the combined effects of hydrodynamic pressure generation, viscosity variations due to temperature changes and pad bending due to pressure and thermal gradients in the bearing pad.
THD	Thermo-Hydrodynamic Refers to a numerical model considering the combined effects of hydrodynamic pressure generation and viscosity variations due to temperature changes.
ISO	Isothermal Refers to a numerical model considering the effects of hydrodynamic pressure generation.

Chapter 1

Introduction

1.1 Motivation

Tilting-pad bearings are frequently used in large energy converting machinery (electrical engines, power plants etc.). In hydro power plants tilting-pad thrust bearings are used for carrying the weight of the generators and turbines. The friction in the thrust bearings is responsible for a large amount of the energy losses in hydro power plants.

Operated correctly tilting-pad bearings have an almost infinite lifetime as wear can be completely avoided. Correctly dimensioned the bearings operate in the hydrodynamic lubrication regime and are only subjected to boundary and mixed lubrication if they are loaded at start-up of the rotor. Using hydrostatic jacking for lifting up the rotor at start-up ensures a full oil film at all operating conditions.

Due to the rising energy prices the possibilities of reducing the friction in hydro power plants are receiving increased attention. The energy savings due to reduced friction can often fully depreciate the initial cost of new bearings in few years when retrofitting an existing power plant with new bearings. The long life expectancy of the tilting-pad bearings allow for more intricate bearing low friction constructions at higher initial costs. The reduction of friction is therefore of special interest in the design of large tilting-pad thrust bearings. Research questions which are taken up in the present work are related to the necessity of accurate mathematical modelling of the operating conditions of thrust bearings and to the study of design options reducing the friction.

1.2 Historical Development

The pivot pad bearing was invented by Anthony G. M. Michell in 1905 and independently by Albert Kingsbury in 1910 in a slightly different version. Tilting-pad bearings have the great advantage over fixed incline bearings that the pad convergence ratio $K = \frac{h_{le}}{h_{te}} - 1$ is a function of the position of the pivot only. K is independent of the operating conditions (when thermal effects and side leakage are negligible). The load carrying capacity depends strongly on K and fixed incline bearings therefore do not work well under varying operating conditions. This problem was solved by the introduction of the pivot-pad bearing. A schematic illustration of a tilting-pad thrust bearing is seen in figure 1.1. Michell's construction was based on a line pivot not allowing for radial pivoting. Kingsbury used a

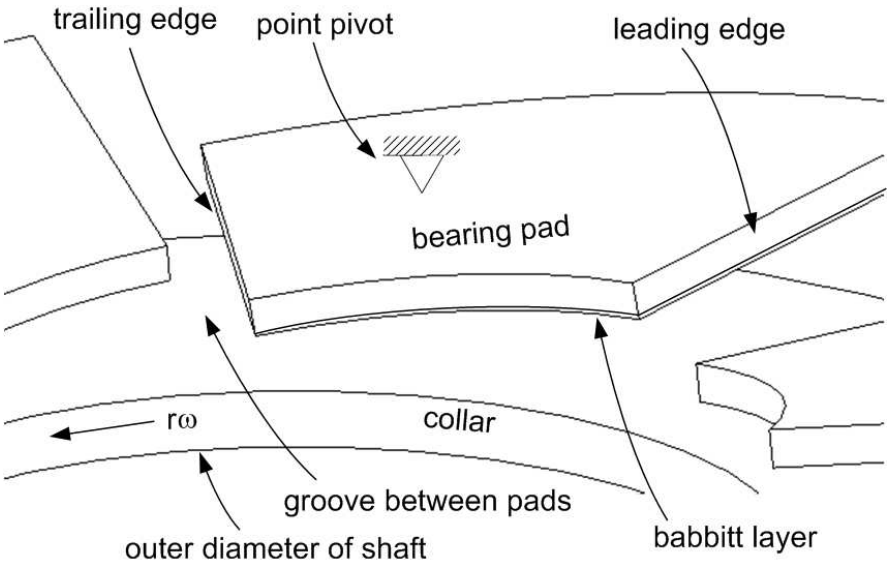

Figure 1.1: An illustration of a tilting-pad bearing and the terminology used in this report.

spherical pivot, which allows the bearing-pad to tilt in all directions to compensate for misalignment between the pad and the rotor. Due to this additional advantage of Kingsbury's design the spherically pivoted bearing is in more widespread use and it is the type of pivot pad, which is considered in this report.

The present day bearing designs are very similar to the original design. In figure 1.2* some examples of modern tilting-pad thrust bearings are shown. To enhance the performance some modifications of the design have been introduced over the years. Levelling systems have been introduced to ensure equal loads on all pads. In large bearings crowning of the pads due to thermal gradients between the oil film side and the backside of the pads may constitute a problem due to a negative influence on the oil film thickness distribution. In order to reduce thermal crowning circular supports, internal cooling of the pads or sandwich constructions have been introduced by bearing designers. Other designers have eliminated the pivot and positioned the pad on a bed of springs allowing for a thinner pad in which the thermal deflection is opposed by pressure bending induced by the springs. Traditionally, bearings are operated in an oil bath under fully flooded conditions. In slow speed bearings movement of the oil in the oil bath does not induce a large energy loss. In high-speed bearings however the churning loss may constitute a significant part of the total friction loss. In such bearings oil is often directly sprayed onto the collar in the groove between the pads or supplied through leading edge grooves. In large applications starting up a loaded rotor from zero velocity causes high temperatures to develop due to dry friction and the white metal surface may melt. To avoid this, hydrostatic jacking is often used. In recent years attention has turned to using polymer materials such as Polyetheretherketones (PEEK) as coating materials instead of white metal because of their low friction coefficients against steel. Hydrostatic jacking may then be avoided.

*The top row pictures are downloaded from the internet: left: www.kingsbury.com/pdfs/catalog-leg.pdf, middle: www.waukbearing.com/_data/page/550/CQ.pdf, right: www.michellbearings.com/product/images/bearing.jpg, The bottom row pictures are curtesy of: Alstom Power (Switzerland) Ltd.

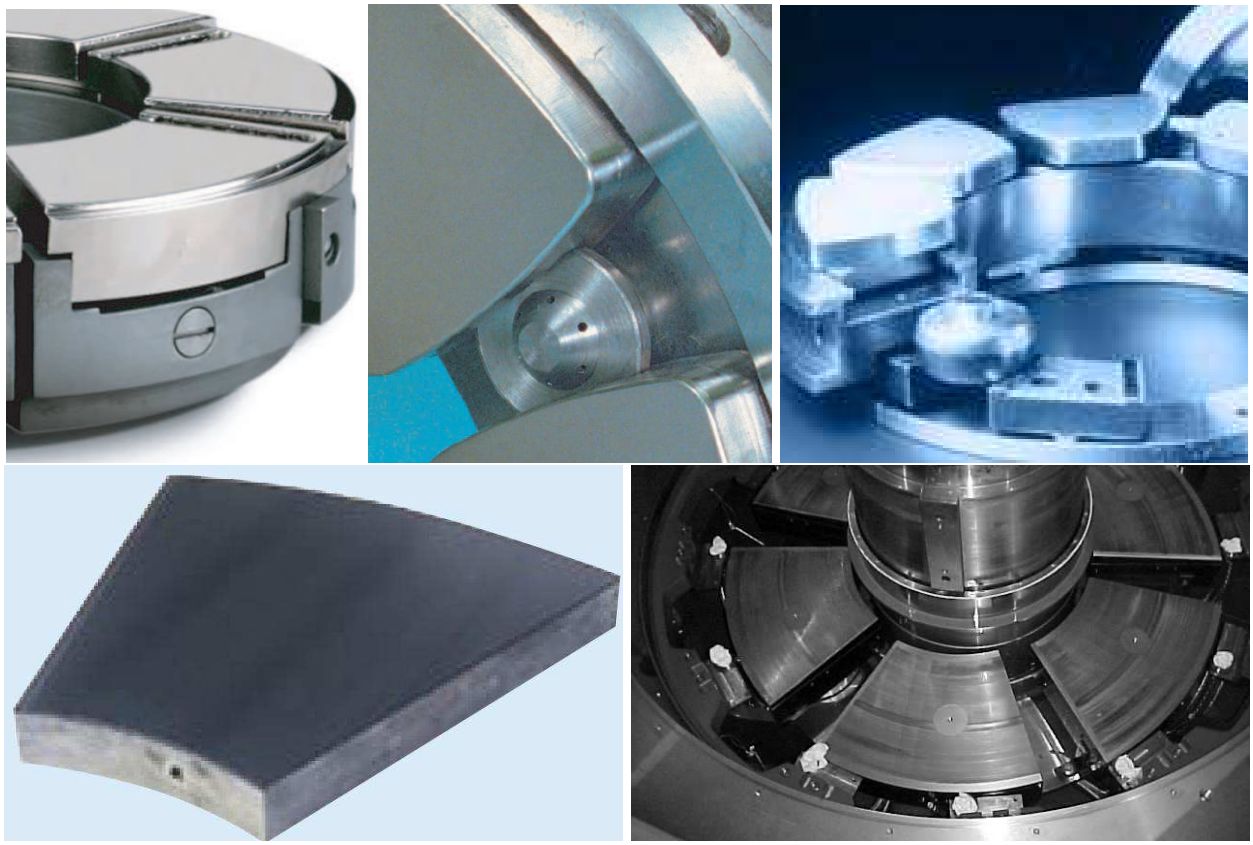

Figure 1.2: Thrust bearings with different features: Leading edge grooves(top left), spray lubrication(top middle), load equilization(top right), PEEK coated pad (bottom left), oil injection pockets (bottom right) .

The improvements in the design of tilting-pad thrust bearings have been aided by the developments in the theoretical description. The analyses of hydrodynamic thrust bearings have predominantly been based in the Reynolds equation (Reynolds, 1886) for the pressure distribution. With the increasing capacity of computers numerical models have been developed including the influences of viscosity variations along and across the lubricating film (Sternlicht et al., 1961; Huebner, 1974b; Fust, 1981; Kim et al., 1983) and the inclusion of the deformation of the bearing pads due to pressure and thermal gradients (Sternlicht et al., 1961; Ettles, 1976, 1980; Pistner, 1996). Heat transfer phenomena have been analysed (Ettles, 1976; Vohr, 1981; Heshmat & Pinkus, 1986; Ettles & Anderson, 1991) and the influence of turbulence in high speed bearings (Huebner, 1974a; Capitao, 1974; Jeng et al., 1986; Hashimoto, 1990) has been studied.

1.3 Objectives and Contributions

The influence of certain design features on the operating conditions of tilting-pad thrust bearings have only been treated peripherally in the scientific literature. Leading edge tapers are sometimes used to assist the build-up of the oil film during start-up. Oil injection pockets may be machined

in the pad surfaces at the pivot points in order to facilitate hydrostatic jacking at start-up. These are features which influence the pressure distribution and thereby the oil film thickness. The works presented in the scientific literature dealing with the combined effects of hydrodynamic pressure build up, temperature variations and deformations of the pads assume sector shaped pads without cutouts in the surfaces. The interest in accurately determining the operating conditions of tilting-pad thrust bearings and the desire to reduce the friction lead to the following research questions:

The first research question which is taken up, deals with the influence of oil injection pockets on the operating conditions and dimensioning of tilting-pad thrust bearings.

The second research question is concerned with, whether improvements in the performance, i.e. a lower friction coefficient and higher load carrying capacity can be achieved by applying features like deep or shallow cutouts in the surfaces of the bearing pads.

In order to answer these questions a numerical model is developed. It includes the components developed in the past, i.e. hydrodynamic pressure build up, temperature variations along and across the lubricant film and bearing pads and the deformation of the pads due to pressure and thermal gradients. It includes options to vary the geometry of the surfaces of the pads so that inlet pockets and enclosed pockets of various geometry, size and depth can be studied. The model also allows for injection of oil in the surfaces of the pads, such as it is used for hydrostatic jacking.

The focus of the work is on reducing the friction. The friction force in a tilting-pad bearing can be quantified as the shear stress in the lubricating oil at the rotor surface integrated over the rotor surface area. Many approaches can be taken in the search for ways to reduce the friction loss. Designing bearings capable of operating at lower lubricant film thicknesses and thereby reducing the bearing area, choosing a lubricant with improved physical properties or changing the lubricant supply method (New, 1974; Mikula & Gregory, 1983; Mikula, 1988) are approaches which can lead to lower friction coefficients. In the present report the focus is limited to the design of the bearing pads. Parameters such as the oil properties, oil film thickness and thermal conditions are considered given by the design specifications. The attention is on correctly dimensioning pads of standard design for small friction coefficients and on suggesting modifications to the design, which result in further reductions of the power loss.

The major contributions of this work relate to the following:

- The elaboration of a numerical model based on the Reynolds equation extends three dimensional thermo-elasto-hydrodynamic (TEHD) analysis of tilting-pad thrust bearings to include the effects of high pressure injection and recesses in the bearing pads.
- The validation of the model through experiments. Apart from predicting the behaviour of tilting-pad thrust bearings to the same level of accuracy as similar models published in the scientific literature it is shown that the model can predict the behaviour of bearings with enclosed recesses. The ability of the model to predict the start-up behaviour of bearings subjected to hydrostatic jacking is similarly validated.

- Combining the parallel-step bearing with the tilting-pad bearing in a design with inlet pockets coverings 60-80 % of the surface areas is suggested. Provided the pivot is positioned correctly the modified bearing pads operate at lower friction coefficients than standard pivot-pad bearings.

- Machining a deep recess (one or more orders of magnitude deeper than the oil film thickness) in the surface of a bearing pad creates a low friction zone inside the pad. It is shown that a substantial reduction in friction compared to conventional bearing designs is possible when designing tilting-pad bearings with deep recesses in the high pressure regions. Design charts are presented stating recess dimensions, recess positions and the corresponding pivot locations leading to small friction coefficients.

1.4 Organisation of the Report

The outline of the thesis is as follows:

Chapter 2: Describes and derives the mathematical models which are used to study tilting-pad thrust bearings. The models are based in the Reynolds equation and employ 2- or 3-dimensional treatment of the temperature distribution in the oil film and in the pad. Whether 2- or 3-dimensional modelling is used depends on the geometry of the studied lubricant flow.

Chapter 3: The models derived in chapter 2 are validated against measurements published in the scientific literature for a bearing with a plain pad surface. Furthermore, a case study of a large sized bearing with oil injection pockets at the pivot points is performed. Oil film thickness measurements are available for comparison. A study of the sensitivity of the bearing operating conditions to the pocket dimensions is performed.

Chapter 4: Measurements of oil film thickness and pressure profiles at four different radii are performed on individual pads in a test-rig. A pad with a leading edge taper and a conical oil injection pocket are measured at various operating conditions. A plain pad is measured for reference. The measurements are compared to theoretical results and serve to validate the numerical model with respect to the description of the pressure changes in the pocket area.

Chapter 5: This chapter studies tilting-pad thrust bearings of standard design. The influence of oil injection pockets placed at the pivot point as well as the influence of thermal bending on the optimal positioning of the pivot point is studied. Furthermore, the influence of the pad length-to-width ratio on the bearing power loss is investigated.

Chapter 6: Correctly designed parallel-step bearings have smaller friction coefficients than tilting-pad bearings. The possibility of designing a bearing combining the good qualities of the two types of bearings is investigated. It is suggested to machine a shallow inlet pocket in the surfaces of the bearing pads. It is shown that a substantial reduction in the power loss can be achieved.

Chapter 7: Deep low friction recesses are introduced in the bearing pads. The recesses create low friction zones in the high pressure region of the pads. It is shown that a substantial reduction in the friction loss can be achieved if the pads and the recesses are correctly dimensioned.

Chapter 8: Summarises the research presented in the report and outlines the main conclusions.

Chapter 2

Mathematical Modelling

The analysis of lubrication problems is usually based on the Reynolds equation which can be derived through an order of dimension analysis from the Navier-Stokes equations. If only the lowest order terms are retained, these can be introduced in the continuity equation which is then integrated across the fluid film to give the Reynolds equation. This was first shown by Reynolds (1886) for a fluid with constant properties. Various researchers have since extended the equation to include compressibility and variations in fluid properties along or across the fluid film. Notably, Dowson (1962) introduced a general extension of the equation to include varying fluid properties both along and across the fluid film. The energy equation similarly reduced to contain only the lowest order terms may be solved for the temperature distribution. It is common practice to use a 2-dimensional flat plate approximation to calculate the bending of the bearing pads stemming from pressure and thermal gradients. Models which include the combined effects of hydrodynamic pressure generation, viscosity variations due to temperature changes and pad bending are termed thermo-elasto-hydrodynamic (TEHD) models.

Many authors have dealt with modelling of hydrodynamic thrust bearings. Sternlicht et al. (1961) presented the first 2-dimensional TEHD analysis of a pivoted thrust pad assuming adiabatic conditions and laminar flow. Design charts (Raimondi & Boyd, 1955; Sternlicht & Arwas, 1962) based on 2-dimensional isothermal and TEHD calculations are still used in bearing analysis today. Models including 3-dimensional treatment of the oil temperature include (Huebner, 1974b; Kim et al., 1983; Ettles & Anderson, 1991). Vohr (1981) presented a model for predicting the operating temperature and leading edge temperature.

The influence of turbulence in tilting-pad-thrust bearings has been studied (Capitao, 1974; Jeng et al., 1986; Hashimoto, 1990). Capitaos 2-dimensional work predicts twice the load carrying capacity and three times the power loss as would have been predicted through pure laminar modelling. It is generally accepted that the flow can be considered laminar for a modified Reynolds number $\mathfrak{R}_x = \rho_0 u_0 h_0^2/(\eta_0 l_0) < 1$.

With the increasing focus on hybrid journal bearings, models of such bearings have been presented in recent years (San Andres, 1995; Santos & Nicoletti, 1999). They treat temperature as a bulk flow property. The flow pattern in bearing pockets and its influence on the pressure distribution has been investigated by the use of Navier-Stokes equation solvers (Ettles & Donoghue, 1971; Braun & Dzodzo, 1995; Helene et al., 2003; Brajdic-Mitidieri et al., 2005). Shinkle & Hornung (1965) showed experimentally and numerically that the pocket flow can be considered laminar for $Re < 1000$. The influence of pocket size in a centrally pivoted bearing was investigated by Hemmi

& Inoue (1999) using an isothermal model.

Some flow phenomena which occur in bearings are not convincingly treated by the Reynolds equation. Stagnation of oil at the leading edge of a pad creates an inertial pressure rise in front of the leading edge (Heckelman & Ettles, 1987; Rhim & Tichy, 1989; Kim & Kim, 2002). Similarly, the changes in flow velocity inside a recess in a bearing pad create inertial pressure changes which are neglected using the classical simplifications employed in lubrication theory (Ettles & Donoghue, 1971). Due to such limitations there is a trend towards employing Navier-Stokes equation solvers in the analysis of bearing fluid flow. The majority of such studies have been isothermal and restricted to the study of fixed geometry flows. The studies have served the purpose of studying isolated phenomena such as inertial effects in hydrostatic injection flows. A number of these studies were mentioned in the previous paragraph. No analysis using Navier-Stokes equation solvers has been performed for the purpose of determining the operating conditions of full tilting-pad bearings. At present the computational effort necessary to analyse problems involving long thin oil films, temperature changes and the movement and bending of the solid surfaces renders the use of 3-dimensional flow modelling very time consuming.

In recent years some focus in the theoretical description of bearings has turned to the description and inclusion of inertial effects. It has been proposed to include local effects of inertia at fluid film thickness discontinuities, for instance at the step in a parallel-step bearing, in a Reynolds equation formulation of the flow problem. Arghir et al. (2002) applied the approach to an oil lubricated double incline step bearing. In a parallel-step bearing the concentrated inertia effect results in a pressure drop at the step because of the acceleration of the fluid at the step. Dobrica & Fillon (2006) applied the approach to a 3-dimensional THD-model of such a bearing of 64 cm^2 surface area operating using a VG32 oil at U=30 m/s and a minimum oil film thickness of 20 μm. Their results showed a pressure drop at the step due to concentrated inertia of 1 % of the maximum pressure. This affects the characteristics of the bearing very little. At higher speeds the effects are larger. No comparative study between experimentally and theoretically determined pressure distributions validating the accuracy of including inertia by a concentrated inertia approximation has been published.

Experimental work on micro texturing have shown a potential for improving the load carrying capacity by the inclusion of shallow recesses in the surfaces of bearings, seals and cylinder liners (Etsion & Klingerman, 1999; Etsion et al., 2004). Recently, Glavatskikh et al. (2005) presented measurements showing a reduction in friction and higher oil film thickness when equipping a tilting-pad thrust bearing with texturing. Arghir et al. (2003) showed that inertial effects are instrumental in improving the load carrying capacity and in textured bearings can therefore not be analysed using the Reynolds equation.

In the work presented in this report a Reynolds equation formulation of the flow problem is applied. All effects of inertia are neglected.

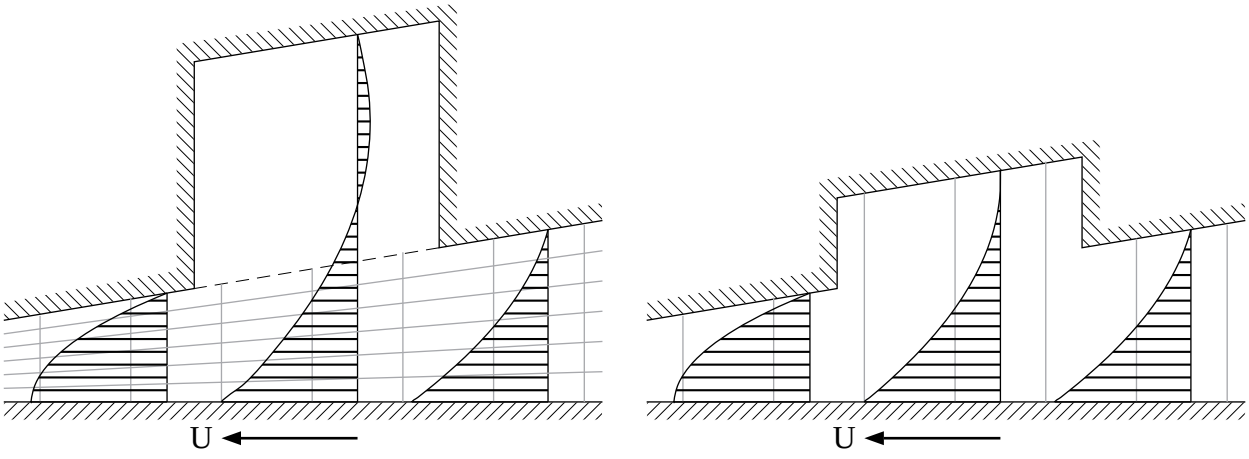

Figure 2.1: Illustration of the flow phenomena in the recess areas. Left: A bearing with a deep recess (3-dimensional grid). Right: A bearing with a shallow recess (2-dimensional grid).

2.1 Levels of Modelling

Models of different levels of detail are used in this report. 1-dimensional models* for pressure are used in places to examine the potential of a specific geometry. 2-dimensional models for pressure are used in isothermal versions (ISO) or including 2-dimensional temperature calculations (2D-THD) and with the calculation of 2-dimensional thermal bending of the pad (2D-TEHD). 2-dimensional models for pressure are used including 3-dimensional temperature calculations (3D-THD) and with the calculation of 2-dimensional thermal bending of the pad (3D-TEHD). The 3-dimensional models yield a more detailed picture of the temperature distribution than the 2-dimensional models. Heat transfer phenomena can thereby be determined more accurately. Furthermore, the thermal bending of the pad is much more accurately determined.

In the remainder of this report recesses of different depth are studied. They can be divided into two categories which have different properties. A class of recesses termed “deep recesses” are considered. The depths of the deep recesses are generally two or more orders of magnitude larger than the oil film thickness. Another class of recesses are termed “shallow recesses”. The depths of the shallow recesses are of the same order of magnitude as the oil film thickness. Flow wise the two classes of recesses differ in that there is recirculation flow in the deep recesses while no recirculation in the shallow recesses is predicted by the Reynolds equation. Figure 2.1 schematically shows the two different flow situations.

In the studies performed on deep recesses the recesses are enclosed in the bearing surfaces and they have a relatively small surface area (< 20 %) compared to the total bearing area. The recirculation in a deep recess results in a large amount of mixing of the oil in the volume of the recess. Therefore, the temperature inside the volume of the recess is considered uniform. A 3-dimensional description of the temperature is used in the oil film outside of the recess area. This is schematically shown in figure 2.1(left). A 3-dimensional treatment of the temperature inside

*The equation set used in the 1-dimensional models is not given in this report. The description and derivation of 1-dimensional models can be found in for instance Hamrock et al. (2004).

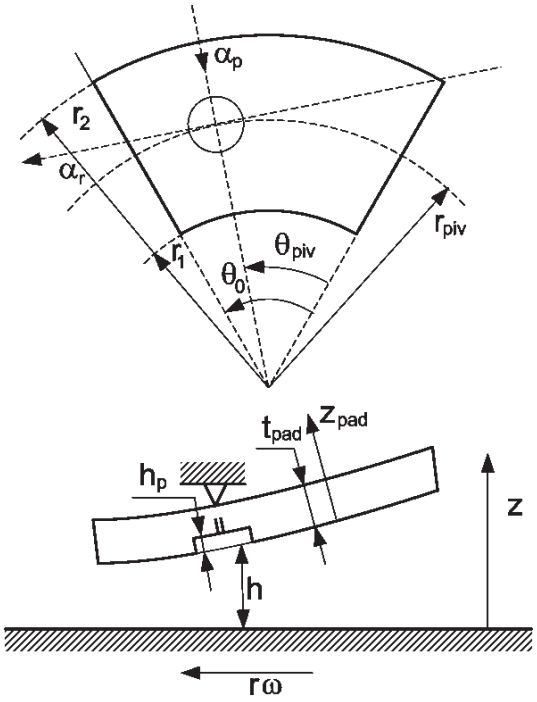

Figure 2.2: The coordinate system used for the 3-dimensional calculations.

the recess area would involve a large effort in the construction of the computational grid, raise the computation time and make it difficult to study recesses of various geometries.

In the studies involving shallow recesses the fluid inside a recess does not mix as it does in a deep recess. The assumption of a uniform recess temperature is therefore not valid. A 3-dimensional formulation would require a grid which stretches into the volume of the recess. A grid as seen in figure 2.1(left) which is stretched with the oil film thickness does not deal well with oil film thickness discontinuities. A more intricate grid is necessary. This would restrict the study of various recess geometries. It is therefore chosen to use a 2-dimensional formulation in which the energy equation is integrated over the thickness of the oil film.

In section 2.2 the derivation of a 3-dimensional formulation is elaborated. Subsequently in section 2.3 the equation set is reduced to a 2-dimensional formulation.

2.2 Governing Equations (3-dimensional formulation)

The bearing is assumed to be operated using a Newtonian and incompressible fluid and under conditions where the flow is laminar and body forces and effects of inertia are negligible. Viscosity is considered to vary with temperature only. All other fluid properties are considered constant. The 3-dimensional formulation is employed for deep recesses when there is recirculation in the volume of the recess. The recirculation results in a large amount of mixing of the oil in the volume of the recess. The temperature inside the volume of the injection recess is considered uniform. Figure 2.2 shows the coordinate system used. The governing equations are nondimensionalised using the

following variable transformations:

$$\overline{\theta} = \frac{\theta}{\theta_0}\ ,\ \overline{r} = \frac{r}{r_1}\ ,\ \overline{z} = \frac{z}{h}\ ,\ \overline{z}_{pad} = \frac{z_{pad}}{t_{pad}}\ ,\ \overline{h} = \frac{h}{h_0}\ ,\ \overline{w} = \frac{w}{h_0}\ ,\ \overline{\alpha}_r = \alpha_r \frac{r_1}{h_0}\ ,$$
$$\overline{\alpha}_p = \alpha_p \frac{r_1}{h_0}\ ,\ \overline{v}_r = \frac{v_r}{r_1\omega}\ ,\ \overline{v}_\theta = \frac{v_\theta}{r\omega}\ ,\ \overline{v}_z = \frac{v_z}{h_0\omega}\ ,\ \overline{\mu} = \frac{\mu}{\mu_0}\ ,\ \overline{T} = \frac{T}{T_0}\ ,$$
$$\overline{p} = \frac{p h_0^2}{r_1^2\omega\mu_0}\ ,\ \overline{\dot{V}}_{inj} = \frac{\dot{V}_{inj}}{h_0 r_1^2\omega\theta_0}\ ,\ \overline{\dot{Q}} = \frac{\dot{Q}}{r_1^3\theta_0\omega^2\mu_0}\ ,\ \overline{\dot{W}} = \frac{\dot{W}}{r_1^3\theta_0\omega^2\mu_0} \tag{2.1}$$

2.2.1 Fluid film

Subject to the standard reductions and boundary conditions applied in fluid film lubrication, the momentum equations are integrated twice across the oil film to give the velocity components in the $\overline{\theta}$- and $\overline{r}$-directions. The $\overline{z}$ component is determined using the continuity equation.

$$\overline{v}_\theta = \frac{\overline{h}^2}{\theta_0\overline{r}^2}\frac{\partial\overline{p}}{\partial\overline{\theta}}\int_0^{\overline{z}}\frac{\overline{z}d\overline{z}}{\overline{\mu}} - \left(\frac{1}{\overline{F}_0} + \frac{\overline{h}^2}{\theta_0\overline{r}^2}\frac{\partial\overline{p}}{\partial\overline{\theta}}\frac{\overline{F}_1}{\overline{F}_0}\right)\int_0^{\overline{z}}\frac{d\overline{z}}{\overline{\mu}} + 1 \tag{2.2}$$

$$\overline{v}_r = \overline{h}^2\frac{\partial\overline{p}}{\partial\overline{r}}\int_0^{\overline{z}}\frac{\overline{z}d\overline{z}}{\overline{\mu}} - \overline{h}^2\frac{\partial\overline{p}}{\partial\overline{r}}\frac{\overline{F}_1}{\overline{F}_0}\int_0^{\overline{z}}\frac{d\overline{z}}{\overline{\mu}} \tag{2.3}$$

$$\overline{v}_z = -\frac{1}{\overline{r}}\frac{\partial}{\partial\overline{r}}\int_0^{\overline{z}}\overline{r}\overline{h}\overline{v}_r d\overline{z} - \frac{1}{\theta_0}\frac{\partial}{\partial\overline{\theta}}\int_0^{\overline{z}}\overline{h}\overline{v}_\theta d\overline{z} + \overline{z}\frac{\partial\overline{h}}{\partial\overline{r}}\overline{v}_r + \frac{\overline{z}}{\theta_0}\frac{\partial\overline{h}}{\partial\overline{\theta}}\overline{v}_\theta \tag{2.4}$$

$$\overline{F}_0 = \int_0^1\frac{d\overline{z}}{\overline{\mu}} + \frac{\overline{h}_p}{\overline{\mu}_p\overline{h}}\ ,\ \overline{F}_1 = \int_0^1\frac{\overline{z}d\overline{z}}{\overline{\mu}} + \frac{1}{\overline{\mu}_p}\left(\frac{\overline{h}_p}{\overline{h}} + \frac{\overline{h}_p^2}{2\overline{h}^2}\right) \tag{2.5}$$

Introducing the $\overline{r}-$ and $\overline{\theta}-$velocity components in the continuity equation and integrating across the oil film following the approach suggested by Dowson (1962) the Reynolds equation for 2-dimensional pressure in the oil film becomes:

$$\frac{1}{\overline{r}}\frac{\partial}{\partial\overline{r}}\left[\overline{G}_1\overline{r}\overline{h}^3\frac{\partial\overline{p}}{\partial\overline{r}}\right] + \frac{1}{\theta_0^2\overline{r}^2}\frac{\partial}{\partial\overline{\theta}}\left[\overline{G}_1\overline{h}^3\frac{\partial\overline{p}}{\partial\overline{\theta}}\right] = \frac{1}{\theta_0}\frac{\partial}{\partial\overline{\theta}}\left[\overline{h}\left(\frac{\overline{G}_0}{\overline{F}_0} - 1\right)\right] - \overline{v}_{z,inj} \tag{2.6}$$

$$\overline{G}_0 = \int_0^1\int_0^{\overline{z}}\frac{d\overline{z}}{\overline{\mu}}d\overline{z} + \frac{\overline{h}_p}{\overline{h}}\int_0^1\frac{d\overline{z}}{\overline{\mu}} + \frac{\overline{h}_p^2}{2\overline{h}^2\overline{\mu}_p} \tag{2.7}$$

$$\overline{G}_1 = \int_0^1\int_0^{\overline{z}}\frac{\overline{z}d\overline{z}}{\overline{\mu}}d\overline{z} + \frac{\overline{h}_p}{\overline{h}}\int_0^1\frac{\overline{z}d\overline{z}}{\overline{\mu}} + \frac{1}{6\overline{\mu}_p}\left(\frac{\overline{h}_p^3}{\overline{h}^3} + 3\frac{\overline{h}_p^2}{\overline{h}^2}\right) - \frac{\overline{F}_1}{\overline{F}_0}\overline{G}_0 \tag{2.8}$$

$\overline{v}_{z,inj}$ is the nondimensionalised injection velocity at $\overline{z} = 1 + \overline{h}_p$. At all edges, the pressure is set to zero. Subject to a known viscosity distribution, equation (2.6) can be solved to give the pressure distribution in the oil film.

The assumption of zero pressure at the leading edge is not strictly valid. The oil entering the pad is stagnated at the entrance to the pad resulting in a positive pressure at the leading edge. (Heckelman & Ettles, 1987; Rhim & Tichy, 1989; Kim & Kim, 2002) have theoretically and experimentally

treated this phenomenon and have derived empirical expressions for the pressure. The pressures predicted by the different expressions vary significantly and a comparison to the experimental results stated in chapter 4 have shown that none of the expressions approximate the inlet pressure condition well at a large interval of velocities. In large slow speed bearings the leading edge pressure is usually insignificant and the approximation of zero pressure is adequate. The implications of neglecting inertia in a deep recess are discussed in chapter 7.

Keeping the diffusive term in the $\overline{z}-$direction only and reducing the dissipative terms following Dowson (1962) the conservative energy equation for the oil film reduces to:

$$\frac{1}{\overline{r}}\frac{\partial \overline{v}_r \overline{r}\overline{T}}{\partial \overline{r}} + \frac{1}{\theta_0}\frac{\partial \overline{v}_\theta \overline{T}}{\partial \overline{\theta}} - \frac{\overline{z}}{\overline{h}}\frac{\partial \overline{h}}{\partial \overline{r}}\frac{\partial \overline{v}_r \overline{T}}{\partial \overline{z}} - \frac{\overline{z}}{\theta_0 \overline{h}}\frac{\partial \overline{h}}{\partial \overline{\theta}}\frac{\partial \overline{v}_\theta \overline{T}}{\partial \overline{z}} + \frac{1}{\overline{h}}\frac{\partial \overline{v}_z \overline{T}}{\partial \overline{z}} = \frac{k}{\rho c \omega h_0^2}\frac{1}{\overline{h}^2}\frac{\partial^2 \overline{T}}{\partial \overline{z}^2} + \frac{\mu_0 r_1^2 \omega}{\rho c T_0 h_0^2}\left[\frac{\overline{\mu}}{\overline{h}^2}\left(\frac{\partial \overline{v}_r}{\partial \overline{z}}\right)^2 + \frac{\overline{\mu r}^2}{\overline{h}^2}\left(\frac{\partial \overline{v}_\theta}{\partial \overline{z}}\right)^2\right] \tag{2.9}$$

The temperature in the recess is calculated from a control volume formulation using the approximations that there is zero thermal diffusion on the oil film/recess boundary and that the temperature on the solid wall is equal to the recess temperature.

$$0 = \sum \dot{m}_i u_i - \sum \dot{m}_e u_e + \dot{Q}_{gen,p} + \dot{Q}_{cond,p} \tag{2.10}$$

$\dot{Q}_{gen,p}$ designates the heat generated in the recess, and $\dot{Q}_{cond,p}$ designates the heat conducted from the pad. u_i and u_e designate the internal energy ($du = c \cdot dT$) in the inlet and exit flows into and out of the recess. Using that the mass flows out of and into the recess are equal ($\sum \dot{m}_e = \sum \dot{m}_i$) due to continuity and expanding the terms in equation (2.10), it can be rewritten to give the recess temperature:

$$\overline{T}_p = \left[\overline{\dot{V}}_{inj} + \int_{\overline{A}_i}\left(\overline{v}_r\frac{\partial \overline{h}}{\partial \overline{r}} + \frac{\overline{v}_\theta}{\overline{r}}\frac{\partial \overline{h}}{\partial \overline{\theta}} + \overline{v}_z\right)d\overline{A}\right]^{-1} \cdot \left[\overline{\dot{V}}_{inj}\overline{T}_{inj} + \int_{\overline{A}_i}\left(\overline{v}_r\frac{\partial \overline{h}}{\partial \overline{r}} + \frac{\overline{v}_\theta}{\overline{r}}\frac{\partial \overline{h}}{\partial \overline{\theta}} + \overline{v}_z\right)\overline{T}_i d\overline{A} + \frac{\mu_0 r_1^2 \omega}{\rho c T_{in} h_0^2}\int_{\overline{A}_p}\overline{\mu}_p\overline{h}\left\{\int_1^{1+\overline{h}_p}\frac{1}{\overline{h}^2}\left(\frac{\partial \overline{v}_r}{\partial \overline{z}}\right)^2 d\overline{z} + \int_1^{1+\overline{h}_p}\frac{\overline{r}^2}{\overline{h}^2}\left(\frac{\partial \overline{v}_\theta}{\partial \overline{z}}\right)^2 d\overline{z}\right\}d\overline{A}_p - \frac{k_{pad}}{t_{pad}\rho h_0 \omega c}\int_{\overline{A}_p}\frac{\partial \overline{T}}{\partial \overline{z}_{pad}}\bigg|_{\overline{z}_{pad}=0} d\overline{A}\right] \tag{2.11}$$

$$\int_1^{1+\overline{h}_p}\frac{1}{\overline{h}^2}\left(\frac{\partial \overline{v}_r}{\partial \overline{z}}\right)^2 d\overline{z} = \left(\frac{\partial \overline{p}}{\partial \overline{r}}\right)^2\frac{1}{\overline{\mu}_p^2}\left[\frac{1}{3}\frac{\overline{h}_p^3}{\overline{h}} + \overline{h}\overline{h}_p + \overline{h}_p^2\overline{h}\overline{h}_p\left(\frac{\overline{F}_1}{\overline{F}_0}\right)^2 + (\overline{h}_p^2 + 2\overline{h}\overline{h}_p)\frac{\overline{F}_1}{\overline{F}_0}\right] \tag{2.12}$$

$$\int_1^{1+\overline{h}_p}\frac{\overline{r}^2}{\overline{h}^2}\left(\frac{\partial \overline{v}_\theta}{\partial \overline{z}}\right)^2 d\overline{z} = \frac{1}{\theta_0}\left(\frac{\partial \overline{p}}{\partial \overline{\theta}}\right)^2\frac{1}{\overline{\mu}_p^2\overline{r}^2}\left[\frac{1}{3}\frac{\overline{h}_p^3}{\overline{h}} + \overline{h}\overline{h}_p + \overline{h}_p^2 + \overline{h}\overline{h}_p\left(\frac{\overline{F}_1}{\overline{F}_0}\right)^2 + (\overline{h}_p^2 + 2\overline{h}\overline{h}_p)\frac{\overline{F}_1}{\overline{F}_0}\right] + \frac{1}{\theta_0}\frac{\partial \overline{p}}{\partial \overline{\theta}}\frac{1}{\overline{\mu}_p^2}\left[\frac{2\overline{F}_1\overline{h}_p}{\overline{F}_0^2\overline{h}} - \frac{1}{\overline{F}_0}\left(\frac{\overline{h}_p^2}{\overline{h}^2} + 2\frac{\overline{h}_p}{\overline{h}}\right)\right] \tag{2.13}$$

A_p is the area of the recess and A_i is the area in which there is inflow to the recess from the oil film. T_i is the oil film temperature at $\overline{z} = 1$ which is determined by solution of equation (2.9). Equation

(2.12) and equation (2.13) are expansions of the terms in equation (2.11) for the generated heat in the recess.

In equation (2.9) upwinding is used for the discretization of the convective terms. No boundary conditions are therefore needed at $\overline{\theta} = 1$, $\overline{r} = 1$ and $\overline{r} = \overline{r}_2$ where the flow direction is out of the computational domain. At $\overline{\theta} = 0$, $\overline{T} = \overline{T}_{le}$. The leading edge temperature $\overline{T}_{le}$ is determined in section 2.2.2 of the report. At $\overline{z} = 0$, $\overline{T} = \overline{T}_c$ which is considered constant in both $\overline{r}$ and $\overline{\theta}$. $\overline{T}_c$ must be stated as an input to the model. In the $\overline{z}$-direction, diffusion is neglected at the boundary to the recess volume. No boundary condition is therefore needed inside the recess area at $\overline{z} = 1$ when $\overline{v}_z > 0$. $\overline{T}_p$ provides the boundary condition when $\overline{v}_z < 0$. The pad temperature gives the boundary condition outside the recess area. The collar temperature depends on the thermal boundary conditions on the backside of the collar. These can vary depending on how the bearing is built in. To keep the model general and simple it is therefore chosen to state the collar temperature as an input.

2.2.2 Heat transfer

Equation (2.14) describes heat transfer in the pad. On the oil/pad-surface, equation (2.15) states the boundary condition on temperature. At the free sides of the pad, the boundary conditions are given in the form of convection coefficients, H (equation 2.16), where T_a is the oil bath temperature and n represents the normal to the surface. At the inner and outer radial surfaces, a laminar boundary layer solution is used assuming the free stream velocity to be equal to the collar velocity (equation 2.17). Ettles & Anderson (1991) state the correlation given in equation (2.18) for the convection coefficient at the back of the pad. They also state that experiments indicate the values of H at the leading and trailing surfaces to be twice as high as the value at the back of the pad. These values are used due to the absence of more detailed experimental results.

$$0 = \frac{1}{\overline{r}}\frac{\partial}{\partial \overline{r}}\left(\overline{r}\frac{\partial \overline{T}}{\partial \overline{r}}\right) + \frac{1}{\theta_0^2 \overline{r}^2}\frac{\partial^2 \overline{T}}{\partial \overline{\theta}^2} + \frac{r_1^2}{t_{pad}^2}\frac{\partial^2 \overline{T}}{\partial \overline{z}_{pad}^2} \tag{2.14}$$

$$\frac{\partial \overline{T}}{\partial \overline{z}_{pad}}\Big|_{\overline{z}_{pad}=0} = \frac{k t_{pad}}{k_{pad} h_0 \overline{h}}\frac{\partial \overline{T}}{\partial \overline{z}}\Big|_{\overline{z}=1} \tag{2.15}$$

$$H(\overline{T} - \overline{T}_a) = -k_{pad}\frac{\partial \overline{T}}{\partial n} \tag{2.16}$$

$$H_r = \frac{0.332k}{r_1 \overline{r} \theta_0 \overline{\theta}} Re^{\frac{1}{2}} Pr^{\frac{1}{3}}\ ,\ Re = \frac{\rho r_1^2 \omega \theta_{pad} \overline{\theta} \overline{r}^2}{\mu}\ ,\ Pr = \frac{c\mu}{k} \tag{2.17}$$

$$H_{back} = 25.5(r_1 \overline{r} \omega)^{0.7} (\mu_0 \overline{\mu})^{-0.2} L_{pad}^{-0.4},\ L_{pad} = \frac{r_1(1 + \overline{r}_2)\theta_{pad}}{2} \tag{2.18}$$

Following the general procedure of Vohr (1981) $\overline{T}_a$ and $\overline{T}_{le}$ can be determined to fulfil equilibrium of thermal energy for the entire bearing and for the groove between pads. Assuming that all the generated heat flows into the oil bath and is mixed with the cold oil, the oil bath temperature T_a is determined from the heat generated in the oil due to viscous shear $\dot{Q}_{gen}$. The generated heat is calculated as the work used to turn the collar plus the work used to inject the oil in the recess. The oil injection work is calculated neglecting changes in kinetic energy and the influence of restrictors

in the flow. $\dot{W}_{inj}$ can therefore be determined directly from the pressure change in the injection flow.

$$\overline{T}_a = 1 + \frac{r_1^3\theta_0\omega^2\mu_0}{c\rho\dot{V}_{oil}T_0}\overline{\dot{Q}}_{gen}\,, \qquad \overline{\dot{Q}}_{gen} = \overline{\dot{W}}_{fric} + \overline{\dot{W}}_{inj} \tag{2.19}$$

$$\overline{\dot{W}}_{fric} = \frac{r_1}{h_0}\int_1^{\bar{r}_2}\int_0^1 \frac{\overline{r}^3\overline{\mu}}{\overline{h}}\frac{\partial\overline{v}_\theta}{\partial\overline{z}}\Big|_{\overline{z}=0} d\overline{\theta}d\overline{r}\,, \qquad \overline{\dot{W}}_{inj} = \frac{r_1}{h_0}\overline{\dot{V}}_{inj}\overline{p}_{inj} \tag{2.20}$$

p_{inj} is the pressure in the oil film at the oil injection pipe determined from the Reynolds equation.

The heat balance in the groove is not readily determined. Heat is convected to the collar at the trailing edge of the pad where the exit oil is hot. At the leading edge of the pad, however the collar may conduct heat to the oil. Heat is convected from the hot exit oil to the colder oil bath. All these phenomena are difficult to quantify and few experimental results are available in the literature. Vohr (1981) states an average experimental value of the groove convection coefficient $H_{gr,Vohr} = 2960$ W/m^2/K for a bearing of $r_1 = 0.43$ m, $r_2 = 0.585$ m and $\theta_{gr,Vohr} = 0.105$ rad operating at $\omega_{Vohr} = 15.71\,rad/s$. Vohr's result is extrapolated using laminar flow theory stating the convection coefficient to be proportional to the square root of velocity divided by the distance between pads. The groove heat transfer $\dot{Q}_{gr}$ can then be determined through equation (2.21). Equation (2.23) states energy conservation on a control volume. With the additional assumption that no thermal energy is transported in the radial direction in the groove, T_{le} can be found through equations (2.24), (2.25) and (2.26). Equation (2.26) defines the distribution of leading edge temperature in the $\bar{z}$-direction. The equation is chosen for reasons of numerical stability and accuracy and has no physical basis. It ensures continuity of temperature at the collar surface. Continuity of temperature at the collar surface is important for the global conservation of energy. When a leading edge taper is present in the analysed bearing, a uniform temperature distribution is used. In this case, there is back flow at the leading edge and most of the inflow to the bearing occurs close to the collar.

$$\overline{\dot{Q}}_{gr} = \frac{T_0}{r_1\omega^2\mu_0}\int_1^{\overline{r}_2} H_{gr}(\overline{T}_c - \overline{T}_a)\overline{r}\overline{\theta}_{gr}d\overline{r} \tag{2.21}$$

$$H_{gr} = H_{gr,Vohr}\sqrt{\frac{\theta_{gr,Vohr}\cdot\omega}{\theta_{gr}\cdot\omega_{Vohr}}} \tag{2.22}$$

$$\overline{\dot{Q}}_{oil,le} = \overline{\dot{Q}}_{oil,te} - \overline{\dot{Q}}_{gr} \tag{2.23}$$

$$\overline{\dot{Q}}_{oil,le} = \frac{T_0 c\rho}{\omega\mu_0}\int_0^1\int_1^{\overline{r}_2}(\overline{T} - \overline{T}_a)\overline{v}_\theta\overline{h}d\overline{r}d\overline{z}\ , \quad \text{at } \overline{\theta} = 0 \tag{2.24}$$

$$\overline{\dot{Q}}_{oil,te} = \frac{T_0 c\rho}{\omega\mu_0}\int_0^1\int_1^{\overline{r}_2}(\overline{T} - \overline{T}_a)\overline{v}_\theta\overline{h}d\overline{r}d\overline{z}\ , \quad \text{at } \overline{\theta} = 1 \tag{2.25}$$

$$\overline{T}_{le} = \overline{T}_c + (\overline{T}_c - \overline{T}_{le,pad})(\overline{z}^2 - 2\overline{z}) \tag{2.26}$$

The treatment of heat transfer coefficients is coarse and does not take differences in support design into account. equation (2.14) is stated for a pad of uniform thickness although a multilayered design is often used in large bearings to reduce thermal deflections. As described in section 2.2.3

the numerical model allows for the analysis of thermal bending of pads of variable thicknesses. The restriction given by the description of heat transfer is that such a pad of variable thickness is composed of a main pad of uniform thickness and a supporting structure. The main pad is treated in three dimensions while heat transfer through supporting structures is considered one dimensional in the z_{pad}-direction only. Generally, only a small amount ($5 - 25$ %) of the generated heat is transported through the pad. Inexact treatment of heat transfer phenomena therefore only induces small errors on the pad and oil temperatures.

2.2.3 Deflection of bearing pad

The deflection of the pad is modelled following Gould (1988) using a flat plate approximation for a plate of variable thickness. A plate of variable thickness is modelled in order to accommodate supporting structures, which are tightly fixed to the main pad. An example of the implementation of the equation system on a pad with a firmly fixed circular support is given in chapter 3.2.

The equation system has not been nondimensionalised as it does not simplify the description. Force equilibrium in the z_{pad}-direction yields:

$$0 = \frac{\partial}{\partial r}\left[\frac{\partial(rM_r)}{\partial r} + \frac{\partial M_{r\theta}}{\partial \theta} - M_\theta\right] + \frac{1}{r^2}\frac{\partial}{\partial \theta}\left[\frac{\partial(rM_{r\theta})}{\partial r} + \frac{\partial M_\theta}{\partial \theta} + M_{r\theta}\right] + p \tag{2.27}$$

Introducing M_r, M_θ and $M_{r\theta}$ as given by equation (2.29)−(2.33), equation (2.27) transforms into a fourth order differential equation in pad deflection w. A pad with a point pivot is restricted by $w = \partial w/\partial r = \partial w/\partial \theta = 0$ at the pivot point. The boundary conditions at the free edges of the plate are stated in equation (2.28). The Kirchhoff shear stresses and bending moments are zero, and at the four corners the twisting moments are zero. t_{plate} denotes the thickness of the plate.

$$\left.\begin{array}{llll} 0 = V_\theta(r,0), & 0 = M_\theta(r,0), & 0 = V_\theta(r,\theta_{pad}), & 0 = M_\theta(r,\theta_{pad}), \\ 0 = V_r(r_1,\theta), & 0 = M_r(r_1,\theta), & 0 = V_r(r_2,\theta), & 0 = M_r(r_2,\theta), \\ 0 = M_{r\theta}(r_1,0), & 0 = M_{r\theta}(r_1,\theta_{pad}), & 0 = M_{r\theta}(r_2,0), & 0 = M_{r\theta}(r_2,\theta_{pad}) \end{array}\right\} \tag{2.28}$$

$$M_r = -D\left[\frac{\partial^2 w}{\partial r^2} + \nu\left(\frac{1}{r}\frac{\partial w}{\partial r} + \frac{1}{r^2}\frac{\partial^2 w}{\partial \theta^2}\right)\right] - M_T \tag{2.29}$$

$$M_\theta = -D\left[\frac{1}{r}\frac{\partial w}{\partial r} + \frac{1}{r^2}\frac{\partial^2 w}{\partial \theta^2} + \nu\frac{\partial^2 w}{\partial r^2}\right] - M_T \tag{2.30}$$

$$M_{r\theta} = -D(1-\nu)\frac{\partial}{\partial r}\left(\frac{1}{r}\frac{\partial w}{\partial \theta}\right) \tag{2.31}$$

$$M_T = \frac{E}{1-\nu}\int_0^{t_{plate}} (z_{pad} - \frac{t_{plate}}{2})\alpha T dz_{pad} \tag{2.32}$$

$$D = \frac{E t_{plate}^3}{12(1-\nu^2)} \tag{2.33}$$

$$V_r = -D\left[\frac{\partial}{\partial r}(\nabla^2 w) + (1-\nu)\frac{1}{r}\frac{\partial}{\partial r}\left(\frac{1}{r}\frac{\partial^2 w}{\partial \theta^2}\right)\right] - \frac{\partial M_T}{\partial r} \tag{2.34}$$

$$V_\theta = -D\left[\frac{1}{r}\frac{\partial}{\partial\theta}(\nabla^2 w) + (1-\nu)\frac{\partial^2}{\partial r^2}\left(\frac{1}{r}\frac{\partial w}{\partial\theta}\right)\right] - \frac{1}{r}\frac{\partial M_T}{\partial\theta} \tag{2.35}$$

For a pad of constant thickness equation (2.27) reduces to the well known plate equation:

$$\nabla^2(\nabla^2 w) = \frac{p}{D} - \frac{1}{D}\nabla^2 M_T \tag{2.36}$$

2.2.4 Bearing equilibrium

The film thickness is calculated as a geometrical relation between the roll and pitch angles and the film thickness at the pivot point. Linearizing to only contain first order terms yields equation (2.37). The pressure distribution is integrated over the pad area to give the resulting force (equation 2.38) and the moments in two perpendicular directions around the pivot point (equation 2.39 and 2.40).

$$\overline{h} = 1 - \overline{\alpha}_r[\overline{r}_{piv} - \overline{r}\cos(\theta_{pad}(\overline{\theta} - \overline{\theta}_{piv}))] - \overline{\alpha}_p\overline{r}\sin(\theta_{pad}(\overline{\theta} - \overline{\theta}_{piv})) + \overline{w} \tag{2.37}$$

$$0 = \overline{F}_{res} = \int_1^{\overline{r}_2}\int_0^1 \overline{pr}\,d\overline{\theta}\,d\overline{r} - \overline{F}_z \tag{2.38}$$

$$0 = \overline{M}_x = \int_1^{\overline{r}_2}\int_0^1 \overline{pr}^2\sin(\theta_{pad}(\overline{\theta} - \overline{\theta}_{piv}))\,d\overline{\theta}\,d\overline{r} \tag{2.39}$$

$$0 = \overline{M}_y = \int_1^{\overline{r}_2}\int_0^1 \overline{pr}[\overline{r}\cos(\theta_{pad}(\overline{\theta} - \overline{\theta}_{piv})) - \overline{r}_{piv}]\,d\overline{\theta}\,d\overline{r} \tag{2.40}$$

Solving these equations for a given pressure distribution, pad deflection and load yields the distribution of oil film thickness.

2.2.5 Miscellaneous relations

Viscosity is calculated as a function of temperature using an expression by Roelands (Hamrock et al., 2004).

$$\mu = 10^{[k_1\cdot(1+\frac{T-273.15}{135})^{k_2}-4.200]} \tag{2.41}$$

in which the constants k_1 and k_2 are determined from the measured viscosity of the oil.

2.3 Governing Equations (2-dimensional formulation)

The equation set stated in chapter 2.2 is reduced to a 2-dimensional form. As shown in figure 2.3 the nondimensional oil film thickness $\overline{h}$ in these equations includes the recess depth. The energy equation for the fluid film is integrated over the oil film thickness to give a bulk flow formulation. Heat transfer in the pad is considered a 1-dimensional problem in which heat transfer to the surroundings is assumed to take place at the back of the pad only. This simplifies the determination of the thermal moment causing the bending of the pad.

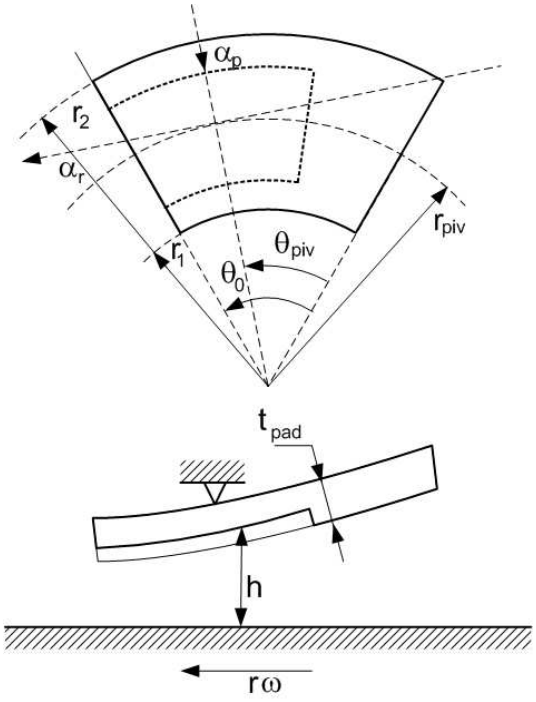

Figure 2.3: The coordinate system used for the 2-dimensional calculations.

2.3.1 Fluid film

Assuming viscosity to be a function of $\overline{r}$ and $\overline{\theta}$ only, the Reynolds equation reduces to the following:

$$\frac{1}{12\overline{r}}\frac{\partial}{\partial\overline{r}}\left[\frac{\overline{r}\overline{h}^3}{\overline{\mu}}\frac{\partial\overline{p}}{\partial\overline{r}}\right]+\frac{1}{12\theta_{pad}^2\overline{r}^2}\frac{\partial}{\partial\overline{\theta}}\left[\frac{\overline{h}^3}{\overline{\mu}}\frac{\partial\overline{p}}{\partial\overline{\theta}}\right]=\frac{1}{2\theta_{pad}}\frac{\partial\overline{h}}{\partial\overline{\theta}}+\overline{v}_{z,inj} \tag{2.42}$$

The energy equation integrated over the oil film thickness $\overline{h}$:

$$\begin{aligned}\frac{1}{12\overline{r}}\frac{\partial}{\partial\overline{r}}\left[\frac{\overline{h}^3\overline{r}\overline{T}}{\overline{\mu}}\frac{\partial\overline{p}}{\partial\overline{r}}\right]+\frac{1}{12\theta_{pad}^2\overline{r}^2}\frac{\partial}{\partial\overline{\theta}}\left[\frac{\overline{h}^3\overline{T}}{\overline{\mu}}\frac{\partial\overline{p}}{\partial\overline{\theta}}\right]-\frac{1}{2\theta_{pad}}\frac{\partial}{\partial\overline{\theta}}\left[\overline{hT}\right]=\\ -\frac{r_1^2\omega\mu_0}{\rho cT_{in}h_0^2}\left[\frac{\overline{h}^3}{12\overline{\mu}}\left(\frac{\partial\overline{p}}{\partial\overline{r}}\right)^2+\frac{\overline{h}^3}{12\theta_{pad}^2\overline{\mu}\overline{r}^2}\left(\frac{\partial\overline{p}}{\partial\overline{\theta}}\right)^2+\frac{\overline{r}^2\overline{\mu}}{\overline{h}}\right]-\frac{S_T}{\rho c\omega T_{in}h_0}\end{aligned} \tag{2.43}$$

where S_T contains the energy added through heat transfer at $\overline{z}=0$ and at $\overline{z}=1$. S_T is determined in section 2.3.2. The boundary conditions on the equations (2.42) and (2.43) are as stated in section 2.2.1.

2.3.2 Heat transfer

Heat transfer through the pad is treated in a simplified way by only modelling heat transfer at the back of the pad and treating conduction in the pad as a 1-dimensional problem. This formulation

is used in combination with the 2-dimensional integrated energy equation for the oil film. The oil temperature in this formulation is considered uniform in the $\overline{z}$-direction and the Nusselt number, $Nu = 7.55$ (Kays & Crawford, 1993) for a fully developed velocity profile between parallel plates is used to calculate the convection heat transfer coefficients at pad and collar. The S_T-term in equation (2.43) thereby becomes:

$$S_T = \left[\frac{4h}{kNu} + \frac{t_{pad}}{k_{pad}} + \frac{1}{H_{back}}\right]^{-1}(T - T_a) - \frac{kNu}{4h}(T - T_c) \tag{2.44}$$

Equation (2.20) for the bearing friction loss reduces to:

$$\overline{\dot{W}}_{fric} = \frac{r_1}{h_0}\int_1^{\bar{r}_2}\int_0^1 \frac{\overline{r}^3\overline{\mu}}{\overline{h}}\Big(\frac{1}{2\theta_0}\frac{\overline{h}^2}{\overline{r}^2\overline{\mu}}\frac{\partial\overline{p}_\theta}{\partial\overline{\theta}} + 1\Big)d\overline{\theta}d\overline{r}\,, \qquad \overline{\dot{W}}_{inj} = \frac{r_1}{h_0}\overline{\dot{V}}_{inj}\overline{p}_{inj} \tag{2.45}$$

2.3.3 Deflection of bearing pad

Subject to a linear temperature distribution through the pad equation (2.32) reduces to the following expression:

$$M_T = \frac{t_{plate}^2 E\alpha}{12(1-\nu)}(T_{bab} - T_{back}) \tag{2.46}$$

in which T_{bab} designates the temperature on the oil film / pad interface and T_{back} designates the temperature on the oil bath side of a pad.

2.4 Numerical Description and Solution Method

The equation system is solved on a finite volume grid which may be uniform in all the transformed variables. Alternatively it may be designed to follow the edges of a recess in the bearing pad surface and with increased control volume density close to the the recess edges. The 2-dimensional thermal deflection of the bearing pad is always solved on a uniform grid. Variables are interpolated between the grids. Second order discretizations are used for the derivatives except for the convective terms in equation (2.9) which are discretized using upwinding. A detailed description of the resulting equation system is not given here as standard finite volume formulations are used. 2-dimensional grids are used for pressure and pad deflection equations. 3-dimensional grids for the temperature equations. Details of the computational grid are graphically shown in figure 2.4. To accommodate abrupt changes in oil film thickness, $\overline{h}$ is calculated on the cell faces as well as in the cell centres. Integrals are evaluated using the composite trapezoidal rule. For hydrostatic jacking oil is usually injected at the centre of the injection pocket. In the numerical formulation the volume flow of injection oil is specified as a boundary condition. In the numerical implementation of equation (2.6) oil is injected only in the control volume which is closest to the injection pipe. Thus $\overline{v}_{z,inj} = \overline{\dot{V}}_{inj}/(\overline{r}d\overline{r}d\overline{\theta})$.

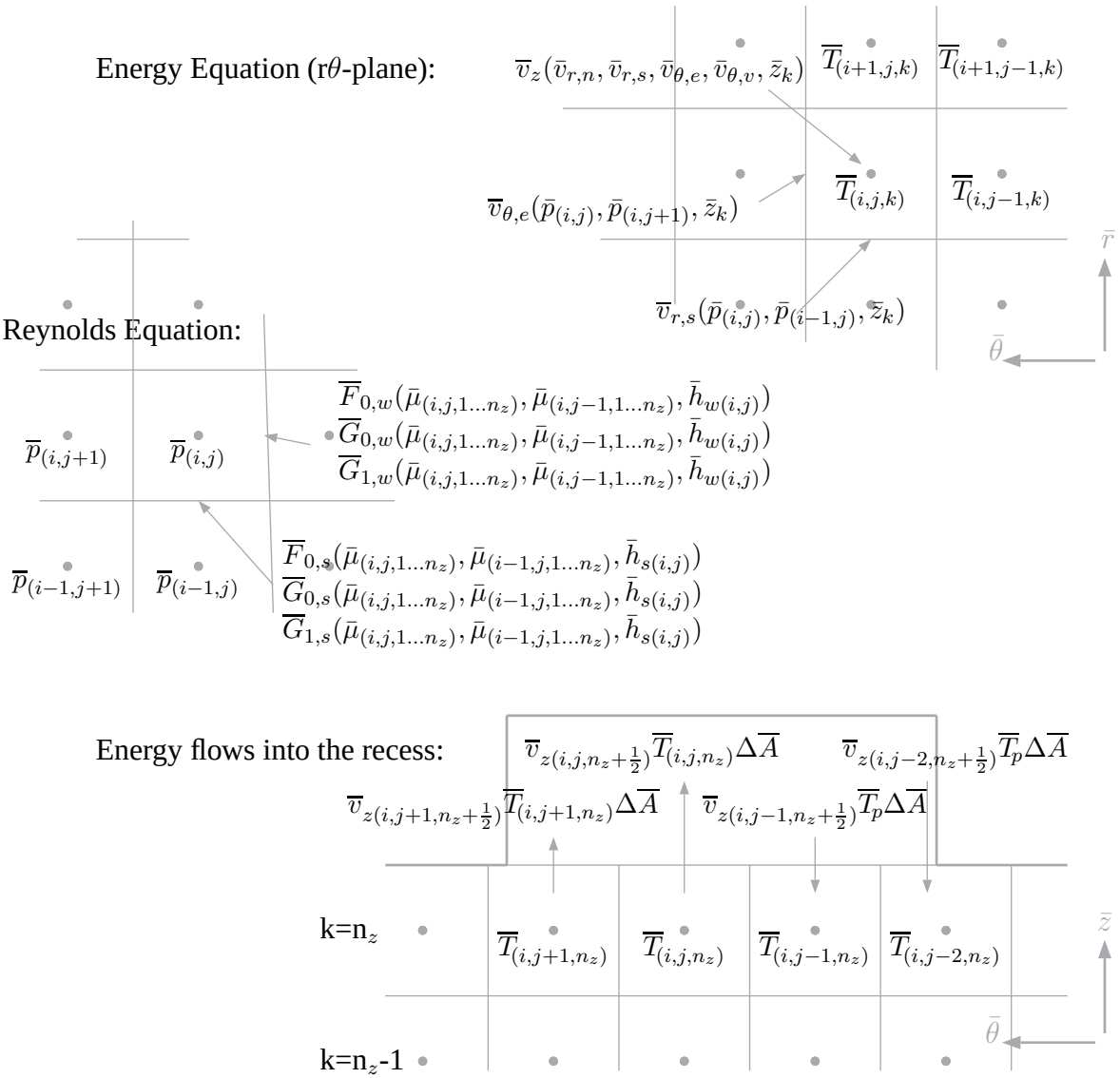

Figure 2.4: Selected details of the computational grid. Top: The energy equation: $r-$ and $\theta-$velocities are evaluated at the cell faces. $z-$velocities are calculated at the cell centres and interpolated to the lower and upper faces. Middle: The Reynolds equation: $\overline{F}_0$, $\overline{G}_0$ and $\overline{G}_1$ are evaluated at the cell faces. Bottom: The energy fluxes from the oil film into the recess control volume.

The problem is solved using an iterative procedure as depicted in the flowchart in figure 2.5. The Newton-Raphson method is used for adjusting $\overline{\alpha}_p$, $\overline{\alpha}_r$ and h_0 until the residuals of the equations (2.38), (2.39) and (2.40) are below some threshold.

The Reynolds equation may predict negative pressures in some control volumes, for instance as a result of a diverging oil film at the trailing edge corners due to thermal crowning. In such cases cavitation is to be expected. Numerically the problem is treated by setting negative pressures equal to zero. This is a simple approximation, which does not satisfy the equation of continuity. However,

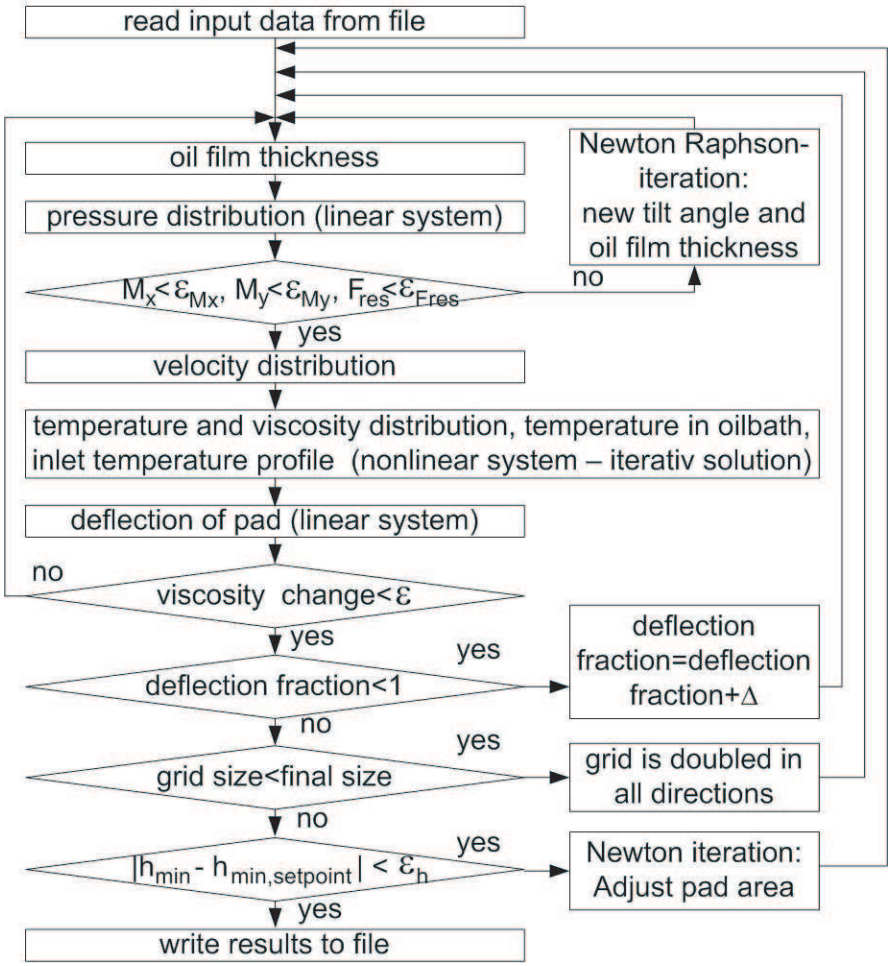

Figure 2.5: Flow chart for the programme.

cavitation does not usually occur in tilting-pad thrust bearings with pivots offset from the centres of the pads, and when it appears in the calculations it is in the study of bearings operating at unusual operating conditions.

The discretized Reynolds equation and plate equation constitute linear systems of equations and are solved using direct methods. The discretized energy equations for oil and pad and their boundary conditions constitute a nonlinear system of equations. Oil film temperature, viscosity and oil bath temperature are calculated simultaneously using a point iterative Gauss-Seidel SOR solver.

The first sweep of the equations causes the temperature distribution to be overestimated. This causes the pad deflection to be overestimated. As a result the oil film thickness distribution and viscosity distribution in the next sweep may cause the energy equation to diverge. To overcome this problem only a fraction of the calculated deflection is applied to the oil film distribution. A loop increases the fraction to one. The grid size can be successively doubled to save computation time. The programme includes an option to adjust the pad surface area by the use of a Newton iteration so that the minimum oil film thickness has a prescribed value. A restriction on the minimum oil

film thickness is often used as a design criteria. Similarly, the radial position of the pivot point can be adjusted by the use of a Newton iteration so that the minimum oil film thickness is located at the centre of the trailing edge. Calculations have shown that designing for this criteria gives close to the optimal performance when prescribing a minimum oil film thickness.

2.5 Conclusion

In this chapter two numerical models for tilting-pad thrust bearings have been derived. Both models are based on the Reynolds equation for pressure and involve the calculation of temperature in oil and pad and the influence of the bending of the pad due to pressure and thermally induced moments. The oil bath and leading edge temperatures are calculated through control volume expressions for conservation of energy. The collar temperature must be stated as an input parameter. This restriction on the model is imposed to avoid modelling heat transfer phenomena through the collar, rotor and adjoining components.

A model involving a 3-dimensional description of the temperature field is elaborated. The model allows for the inclusion of deep recesses with recirculation flows in the pad surfaces and for high pressure oil injection through the surfaces of the bearing pads. The assumptions of the Reynolds equation are not valid for the flow in a deep recess, which is one or more orders of magnitude deeper than the surrounding oil film. In addition, depending on the operating conditions, the recess flow may be turbulent. However, the pressure variations inside the recess are small and assuming inertial effects to be negligible the errors induced on the calculated pressure distribution are small. The description of the thermal conditions inside the recess is simplified by treating the volume of the recess as one control volume of constant temperature. The generated heat inside the volume of the recess is much smaller than in the thinner oil film and the recirculation flow results in a large amount of mixing justifying this description.

The 3-dimensional formulation does not provide a good description of bearings in which there are shallow recesses in the bearing pads. In such recesses there is no recirculation and the assumption of a uniform mixed temperature is not valid. Allowing the 3-dimensional grid to stretch into the recess is not feasible due to the discontinuity of the oil film at the recess edges. For such problems a 2-dimensional formulation is elaborated in which the energy equation is integrated over the thickness of the oil film. The 2-dimensional treatment of the temperature field does not deal well with regions of back flow and the study of recesses are therefore limited to those sufficiently shallow not to generate recirculation. The principal disadvantage of a 2-dimensional over a 3-dimensional formulation of the flow in standard bearing pads without recesses, is in the less exact calculation of the temperature gradients at the pad and collar surfaces. The calculation of the heat transfers through the solid components is therefore less accurate and more importantly, especially in large bearings, the calculation of the thermal crowning of the pads is less accurate due to the lack of knowledge of the temperatures on the pad / oil interface.

In chapter 3 and chapter 4 the models are validated using measurements.

Chapter 3

Validation of Models

To validate the numerical models theoretical results are compared to different sets of experimental data. Glavatskikh (2000, 2001) has published experimental data for a 228 mm outer diameter six-pad bearing. The data include extensive measurements of temperatures below the babbitt surface and oil film thickness measurements at the leading and trailing edges of the pad. Glavatskikhs measurements are used to validate the models for a bearing without recesses in the bearing surface. Calculations using isothermal, 2-dimensional and 3-dimensional adiabatic models and models in which heat transfer and pad bending is included are performed. The variations in the results between the different models are discussed.

Furthermore, a comparison between theoretical results and measurements conducted on a 2.2 m outer diameter bearing in operation in the Bieudron hydro power plant in Switzerland is performed. The bearing has oil injection pockets at the pivot points covering 3.6 % of the total bearing area*.

In chapter 4 experiments are presented to further validate the models. Comparisons between theoretical and experimental pressure profiles are performed with and without oil injection pockets in the bearing surface and with and without constant volume flow high-pressure oil injection. Furthermore, a validation of the theoretically predicted pressure bending and thermal crowning of the bearing pads is performed.

3.1 Comparison with Published Experimental Data

Simulation results are compared to experimental data presented by (Glavatskikh, 2000, 2001) concerning a 228 mm outer diameter six-pad bearing. The pads are supported by spherical pivots and coated with a babbitt layer less than 1 mm thick. Data for the considered bearing, operating conditions and measurements are given in table 3.1 and figure 3.1. The measurements of temperature and oil film thickness are performed in separate bearing pads.

Calculations of the bearing are conducted using a grid of 30×30 control volumes in the radial and circumferential directions - and in the case of 3-dimensional models 10 control volumes in the z-direction of the oil film and 10 in the z_{pad}-direction of the bearing pad. A uniform collar temperature of 61°C is used. The results are stated in table 3.2. Illustrations of the numerical results are given in figure 3.2. In table 3.2 a measured value of power loss is stated. It represents the total

*The measurements are supplied by Alstom Power (Switzerland) Ltd.

number of pads	6
inner radius	57.15 mm
outer radius	114.3 mm
pivot radius	85.725 mm
pad angle	50.0 °
pivot angle	30.0 °
pad thickness	28.58 mm
oil type	VG46
viscosity at 40°C	39.0 mPas
viscosity at 100°C	5.4 mPas
density	855.0 kg/m^3
thermal capacity	2090 J/kg/K
thermal conduc.	0.13 W/m/K
axial load	52265 N
shaft speed	1500 rpm
Inlet temperature	40°C
Oil flow	15 L/min

Table 3.1: Data for the bearing.

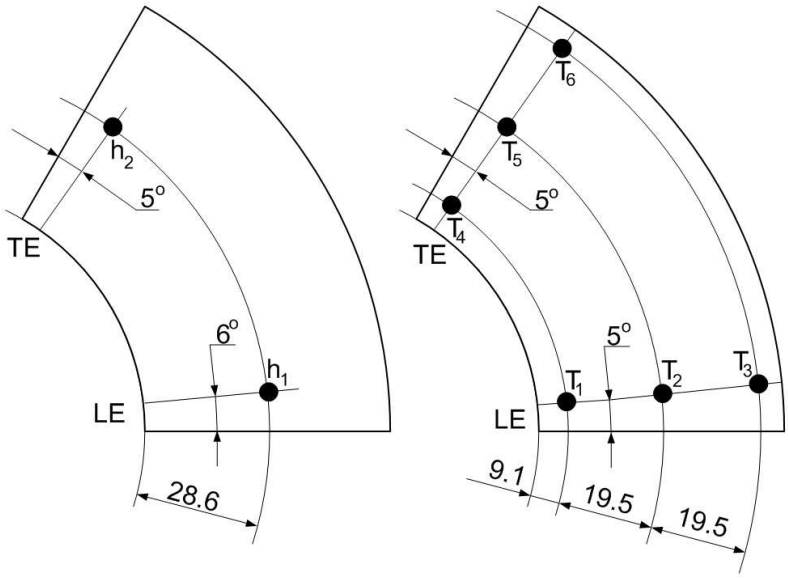

(a) film thickness measurements (b) temperature measurements

Figure 3.1: Locations of measurements are shown. Temperatures are measured in the pad 3 mm below the babbitt layer.

power loss in the bearing and contains losses from the friction between the pads and the collar and losses stemming from the churning of the oil in the oil bath. The calculated power loss does not include churning losses. It can therefore not be directly compared to the measured value.

The 3-dimensional TEHD model predicts a power loss 15 % lower than the measured value. The oil film thickness at the trailing edge is 10 % too high. At the leading edge it is 22 % too small. Calculated temperatures at the leading edge are close the measured ones. At the trailing edge they are 2 to 4 K lower than the measured ones. The temperature rise from the leading to the trailing edge is 15 % smaller than the one measured. The temperature rise from bearing inlet to the trailing edge of the pad is 23.3 K which is 9 % less than the measured value.

Considering the fairly simple treatment of the heat transfer phenomena in the oil bath the calculated temperatures are quite accurate. However, the small temperature rise from the leading to the trailing edge of the pad suggests than one or more of the heat transfer coefficients used in the calculations are too high.

The discrepancies in the oil film thickness show that the calculated pitch angle, α_p is too small. This may partly be caused by a calculated pad deflection which is too small. The pad is considered to be a flat plate of uniform thickness while in reality it has cutouts (Glavatskikh, 2000) at the leading and trailing edges giving larger deflections. Also the pad is considered to be initially flat while it may be slightly crowned due to machining inaccuracies (Glavatskikh et al., 2002). The pressure at the leading edge is set to zero. The velocity boundary layer at the collar surface is however much larger than the oil film thickness at the leading edge. Therefore, the oil is stagnated as it approaches the pad leading to an inlet pressure build-up before the leading edge. Assuming

	experi-mental value	HD-ISO[1]	2D-THD[1] adiab.	2D-THD	2D-TEHD	3D-THD[1] adiab.	3D-THD	3D-TEHD
T_c [°C]	61			61.0	61.0		61.0	61.0
T_{max} [°C]			76.5	70.9	69.6	78.9	70.0	68.9
$T_{max,babbitt}$[°C]				69.9	68.5		69.1	67.8
T_1 [°C]	52			50.8	49.3		55.8	52.4
T_2 [°C]	53			49.5	48.1		56.9	52.4
T_3 [°C]	51			49.7	48.3		55.6	50.5
T_4 [°C]	62			62.2	61.0		62.1	61.0
T_5 [°C]	68			62.9	61.7		65.0	63.9
T_6 [°C]	67			64.9	63.6		66.5	65.1
h_1 [μm]	58	43.6	48.8	47.2	55.6	47.2	30.2	45.5
h_2 [μm]	20	27.2	25.0	24.7	25.5	24.5	19.8	22.1
h_{max} [μm]		53.0	60.2	58.4	71.8	58.3	36.0	58.9
h_{min} [μm]		23.8	19.6	19.9	21.4	19.5	17.9	19.7
Power loss [kW]	3.2			2.71	2.66		3.19	2.73

Table 3.2: Comparison of experimental and numerical results. $T_{le} = \frac{1}{2}(T_c+T_{in})$ in the models marked with[1]. In the other models T_{le} is determined by energy conservation. T_c =61°C is the condition necessary to close the numerical problem.

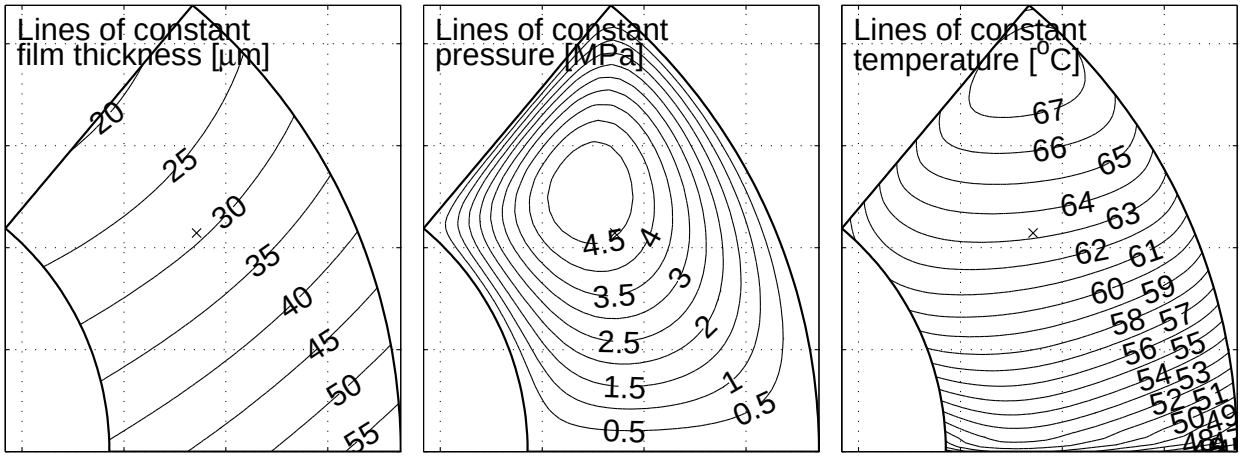

Figure 3.2: Simulation results showing lines of constant oil film thickness (left), lines of constant pressure (middle) and lines of constant pad surface temperature(right).

an inlet pressure larger than zero results in a larger pitch angle reducing the error at the leading edge. A parameter which strongly influences the leading edge film thickness is the leading edge temperature profile. Choosing a uniform temperature in $\overline{z}$ raises the value of h_1 by 8 %. This is due to a higher temperature on the pads surface at the leading edge. This generates a higher deflection

	3D-TEHD				2D-TEHD			
	$15 \times 15 \times (5+5)$	$30 \times 30 \times (10+10)$	$60 \times 60 \times (20+20)$	$120 \times 120 \times (40+40)$	15×15	30×30	60×60	120×120
h_{min} [μm]	20.020	19.714	19.665	19.650	21.681	21.420	21.355	21.324
h_{max} [μm]	60.881	58.870	59.082	59.149	70.689	71.807	72.185	72.235
T_{max} [°C]	68.835	68.897	68.950	68.985	69.505	69.578	69.622	69.662
$T_{max,bab}$ [°C]	67.508	67.754	67.836	67.868	68.829	68.483	68.296	68.208
$\dot{Q}_{gen}$ [kW]	2.6975	2.7259	2.7262	2.7262	2.6499	2.6558	2.6565	2.6570
$\dot{Q}_{out}$ [kW]	2.7598	2.7475	2.7380	2.7335	-	-	-	-

Table 3.3: Grid convergence study: Energy flows are stated per 6 pads, i.e. a full bearing. $\dot{Q}_{out}$ represents the sum of all heat flows out of the computational domain.

of the pad due to higher thermal gradients. Simulations show that the combined effects of inlet pressure build-up and increased deflection due to the effects mentioned above cannot fully explain the errors in oil film thickness. Some effects which are not included in the model may influence the results. There is the possibility that the measuring probes themselves affect the measurements. The eddy-current sensors are embedded in the pad. This involves removal of the babbitt surface over and around the sensors. This area is covered with epoxy. A total of four sensors are located in the pad. The epoxy surfaces cover approx. 10 % of the bearing surface. Two of the sensors are located close to the trailing edge. If the areas in which they are located have a reduced load carrying capacity this would in effect correspond to a pivot point located closer to the trailing edge with a higher tilting-angle as a result. Discrepancies similar to those reported here between measured and theoretical tilting-angles are reported by Glavatskikh et al. (2002) in a comparison between a 3-dimensional TEHD model and measurements conducted using the same test bearing.

In comparison to the results of the 3-dimensional TEHD model the isothermal model overestimates the minimum oil film thickness by 23 %. Considering the simplicity of the model this result is quite good. The 2-dimensional models only slightly over predict the maximum babbitt temperature and minimum oil film thickness compared to the the 3-dimensional models. They estimate pitch angles which are much higher than those calculated by the 3-dimensional models. The pitch angles are close to the one which is experimentally determined. The 2-dimensional and 3-dimensional adiabatic models predict oil film and temperature distributions which only differ slightly. The difference between the models as heat transfer is included is therefore a result of the different accuracy in the description of heat transfer phenomena. And the seemingly more accurate oil film thickness calculations in the 2-dimensional case must therefore be considered to be an accidental effect of less accurate boundary conditions on the energy equation in the z-direction.

Both 2- and 3-dimensional modelling provide good results for the minimum film thickness h_{min} although the predicted pitch angles are very different. The reason is that h_{min} is insensitive to changes in boundary conditions which strongly influence the pitch angle. A higher pitch angle demands a higher mean oil film thickness because of equilibrium with the applied load. Raising the pitch angle while keeping the minimum oil film thickness constant provides a higher mean film thickness. This effect in combination with a higher side leakage causes h_{min} to be insensitive to

raising α_p for the bearing in question.

To determine the minimum oil film thickness and the maximum babbitt temperature a 2-dimensional model seems to be sufficient for the considered bearing. A 2-dimensional integrated description is meaningful only if streamlines are nearly parallel. If the pitch angle is large reverse flow may occur at the leading edge. In cases where reverse flow is significant a 2-dimensional model does not accurately determine the temperature distribution.

Grid convergence studies showing the convergence of key variables for both the 3-dimensional and 2-dimensional TEHD models are shown in table 3.3. For both models the variables are seen to converge as the grid sizes are increased. In the 3-dimensional study the values of generated friction work at the collar surface and the heat transported out of the computational domain converge towards each other. The 30×30 grid which is used in the calculations is shown to be sufficient for the study of the problem.

3.2 Comparison to Measured Data for a Large Sized Bearing

The 3-dimensional TEHD model is applied to a thrust bearing of the Bieudron hydro power plant in Switzerland. Theoretical values of oil film thickness are compared to measurements. A comparison is approximate as details of the thermal conditions of the bearing are scarce rendering it necessary to estimate the collar temperature. An earlier theoretical treatment of this bearing was performed by Santos & Fuerst (2003). Only the steady-state behaviour of the bearing at nominal operating conditions is analysed. I. e. the high-pressure oil injection is turned off.

Figure 3.3(left) shows a picture of the instrumented bearing pad. Measurements of the oil film thickness are performed at the leading and trailing edges in the positions marked with h_1, h_2, h_3 and

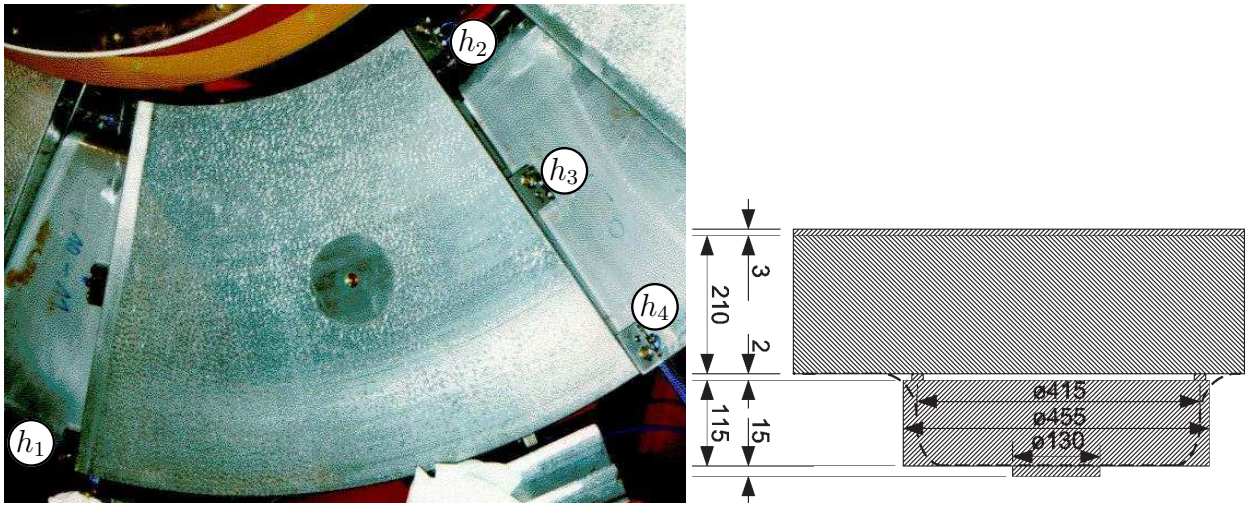

Figure 3.3: Left: The instrumented pad. Right: The dimensions of the ring support (in mm). The dotted line indicates the smoothing function used for the plate thickness. A 3 mm babbitt layer coats the pad.

h_4. The bearing operates using a VG32 mineral oil under fully flooded conditions in combination with a guide bearing. A conical pocket with radius, r_p and maximum depth, $h_{p,max}$ centred at the pivot point allows for hydrostatic lift off. There is a 10 mm, 3° taper at the leading edge. Data for the bearing and oil are: $no_{pads} = 6$, $\theta_0 = 45.31°$, $\theta_{piv} = 27.24°$, $r_1 = 0.527$ m, $r_2 = 1.098$ m, $r_{piv} = 0.8125$ m, $r_p = 0.065$ m, $h_{p,max} = 2.27$ mm, $\mu_{40^oC} = 27.1$ mPas, $\mu_{80^oC} = 6.8$ mPas, $\rho = 848$ kg/m^3, $c = 2090$ J/kg/K, $k = 0.13$ W/m/K, $F_z = 4.94$ MN, $\omega = 44.9$ rad/s, $T_a \approx 40$°C. The collar temperature is unknown. A value of $T_c = 56$°C is used. At this temperature, simulations show that approximately 7 % of the generated heat flows out through the collar. The sensitivity of the solution to changes in the value of T_c is examined later. The bearing pad is firmly mounted on a ring support with a 2 mm gap between pad and support. The geometric data for the pad and support are given in figure 3.3(right). Both pad and support are of steel. As described in chapter 2.2.2 heat transfer in the main pad is considered 3-dimensional while a 1-dimensional description is used for the circular support. As the oil of the gap has a much lower heat transfer coefficient than steel, little heat is transferred across the gap justifying the simplified treatment of heat transfer in the support. Equation (3.1) gives the boundary condition on equation (2.14) inside the area of the support. The solution of equation (2.27) requires continuous first derivatives of D, and therefore a smoothing function is introduced to give the plate thickness shown in figure 3.3(right).

$$\frac{1}{H_{back,eff}} = \left[\frac{1}{H_{back}} + \frac{0.15\text{ m}}{k_{support}} + \frac{0.002\text{ m}}{k_{oil}}\right] \tag{3.1}$$

The Reynolds number in the pocket $Re = \rho\omega r h_p/\mu$ is approx. 4000 at the maximum depth. This indicates turbulence in the deep parts of the pocket enhancing the fluid mixing. Shinkle & Hornung (1965) showed that the transition to turbulence occurs at $Re \approx$1000.

A grid with a final size of $n_r \times n_\theta \times (n_z + n_{z_{pad}}) = 30 \times 30 \times (10 + 10)$ control volumes is used in the simulations.

In table 3.4 a grid convergence study is performed. For three different grid sizes, the study presents key operating parameters for the bearing. The parameters are: friction loss $\dot{Q}_{gen}$, total heat flow out of the computational domain $\dot{Q}_{out}$, the maximum oil temperature T_{max} and the oil film thicknesses h_1 and h_3. Furthermore, pocket specific variables are studied. These are: mass flow into and out of the pocket $\sum \dot{m}_i$ and $\sum \dot{m}_e$, the generated heat in the pocket $\dot{Q}_{gen,p}$, the heat conducted from the pad to the pocket $\dot{Q}_{cond,p}$ and the pocket temperature T_p.

The study is performed both with and without a leading edge taper. The results without a leading edge taper are presented to study the convergence of the heat flows. All other calculations presented in this paper are conducted with a leading edge taper.

The generated friction loss and the total heat flow out of the computational domain converge slowly towards each other. This is due to the leading edge taper, which causes the grid to be very distorted at the leading edge and causes back flow. Consequently, the inflow to the computational domain occurs in only a few control volumes close to the collar. These inaccuracies on the heat flows do not however influence the other bearing parameters significantly and a 30×30×(10+10) grid is considered adequate for the calculations. The heat flows converge more rapidly towards the values of generated work when no leading edge taper is present in the bearing. There is little difference between $\dot{Q}_{gen}$ and $\dot{Q}_{out}$ with a grid of 60×60×(20+20) control volumes indicating that the energy equation is implemented correctly. The generated ($\dot{Q}_{gen,p}$) and conducted ($\dot{Q}_{cond,p}$) heat

	Uniform grid - with 10 mm taper			Uniform grid - without taper		
	$15 \times 15 \times (5+5)$	$30 \times 30 \times (10+10)$	$60 \times 60 \times (20+20)$	$15 \times 15 \times (5+5)$	$30 \times 30 \times (10+10)$	$60 \times 60 \times (20+20)$
General parameters						
$\dot{Q}_{gen}$ [kW]	49.37	49.24	49.38	48.78	49.86	50.15
$\dot{Q}_{out}$ [kW]	63.79	59.54	54.26	49.95	50.10	50.20
T_{max} [°C]	84.97	83.58	83.00	84.64	82.92	82.81
h_1 [μm]	421.7	425.2	427.4	417.5	414.0	418.0
h_3 [μm]	77.65	76.30	76.80	78.18	76.91	77.01
Pocket parameters						
$\sum \dot{m}_i$ [kg/s]	$2.569 \cdot 10^{-4}$	$2.547 \cdot 10^{-4}$	$2.774 \cdot 10^{-4}$	$2.650 \cdot 10^{-4}$	$2.602 \cdot 10^{-4}$	$2.797 \cdot 10^{-4}$
$\sum \dot{m}_e$ [kg/s]	$2.447 \cdot 10^{-4}$	$2.528 \cdot 10^{-4}$	$2.770 \cdot 10^{-4}$	$2.526 \cdot 10^{-4}$	$2.583 \cdot 10^{-4}$	$2.793 \cdot 10^{-4}$
$\dot{Q}_{gen,p}$ [W]	254.8	280.4	305.4	251.2	282.6	305.6
$\dot{Q}_{cond,p}$ [W]	-75.98	-43.46	-57.90	-83.17	-49.42	-64.95
T_p [°C]	63.12	62.52	61.77	62.42	61.31	61.15

Table 3.4: Grid convergence study: Energy flows are stated per pad. $\dot{Q}_{out}$ represents the sum of all heat flows out of the computational domain. $\dot{m}_i$ and $\dot{m}_e$ refer to the mass flow terms of equation 2.10.

T_c [°C]	h_1 [μm]	h_2 [μm]	h_3 [μm]	h_4 [μm]	T_{max} [°C]	$T_{max,babbitt}$ [°C]	$\dot{Q}_{gen}$ [kW]
measurement:							
n/a	430	173	66	202	n/a	n/a	n/a
simulation with pocket included:							
56	425.2	111.6	76.3	122.1	83.6	81.5	295.5
46	428.9	116.4	88.2	128.2	79.6	78.1	327.5
66	421.1	108.4	66.4	117.9	88.6	87.7	272.0
simulation without pocket included:							
56	423.5	114.4	77.7	123.6	83.7	82.7	298.8

Table 3.5: Comparison of experimental and numerical results. T_c is a boundary condition.

in and into the pocket are seen to converge slowly. This is due to the relatively few control volumes covering the pocket. $\dot{Q}_{gen,p}$ and $\dot{Q}_{cond,p}$ are however small compared to the generated heat for the whole pad $\dot{Q}_{gen}$. Therefore, the errors are inconsequential. The pocket temperature converges with increasing grid size. The mass flows into and out of the pocket converge towards each other. This indicates a correct implementation of the pocket equations.

In table 3.5 the simulation results are compared to measurements. For comparison, a pad without an oil injection pocket is also calculated. Additional simulations at varying rotor temperatures are shown as well. A comparison to the measurements shows that the maximum film thickness h_1 is estimated well by the model. h_3 is slightly overestimated and h_2 and h_4 are heavily underestimated.

The discrepancies on the values of h_2 and h_4 may be due to thermal bending of the collar, which is not included in the model.

The theoretical results for pads with and without a pocket differ little. The effect of the pocket on the oil film thickness is small as it covers only 3.6 % of the bearing surface area. When introducing a pocket in the surface the position of the centre of pressure moves towards the centre of the pad causing a higher tilting angle to compensate. The recirculation flow in the pocket causes the temperature downstream of the pocket to be reduced. The maximum babbitt temperature is reduced only slightly by the mixing as it is positioned at a radius outside of the downstream flow of the pocket.

The calculations at collar temperatures of $T_c = 46$°C and $T_c = 66$°C are performed to study the sensitivity of the solution to this unknown parameter. Changes in T_c strongly influence the minimum oil film thickness while the influence on the maximum film thickness is small.

In figure 3.4 the theoretical distributions of oil film thickness, pressure and pad surface temperature are shown. The results are compared to those for a bearing with a plain bearing surface.

In the following a theoretical study of the influence of the pocket dimensions is performed. In figure 3.5 the influence of changing the pocket depth and radius is analysed. Figures 3.5(a)→(d) show pressure profiles, minimum and maximum oil film thickness and friction loss for different pocket radii. The curves are intended to allow designers of bearings with injection pockets to asses the influence of pockets on these key parameters.

In figure 3.5(e)→(h) the influence of the pocket depth on the same parameters is analysed. For the given bearing configuration an increase in pocket depth results in improved performance (reduced friction loss and increased minimum oil film thickness) up to $h_{p,max} \approx 0.15$ mm $\approx 1.1 \cdot h_0$. At this value of $h_{p,max}$ the pressure at the trailing edge of the pocket reaches a maximum - a pressure build-up similar to that of a Rayleigh-step bearing and a flow situation where no recirculation flow in the pocket is predicted by the formulation used. At higher pocket depths recirculation occurs, the pocket does not contribute to the pressure build-up and the loss of bearing area results in a loss of oil film thickness. A similar behaviour is seen when treating a cylindrical pocket of constant depth having the best performance at $h_p \approx 0.08$ mm $\approx 0.6 \cdot h_0$. For decreasing pocket depth, the simulation results converge towards values different from the values obtained when no pocket is present. This is partly due to the different thermal conditions on the pad, as the pad surface in the pocket area is set equal to the pocket temperature. However, mainly it is due to numerical errors, which decrease with decreasing control volume sizes.

The results indicate that machining shallow recesses in the bearing surface could enhance the performance of tilting-pad thrust bearings. Simulations show this to be true also for a bearing in which the pivot position has been optimized for minimal power consumption.

3.3 Conclusion

Comparisons between measurements made in two different bearings and the models presented in chapter 2 have been performed.

Calculations have been carried out to compare with experimental data available in the literature. These are data for steady-state operation of a bearing of 228 mm outer diameter. Simulations show that an isothermal model predicts the minimum oil film thickness within 30 % of the actual value.

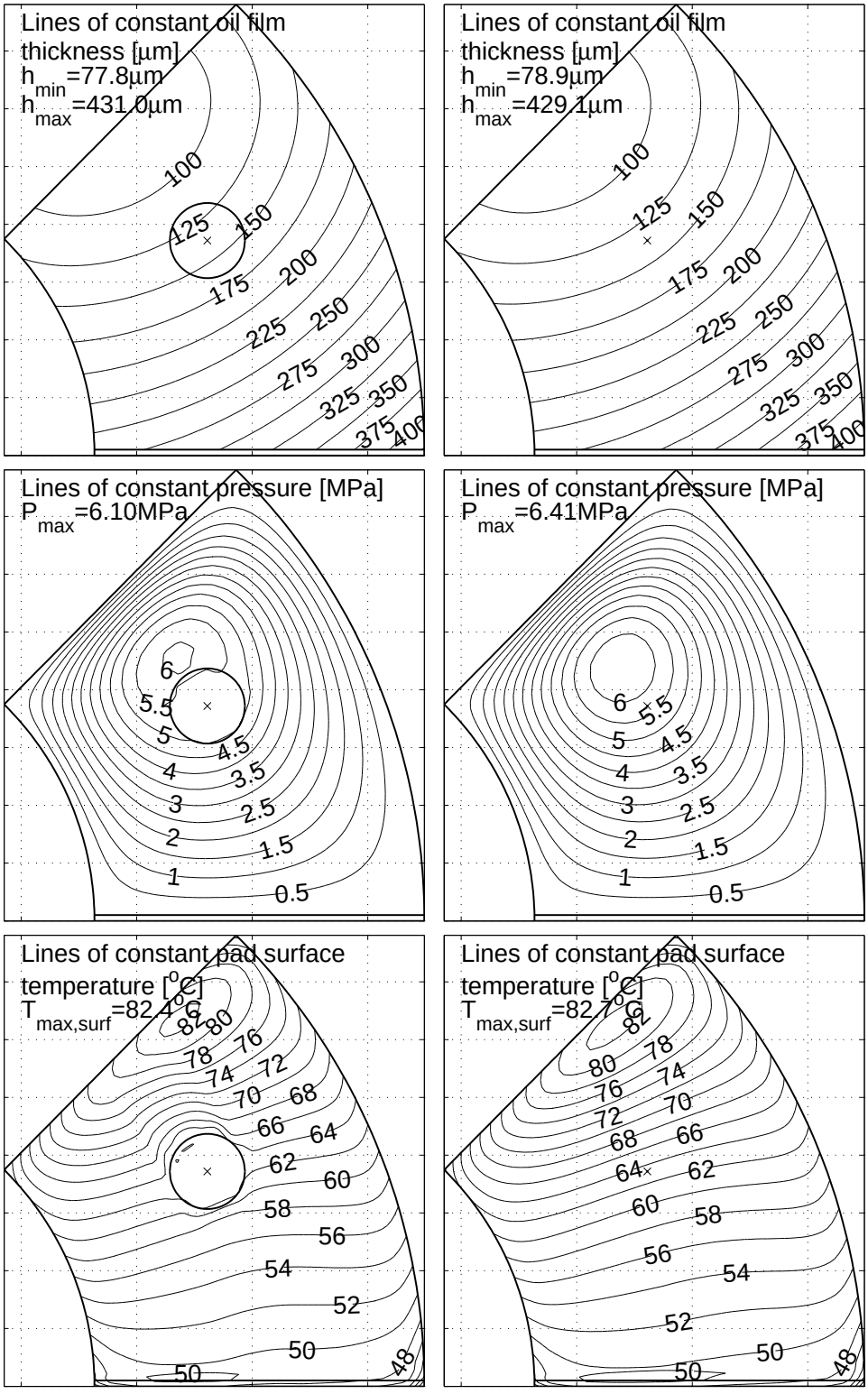

Figure 3.4: Predicted contours of film thickness (top graph), pressure (middle graph) and pad surface temperature (bottom graph) for the studied thrust bearing pads. Left graphs concern the bearing with injection pockets. Right graphs show results for the plain bearing pad. Operating conditions: $\omega = 44.9$ rad/s, $F_z = 4.94$ MN.

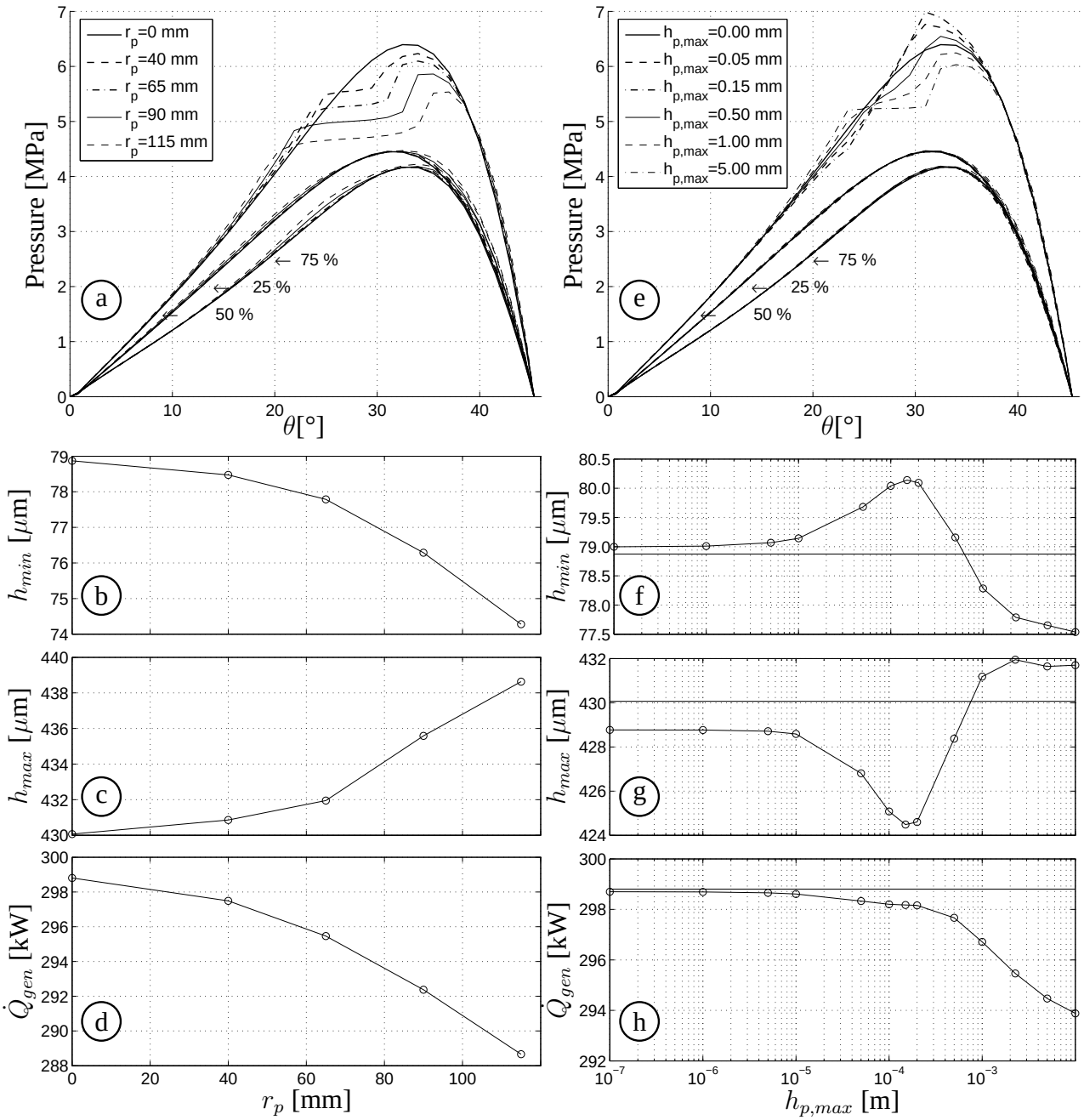

Figure 3.5: Figure showing the influence of varying the pocket width (left) and pocket depth (right). Figure (a) shows the pressure distribution at the 25 %, 50 % and 75 % radial positions for various pocket radii r_p. The pocket radius is varied between zero and 115 mm. In this figure the maximum pocket depth $h_{p,max} = 2.27$ mm is kept constant. Below, the corresponding minimum oil film thickness (b), maximum oil film thickness (c) and friction loss (d) are presented. Figure (e) shows the pressure distribution at the 25 %, 50 % and 75 % radial positions for various maximum pocket depths $h_{p,max}$. The maximum pocket depth is varied between zero and 5 mm. In this figure the pocket radius $r_p = 65$ mm is kept constant. Below, the corresponding minimum oil film thickness (f), maximum oil film thickness (g) and friction loss (h) are illustrated. The horizontal lines in the graphs (f)→(h) represent values obtained for a plain pad without a pocket.

2-dimensional and 3-dimensional models both determine the minimum oil film thickness within 15 % and the temperature rise from inlet to trailing edge within 7 % of the measured values. The temperature distribution is most accurately determined by the 3-dimensional TEHD model. The 3-dimensional models do not improve the accuracy of the theoretical predictions of oil film thickness for this bearing.

Furthermore, the 3-dimensional TEHD model has been applied to the analysis of an existing bearing of large dimensions. The bearing has oil injection pockets at the pivot points. The calculations have been performed at nominal operating conditions with the high pressure injection turned off. The pocket has a surface area of 3.6 % of the total pad area and results in a 1.2 % decrease of the minimum oil film and a 2.2 % increase in the pitch angle compared to a plain bearing pad. Mixing of the oil in the pocket results in cooling of the pad surface downstream of the pocket. The maximum babbitt temperature is only slightly affected by this cooling effect as the hot spot is not located directly downstream of the pocket.

The sensitivity of the results to variations of the diameter of the conical pocket has been studied and the influence on key operating parameters are stated. Similarly, the effect of varying the pocket depth has been analysed. A shallow pocket is shown to improve the performance of the bearing. It contributes positively to the pressure build-up as it has characteristics similar to those of parallel-step bearings. A deep pocket has a negative effect on the performance due to the loss of bearing area.

Further validation of the models with regard to the influence of oil injection pockets and high-pressure oil injection is presented in chapter 4, in which a comparison of theoretically and experimentally determined pressure profiles is performed.

Further validation of the numerical behaviour of the models when using variable grid sizes are performed through grid convergency studies presented in chapters 5, 6 and 7 for different pad geometries.

Chapter 4

Experimental Results

Few papers documenting the influence of injection pockets on the behaviour of tilting-pad bearings have been published. Hemmi & Inoue (1999) presented data documenting the tilting angle as a function of speed for a tilting-pad thrust bearing subject to hybrid lubrication. The pad has two cylindrical injection pockets at the circumferential centre. Yuan et al. (2001) presented a comparison of experimental data and numerical predictions for a large spring-supported thrust bearing with centrally placed ring-shaped injection pockets. The numerical predictions were based on a model developed by Ettles (1991). (Yuan et al., 2001; Ettles, 1991) do not, however, present details of the theoretical implementation of the injection pockets.

This chapter presents a comparison between theoretical results and experimental data obtained in a test-rig for two different bearing pads of approximately 100 cm^2 surface area. One pad has a leading edge taper and an injection pocket. The other is a plain pad without taper or injection pocket. The oil film thickness is measured at the four corners of the pads and pressure is measured in the collar at four different radii. Measurements are carried out at various loads and velocities, with and without constant volume flow, high-pressure oil injection. The test-rig is capable of testing individual pads, not full bearings. Therefore, the thermal boundary conditions such as rotor temperature and leading edge temperature are different from those of full bearings. The test-rig is located at Alstom Power (Switzerland) Ltd., Birr, Switzerland. Earlier Mahieux (2005) published a comparison of data for babbitt, PTFE and PFA coated pads obtained in the test-rig.

Results are given in the form of graphs showing the oil film thickness at the four corner points as functions of load and velocity. Curves of the distribution of pressure are presented for selected measurements showing the change in the pressure profiles as load and velocity is changed. All presented experimental data are compared to the corresponding theoretical values calculated using the 3-dimensional numerical model. Some boundary conditions to the model are adjusted to comply with experimentally determined values. This approach is chosen in order to isolate the comparison between the experiments and the model results to those phenomena which are of interest. For instance, the inlet pressure to a pad is set as a boundary condition in order to compare the pressure profiles along the pad circumference as the primary objective of the comparison is to study the effect of the oil injection pocket.

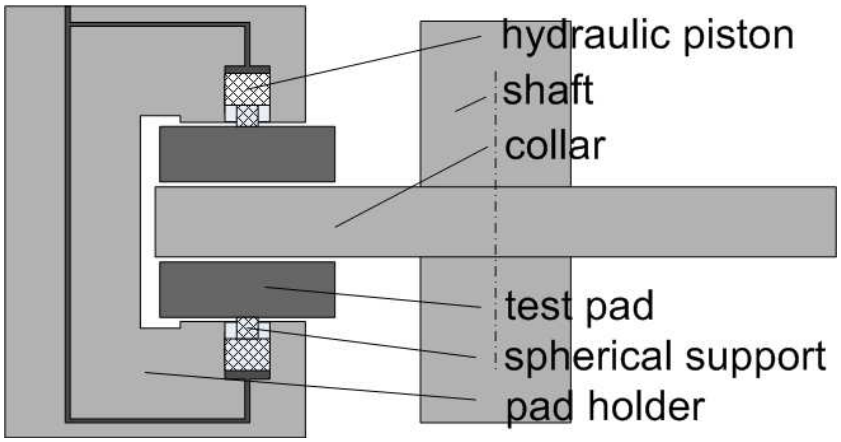

Figure 4.1: Operational principle. The collar diameter is 0.72 m.

4.1 Test Facility

The operational principle of the test rig is shown in figure 4.1. Two pivot pads are hydraulically pressed against opposite sides of a collar. The load is supplied through spherical supports allowing the pads to tilt freely. Movement of the pads in the plane parallel to the babbitt surface is restricted. The oil used is a VG46 mineral oil: $\mu_{40^oC} = 40.1$ mPas, $\mu_{100^oC} = 6.0$ mPas, $\rho_{20^oC} = 872$ kg/m^3, $c = 2090$ J/kg/K, $k = 0.13$ W/m/K. A piston compressor provides a constant volume flow oil injection, which can be varied from 0 to 400 cm^3/min per pad. Measurements are conducted on the lower pad.

4.2 Measuring System

Oil film thicknesses are measured by eddy current sensors mounted at the four corners of the pad, h_1, h_2, h_3 and h_4 as illustrated in figure 4.2. Four transducers placed in the collar at four different radii, p_1, p_2, p_3 and p_4 measure the hydrodynamic pressure distribution. Thermocouples are build in 3 mm below the collar surface at the radii: 283.0 mm, 298.5 mm, 314.0 mm, 329.5 mm and 345.0 mm. The pad dimensions and the positions and sizes of the film thickness and pressure probes are shown in figure 4.2. Two different babbitt (85% Pb, 14% Sb) coated steel (DIN CK45, ASTM 1045) pads are measured. One pad has a leading edge taper and an oil injection pocket at the pivot point. The babbitt coating is 4 mm thick and all edges have a 1 mm chamfer. The other pad is measured for reference. It has no taper, no injection pocket and the edges are not chamfered. The babbitt coating has a thickness of 2.5 mm. The spherical pivot has a radius of curvature of 300 mm. Figure 4.3 shows pictures with details of the test-rig, sensors and bearing pads. The load is determined by measurement of the pressure in the hydraulic load system. 2048 samples of pressure and oil film thickness are made during one turn of the rotor, approximately 114 pressure samples during one pass of the pad. The eddy-current sensors are mounted in holders, which are fixed to the pad by each two bolts as seen in figure 4.3(middle-right). The leading edge holder is of 5 mm moulded plastic. The trailing edge holder is of 2.5 mm aluminium. The pad holder is movable in the radial

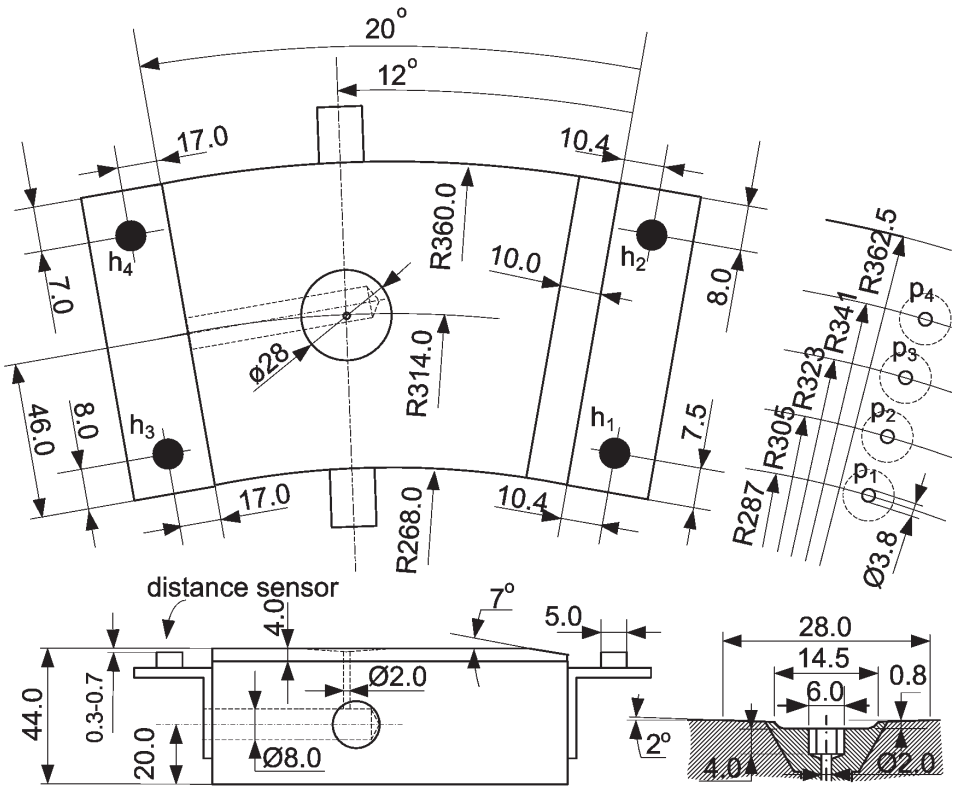

Figure 4.2: Left: The position of sensors and the dimensions of the pad with an injection pocket are shown. all edges have a 1 mm chamfer. Top right: Positions of the pressure sensors in the collar. They are positioned approximately 0.1 mm below the surface. Bottom Right: Cross section of the injection pocket. A brass insert provides the injection piping.

direction in order to ease the changing of bearing pads. The radial positioning is done by eye. The distance of the outer edge of the pad from the shaft centre can therefore vary ± 0.5 mm from the nominal value of 360 mm.

Prior to the measurements the eddy-current sensors are calibrated outside the test-rig using a micrometer screw and subsequently in the test-rig by measuring the output voltages with and without a disk of known thickness between the pad and the collar. Based on these measurements the maximum uncertainty of the distance measurements is estimated to be ± 2 %. The pressure sensors were calibrated when installed, not prior to this set of experiments. A discrepancy between the measured values of the applied load and the pressure distribution is recorded as can be seen in the results section of the paper. The measured value of applied load is $4-10$ % higher than the integrated value of measured pressure over the pad. This discrepancy leads to a $2-5$ % uncertainty on the calculated values of oil film thickness compared to the experimental values. An example of oil film measurements at the trailing edge of the pad is seen in figure 4.4(top). The 2048 measurements cover the circumference of the collar. The change in oil film thickness is a measure for the unevenness of the collar. The measurements with the four sensors vary approx. $40-65$ μm with standard deviations of $\sigma \approx [12, 17, 11, 16]$ μm for the sensors $[h_1,\ h_2,\ h_3,\ h_4]$. The distance measurements represent the

Figure 4.3: Top left: The test-rig. Top middle: The user interface. Top right: Pad shown in a dismounted pad holder. Middle left: A view into the test-rig with a dismounted pad. Middle right: A view of the trailing edge. The distance sensors and the oil injection pipe is seen. Bottom: Pictures of the tested pads taken after the measurements. The plain pad has a ground down surface finish.

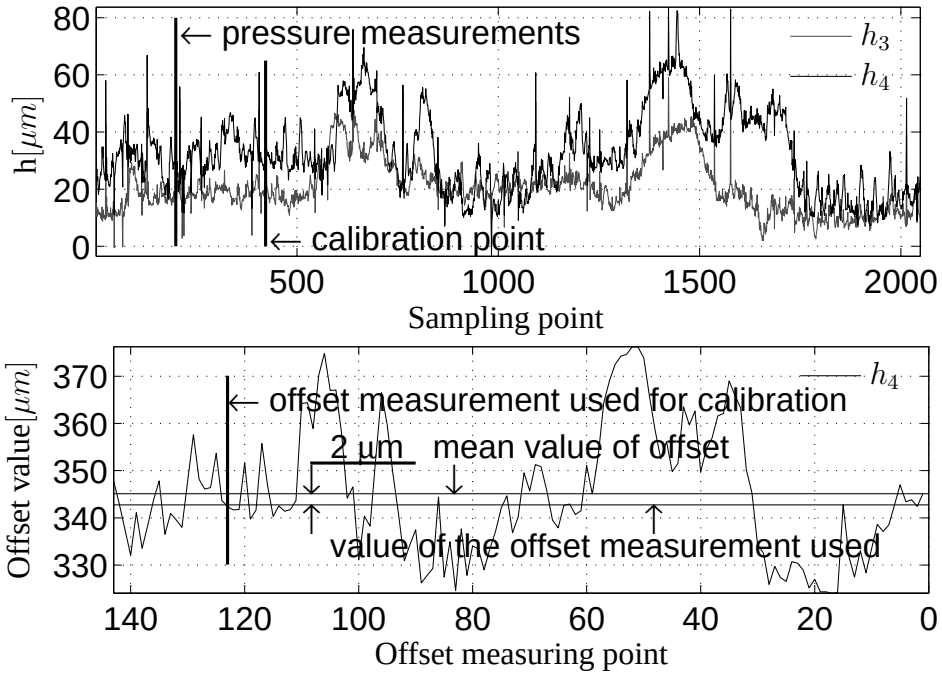

Figure 4.4: Top: An example of trailing edge film thickness measurements (sensors h_3 and h_4). There are 2048 sampling points for one turn of the rotor. The position for the pressure measurements and the position for calibration of the distance sensors are stated. Bottom: Distance from collar to sensor h_4 at 143 evenly spaced points on the collar circumference. The pad is pressed against the collar. Offset measurement 123 is used for calibration of the distance sensors.

distances from the sensors to the collar surface subtracted calibration values measured with the pad pressed against the collar. Figure 4.4(bottom) shows the distance from an eddy-current sensor to the collar at 143 evenly spaced positions around the collar circumference. The pad is pressed against the collar. The graph shows variations similar to those of the 2048 film thickness measurements. To accurately determine average values of oil film thickness the offset values used for calibration of the sensors are always determined in the same position of the collar (measuring point no. 123). The measured offset in this position does not represent the mean offset distance from the collar. The calibration-offset value is therefore corrected to represent the mean distance. E.g., 2 μm is added to the calibration-offset value for sensor 4 as described in figure 4.4(bottom). With these corrections, the mean value of the 2048 sampling points represents the average film thickness. The calibration is done at the operating temperature as the axial position of the sensors move up to 0.5 μm/K when changing the oil bath temperature due to thermal expansion of the sensor holders and bolts.

Data are presented for pads operating at 40°C oil bath temperature, loads of 15 and 40 kN and velocities varying from the minimum possible for each load to a maximum of 1000 rpm. The pad with an injection pocket is measured without and with 400 cm^3/min constant volume flow oil injection. At each operating condition, the measurements are carried out when the thermal conditions have stabilized. Thermal equilibrium is achieved within a couple of minutes.

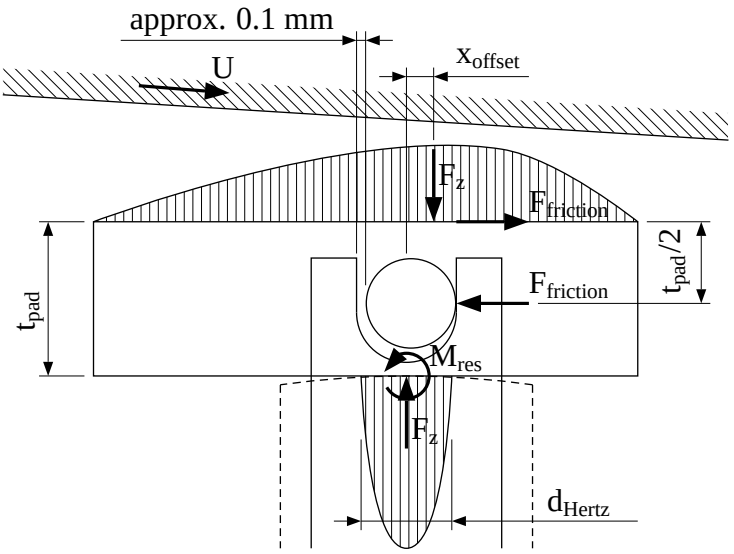

Figure 4.5: Illustration of the forces acting on the pad. The pressure distribution in the oil film and the Hertzian pressure distribution between the spherical support and the pad are indicated. The centres of the pressure distributions are shown as F_z. The centres are offset by x_{offset}. A resulting moment M_{res} in the pivot point is therefore necessary.

4.3 Simulations

Simulations are carried out for comparison. The pad with a pocket is simulated as a pad of $\theta_0 = 19.64°$, $\theta_{piv} = 11.82°$, $r_1 = 269$ mm, $r_2 = 359$ mm and a 9 mm taper at the leading edge. Thus, the dimensions of the test pad are reduced by the 1 mm chamfer on all edges. The pad is modelled as a solid steel plate of 40 mm thickness. The influence of the babbitt layer is neglected. All other dimensions are as stated in figure 4.2. The boundary conditions are as follows: The collar temperature is set equal to the mean value of the five experimental collar temperature measurements. The scatter between the five measurements is generally less than 1 K. The leading edge temperature profile is set uniformly equal to the collar temperature. As both the laminar velocity- and temperature boundary layers grow to thicknesses much larger than the leading edge oil film thickness it is reasonable to assume the temperature variations in the axial direction to be small justifying the choice of boundary condition. A grid of 30×30×(10+10) control volumes is used.

The force and the moment acting at the centre of the spherical pivot can be calculated from the experimentally determined pressure curves. The curves are extrapolated to a grid covering the pad and numerically integrated. As will be shown in the results section of this paper the moment is not zero as it is assumed in the theoretical description of the problem. Figure 4.5 shows a schematic illustration of the forces acting on the pad. The measured pressure profiles indicate centres of pressure located to the trailing edge side of the pivot point. Assuming the Hertzian pressure distribution on the interface between the spherical pivot and the pad to be symmetrical around the centre of the pivot there must be a resulting moment M_{res} acting at the pivot point. As an example, the forces and moments are stated for the operating conditions: $F_z = 40$ kN, $\omega = 1000$ rpm. The force determined from the numerical integration of the pressure curves is $F_z = 37.3$ kN and the resulting moment is $M_{res} = 108$ Nm. From the theoretical solution the friction force is calculated to be $F_{friction} = 133$ N

generating a moment of 2.7 Nm in the same direction as that of the pressure distribution. It is 2.5 % of M_{res} and its influence is negligible. The diameter of the Hertzian pressure distribution between the pad and the spherical support is calculated to be $d_{Hertz} = 8.5$ mm. The resulting moment may be generated by external forces acting on the pad but not included in the analysis or it could be a result of an offset of the centre of pressure of the Hertzian pressure distribution. The origin of M_{res} is not known. In this report however, it is treated as an offset of the pivot point, which for the presented example is $x_{offset} = 2.9$ mm representing 2.6 % of the pad length. The rolling motion of the pad on the spherical pivot will move the pivot position in the direction of the leading edge and give a negative value in the figure. This effect is negligible as it moves the pivot point only a few tenths of a millimetre. Five sets of measurements with the plain pad at the same nominal operating conditions (16 kN, 400 rpm) have been made. In between the measurements, the pad was built out of the test-rig. The calculated offsets: [3.9, 2.4, 2.9, 2.7, 3.8] mm vary by 1.5 mm. The reason for the offsets could be construction tolerances in the moving parts of the supporting structure. Possibly the hydraulic piston positions itself at an angle in the cylinder causing the spherical pivot to be angled as well. A chain of tolerances of the necessary magnitude is however not found.

The values of F_z and θ_{piv} used as input parameters for the calculations are determined to comply with the experimental results. The values are calculated using numerical integration as described in the previous paragraph. Similarly, the inlet pressure is adjusted to comply with the experimentally determined value. This approach is chosen because the main aim of comparing measurements with calculations is to validate the numerical model with regard to its ability to determine the pressure distribution when a pocket is present in the pad surface. The adjusted input parameters are external to the oil film and using the nominal values makes it difficult to evaluate the effect of the pocket because the shapes of the theoretically and experimentally determined pressure profiles are different. For comparison however, data are also presented using the nominal values of F_z and θ_{piv}.

4.4 Comparison between Experimental and Theoretical Results

4.4.1 Pressure profiles

Pressure profiles for selected measurements are compared to theoretical values in the figures 4.6 to 4.8. Figure 4.6 shows curves for the plain pad operating at 15 kN, 600 rpm. In figure 4.6(a) the nominal values of load and pivot position are used in the calculations. In the calculations of figure 4.6(b) the pivot is moved 2.1 mm towards the trailing edge to achieve moment equilibrium with the measurements and the load is reduced to the experimentally determined value. The discrepancies between the measured and theoretical pressure profiles are much smaller when the pivot point is moved and the applied load adjusted. Similar good agreement between the theoretically and experimentally determined pressure curves is found for the plain pad at all other operating conditions treated in this report. The figures 4.7 and 4.8 show theoretical pressure profiles obtained using input parameters adjusted to give zero moment and force differences between calculations and measurements. The input data for these corrected simulations are stated later.

In figure 4.7 curves are shown for the pad with a pocket with the high-pressure injection turned off. The influence of the pocket is larger at small oil film thicknesses, i.e. at high loads and low speeds. The pocket stretches from approx. $\theta_{piv} = 10° \rightarrow \theta_{piv} = 14°$. There is a significant pressure

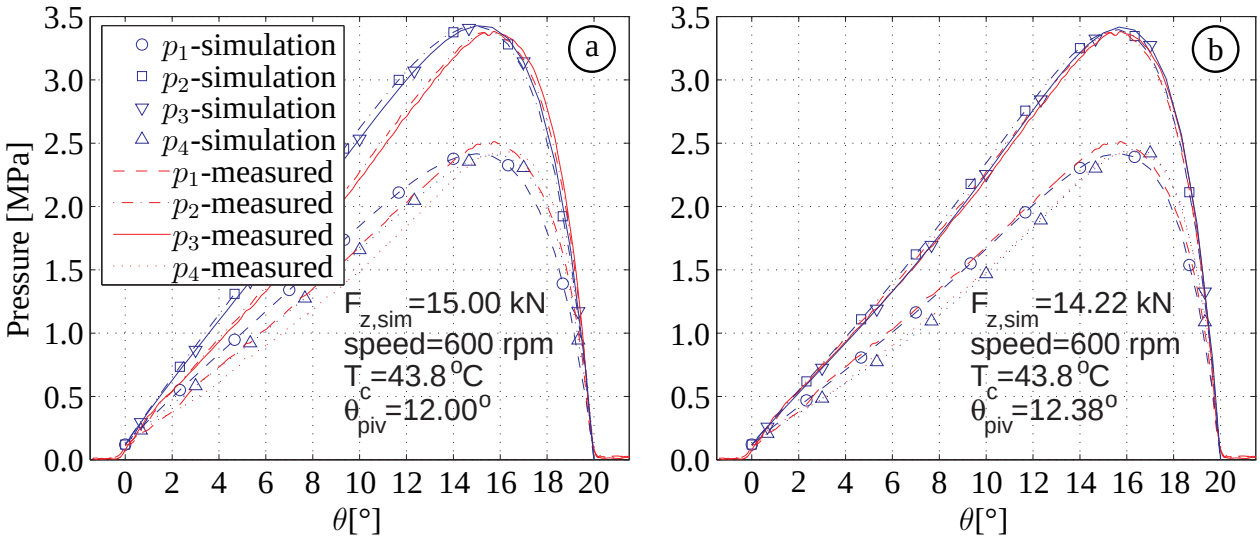

Figure 4.6: Comparison of measured (red lines) and simulated (blue lines) pressure profiles for the plain pad. Calculations in (a) are performed with nominal operating conditions. In (b) the pivot point is moved and the load reduced to give force and moment equilibrium with the measurements. The line legend shown in the left figure also applies to the figures 4.6(b), 4.7 and 4.8.

build-up in this area at a load of 15 kN. At 40 kN where the depth of the pocket is larger relative to the oil film thickness the build-up is smaller. The theoretical and the experimental curves do not correspond as well to each other as in the case of the plain pad. The general shapes of the pressure profiles are described well at $F_z = 15$ kN. The measurements with sensors 3 and 4 are higher than the ones with sensors 1 and 2. This indicates that the pad is pivoted so that the oil film thickness at the outer radius is smaller than at the inner radius. At high loads, the simulated pressure profiles are less accurate. The predicted maximum pressure is smaller than the experimental value by 10 % as the model under predicts the pressure rise after the pocket.

In figure 4.8 oil is injected at a volume flow of 400 cm^3/min. At the load of 15 kN shown and at all presented velocities the pressure curves are well described by the theoretical model. Again, the measured pressure profiles indicate that the pad is tilted to give a smaller oil film thickness at the outer radius. In figure 4.8(a) the constant pressure indicating the position of the pocket is seen to have a larger circumferential extend for sensor 3 compared to sensor 2. This indicates that the pad is positioned slightly inaccurately in the radial direction.

The simulated pressure profiles shown in figures 4.7 and 4.8 under predict the influence of the pocket. This is especially clear at high loads whereas the discrepancies are small at low loads. Inside the pocket, the measured pressure rises little followed by a steep rise after the pocket. The theoretical model predicts a steeper pressure rise inside the pocket and subsequently a lower pressure rise after the pocket.

As the pressure profiles for the plain pad show good agreement with the theoretical results it is natural to assume that the discrepancies seen in figure 4.7(c) and (d) are results of a poor description of the pocket influence by the model used. In figure 4.9, however, a comparison of measured pressure profiles is made for three different pads. Results for a pad without a pocket but with a taper are included. The pad is seen in figure 4.10. It has a surface finish similar to that of the pad

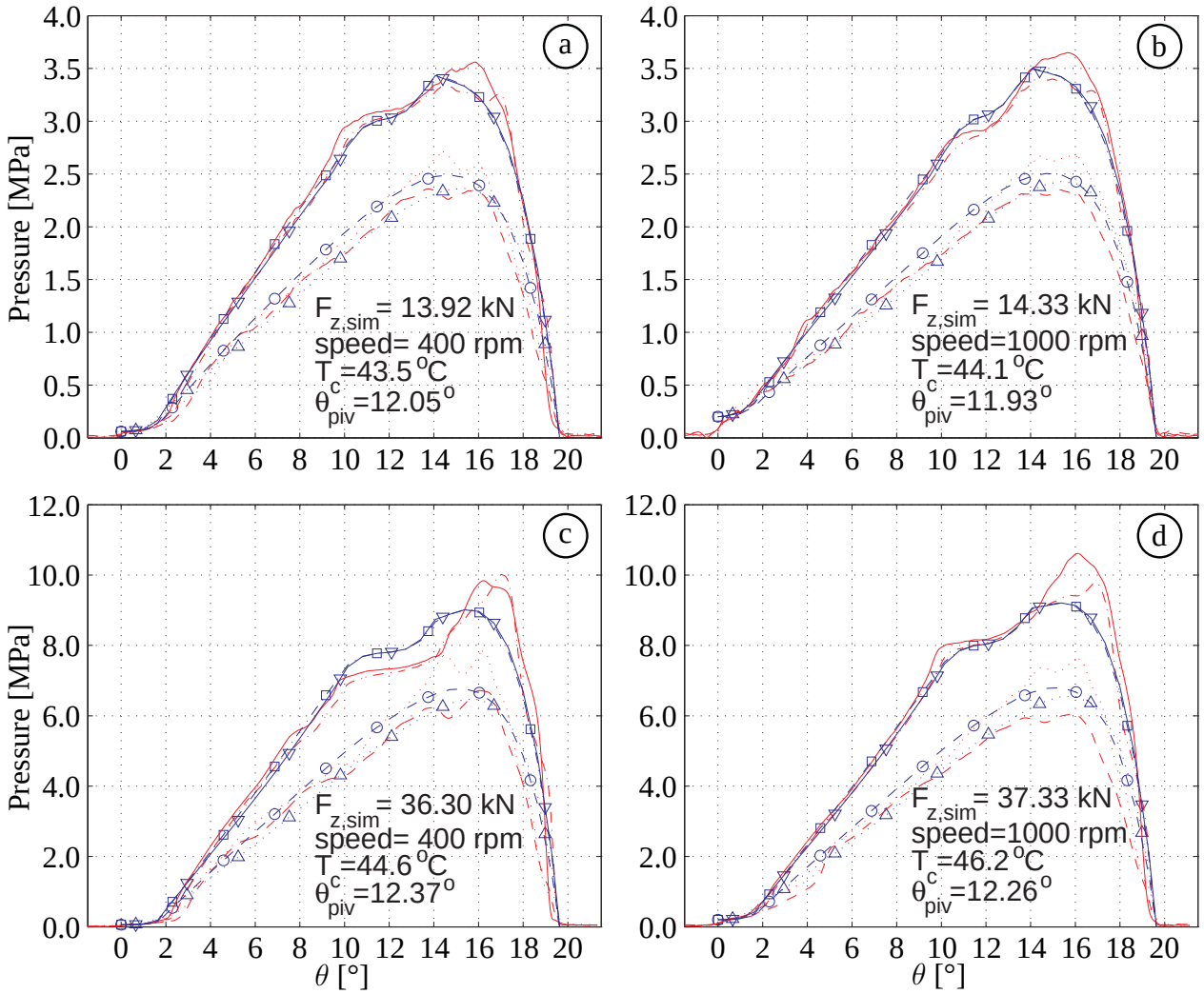

Figure 4.7: Comparison of measured and simulated pressure profiles for selected operating conditions for the pad with an injection pocket.

with an injection pocket. The pressure profiles for the plain pad with an inlet taper behave in a way similar to those for the pad with a pocket. In both cases a drop and subsequently a rise in pressure is seen at $\theta = 14 - 16°$ for the sensors 1 and 4. This may be a result of the unevenness of the collar as it is described in figure 4.4. The plain pad without taper has a higher $h_{max}/h_{min}-$ratio and it is therefore less likely that the unevenness of the collar will result in a diverging oil film for this pad. The unevenness of the collar has an increasing influence as the oil film thickness becomes smaller and it may therefore contribute to the discrepancies between the theoretical and experimental results, which are seen in figures 4.7(c) and 4.7(d). Furthermore, the surface finish may influence the results. The plain pad without a taper has grinding tracks in the direction of motion. These tracks inhibit the flow perpendicular to the tracks and thereby reduce the pressure fluctuations seen in the measurements of the other two pads.

The simplified flow description, which follows from using the Reynolds equation, neglects terms that may significantly influence the flow in the pocket. Changes in inertia at the edges of the pocket

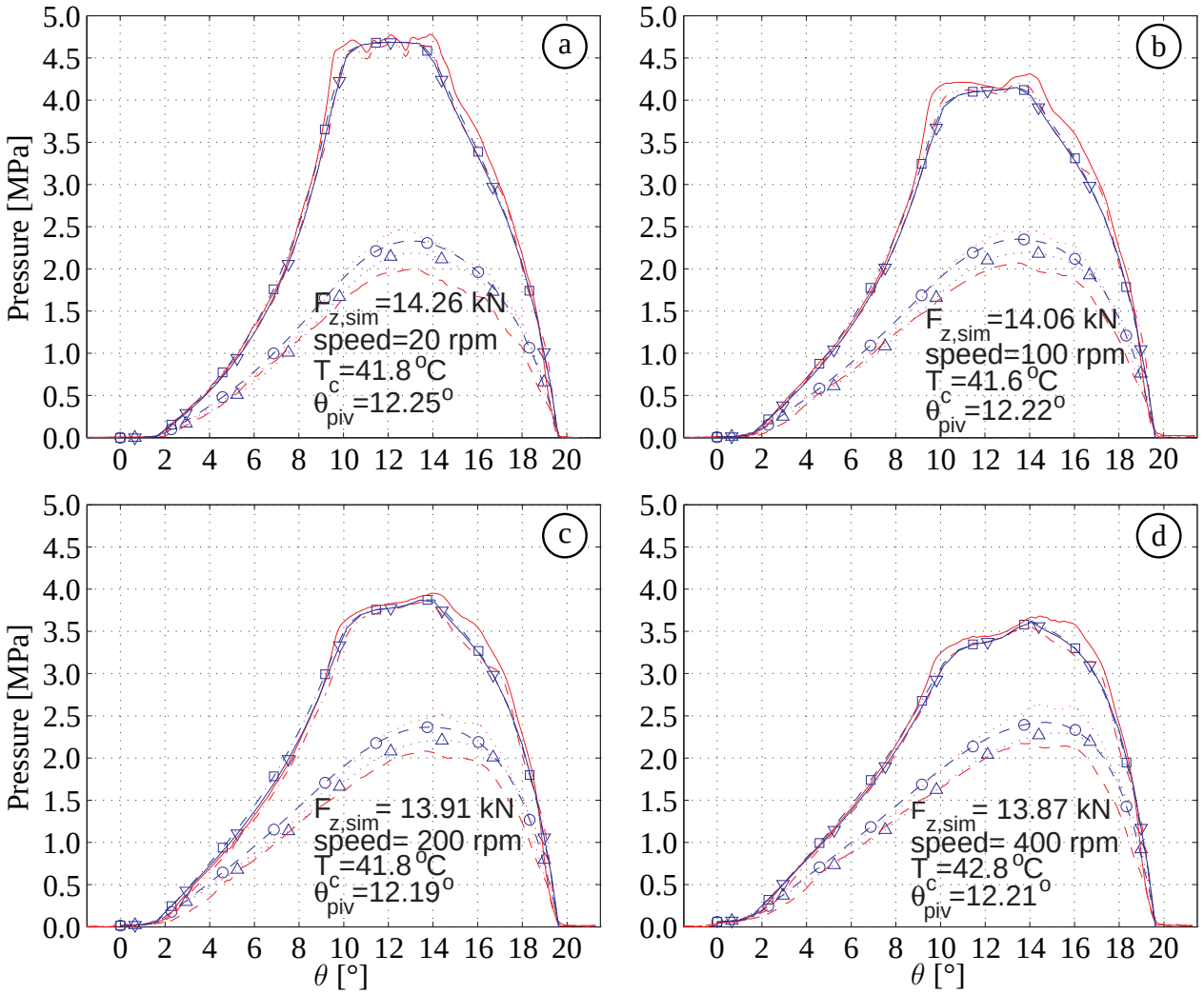

Figure 4.8: Comparison of measured and simulated pressure profiles for selected operating conditions when oil is injected at a flow rate of 400 cm^3/min.

result in reduced pressure at the leading edge of the pocket and a rise in pressure at the trailing edge. This is a result of the recirculation flow in the pocket accelerating the oil entering the pocket. Ettles & Donoghue (1971) discussed this. Simulations for 15 kN, 1000 rpm show an acceleration of the oil at the mean radius from an average speed of $0.45U$ before the pocket leading edge to more than $0.95U$. The influences of inertial changes are likely to increase in importance as loads are lowered and speeds are raised. The discrepancies between the theoretical and experimental pressure curves do not, however, increase with the velocity and it is concluded that the large discrepancies seen in figures 4.7(c) and 4.7(d) are results of other factors than inertial effects.

4.4.2 Oil film thickness

Film thickness measurements and simulations are compared in figure 4.11. The gradients $dh/d\theta$ at the leading and trailing edges of the pad are used to linearly extrapolate the simulated oil film

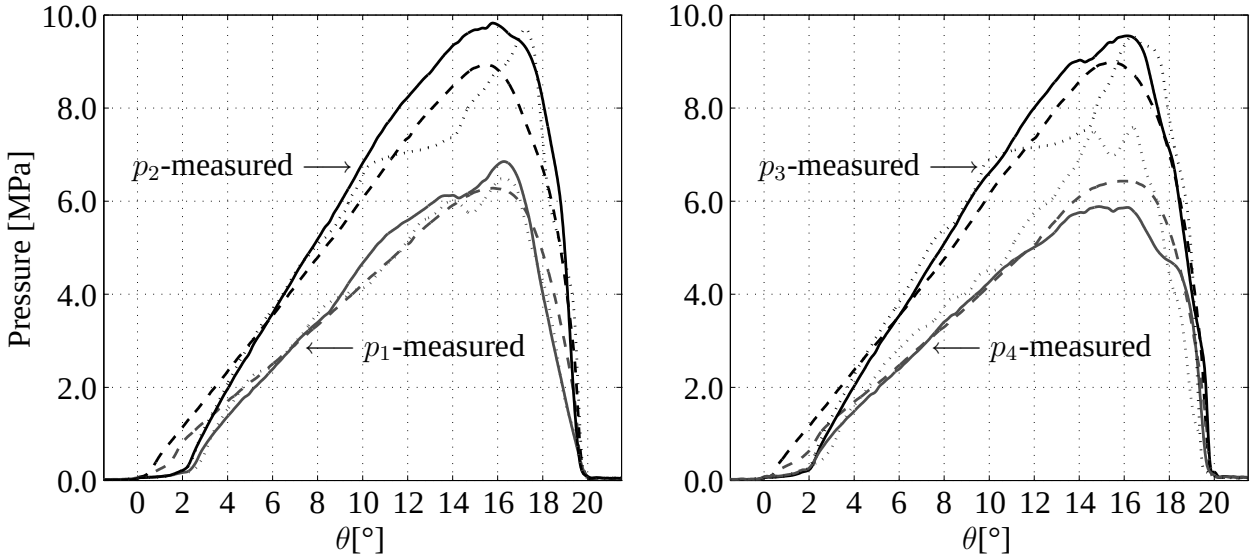

Figure 4.9: Comparison of measured pressure profiles for pad without taper or injection pocket (dashed lines), pad with taper but no injection pocket (full lines) and pad with taper and injection pocket (dotted lines) operating without oil injection at 39 kN, 400 rpm. Left: p_1- and p_2-measurements. Right: p_3- and p_4-measurements.

thicknesses to the measuring points. Simulation values are shown using nominal values (e.g. $F_z =$ 15 kN, $\theta_{piv} = 12°$) and also using values corrected to give zero force and moment deficits between calculations and measurements (e.g. $F_z = 14.2$ kN, $\theta_{piv} = 12.38°$).

For the plain pad, the experimental values of leading edge oil film thickness correspond well with the simulations. The model less accurately determines the trailing edge values. As the load is increased, the discrepancies become larger. Thus, for the plain pad, the simulated values of h_3 and h_4 are 9 μm or 25% lower than the experimental values at 40 kN, 1000 rpm. Similar discrepancies are seen both with and without oil injection for the second pad. The reason for this discrepancy is probably a measuring error. As earlier stated the distance sensor holders move due to thermal elongation of the pad, sensor holders and bolts. The temperature in the pad increases with load and velocity and therefore the possible inaccuracy due to this phenomenon also increases. Simulations predict the mean pad temperature at the trailing edge to be 63°C at 40 kN, 1000 rpm. As the sensors move up to 0.5 μm/K this corresponds to a 12 μm inaccuracy on the measurements of the oil film thickness. At these operating conditions, the measured oil film thickness is approx. 30 μm at the

Figure 4.10: Plain pad with taper.

velocity [rpm]	200	400	600	800	1000
$F_{load} = 15$ kN	error estimate [μm]				
leading edge	1	2	2	2	2
trailing edge	3	5	6	7	7
$F_{load} = 40$ kN					
leading edge	2	2	3	3	3
trailing edge	3	7	9	11	12

Table 4.1: Error estimates on the measured oil film thickness

trailing edge. The calculations are approx. 9 μm smaller. The results deviate with 75 % of the estimated accuracy. Estimates of the error at all the operating conditions stated in the figure are given in table 4.1. The thermal conditions are similar for the two pads so the estimates apply to both. The errors seen in figure 4.11 on the trailing edge oil film thickness are within the range given in table 4.1. The leading edge errors are larger than those predicted.

For the pad with a pocket, the theoretical thicknesses of the oil film do not correspond as well to measurements as those for the plain pad. At the trailing edge, the experimental values are higher at the inner radius than at the outer radius indicating that the pad is tilted radially. This was also seen in the pressure measurements in the figures 4.7 and 4.8. The theoretical values indicate a slight tilt in the other direction.

The results with high-pressure injection in figure 4.11(c) and (f) show a reasonable agreement between the measured and calculated values of trailing edge oil film thickness as the velocity goes towards zero. This good agreement is achieved with the input data corrected for force and moment deficits. With the nominal values of load and pivot position, the trailing edge oil film thickness is much higher. This shows that the behaviour of the pad during start-up with high-pressure oil injection is sensitive to the position of the pivot. Calculations predict oil film thicknesses at zero velocity of $[h_3, h_4]_{15kN} = [25, 24]$, $[h_3, h_4]_{40kN} = [18, 18]$ at the nominal conditions while the values are $[h_3, h_4]_{15kN} = [9, 7]$, $[h_3, h_4]_{40kN} = [9, 8]$ at the corrected pivot locations.

In figure 4.12 the inputs data for the numerical model are stated. Figure 4.12(a)$-$(b) present the loads applied in order to achieve zero force deficits between the measurements and the theoretical results. At 15 kN nominal load, the loads determined from the oil film pressure measurements are $1 - 11$ % smaller. The mean value in figure 4.12(a) is 6 % lower than the nominal value. At 40 kN nominal load, the loads determined from the pressure measurements are $4 - 9$ % smaller. The mean value in figure 4.12(b) is 6 % lower than the nominal value. In figure 4.12(c) the offsets in the angular direction of the pivot point which are used in the simulations are stated. The offsets vary between 0.6 and 3.4 mm in the direction of the trailing edge. This corresponds to $0.5 - 3.1$ % of the pad length. The resulting moment acting at the nominal position of the pivot point can be calculated from figure 4.12(a)$-$(c). Figure 4.12(d) and (e) show the leading edge pressure and the rotor temperature used in the calculations. These input parameters are set equal to measured values. At high velocities, the leading edge pressure is smaller by approx. 25 % when the pad has a taper.

In figure 4.13 simulation results are shown for a pad operating at 14 kN, 400 rpm. The volume of the pocket significantly affects the temperature distribution. The effect is probably larger than it would be in most bearings because the collar temperature in the test-rig is relatively low in

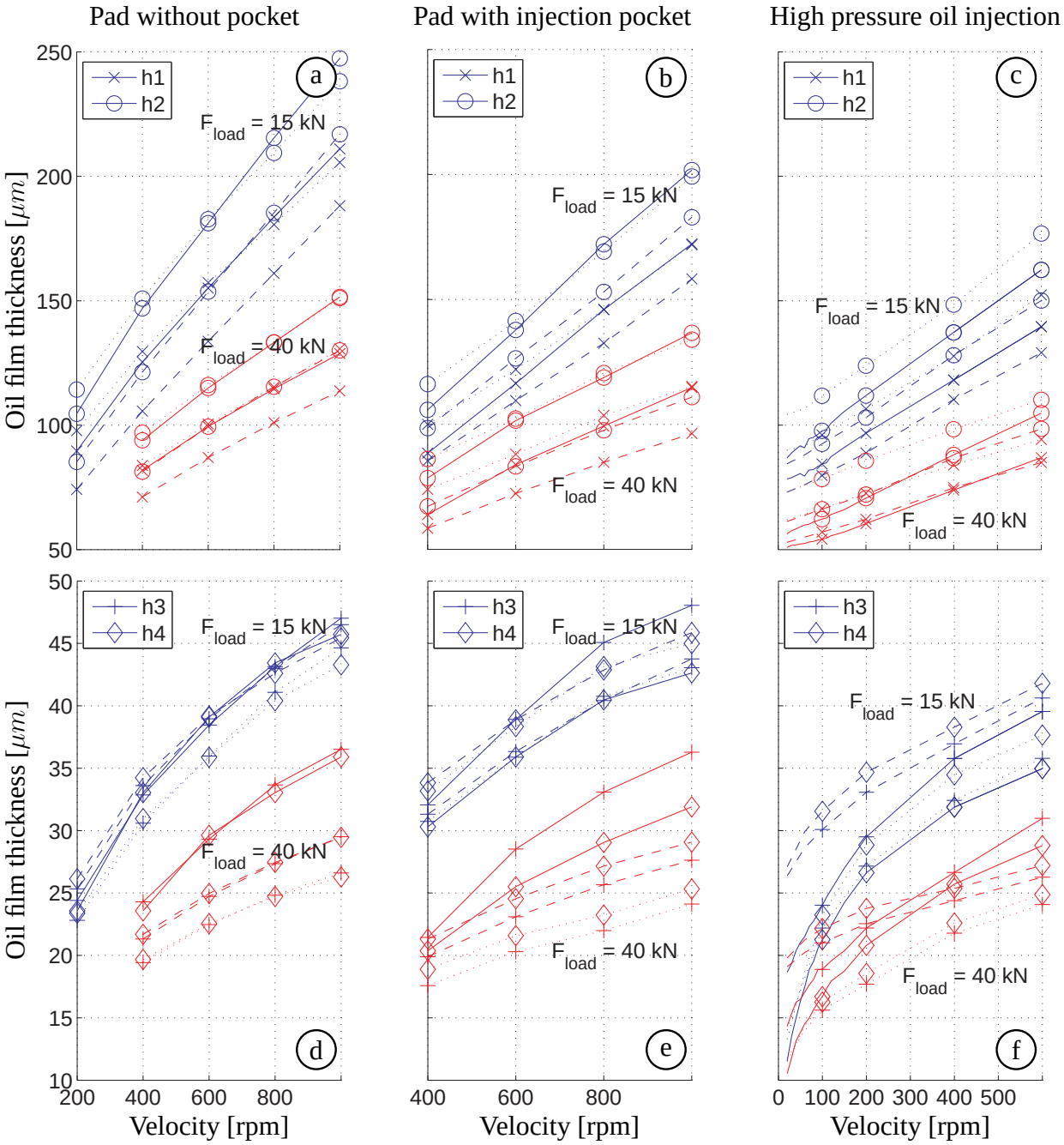

Figure 4.11: Comparison of measured and calculated oil film thicknesses. (Full lines: Measurements. Dashed lines: Calculations using nominal values of F_z and θ_{piv}. Dotted lines: the pivot point is moved and the load reduced for force and moment equilibrium with the measurements.) Top figures show leading edge film thicknesses. Bottom figures present trailing edge values. Figures (a) and (d): Results for the plain pad. Figures (b) and (e): Results for the pad with a pocket. The oil injection is turned off. Figures (c) and (f): Results with 400 cm^3/min oil injection. Symbols: $\times$, O, $+$ and $\diamond$ represent measured values. Additionally, measurements are performed with intervals of 10 rpm from the minimum possible of 20 rpm to 120 rpm for the pad operated with oil injection.

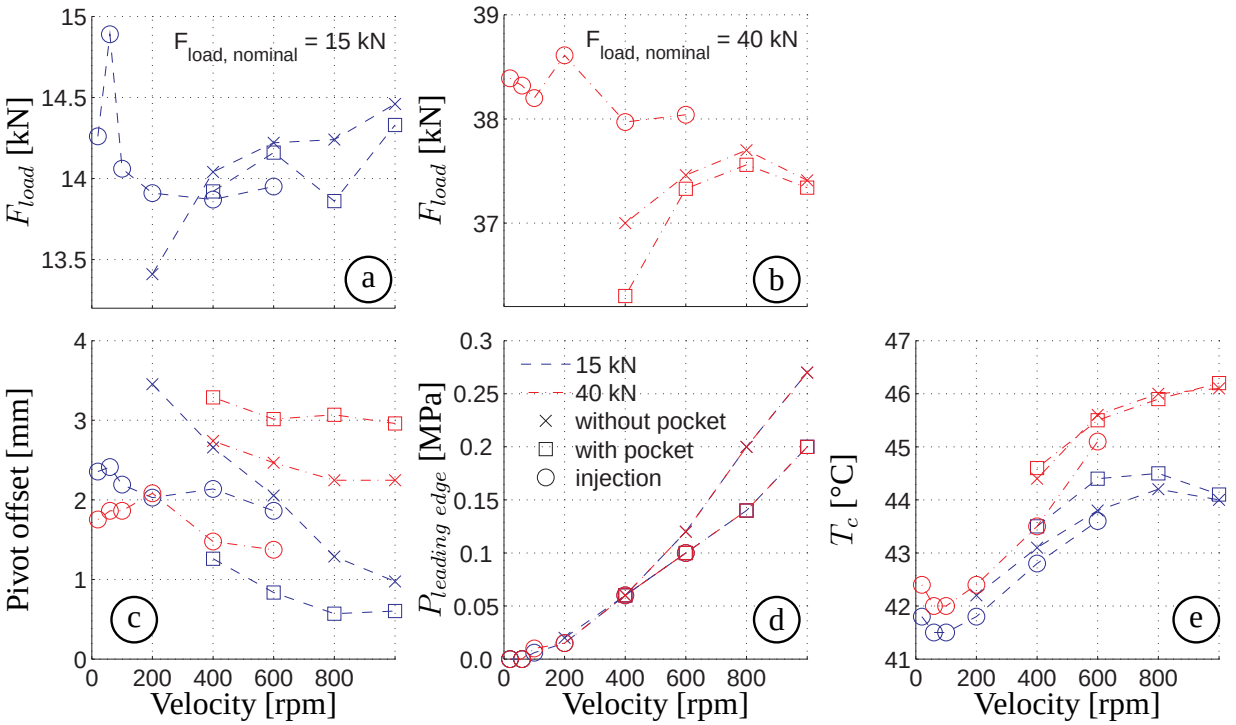

Figure 4.12: Input data for the calculations in which the pivot point and the load are adjusted for moment and force equilibrium with the measurements. The nomenclature for all figures is defined in (d). Figure (a) illustrates the loads used when the nominal condition is a load of 15 kN. Data for various collar speeds and three bearing configurations are given: pad without pocket '×', pad with pocket but without high-pressure injection '□' and pad with pocket and 400 cm^3/min oil injection 'O'. Figure (b) illustrates the same data for a nominal load of 40 kN. Figure (c) presents the pivot offsets resulting in moment equilibrium with the measurements. Figure (d) shows the leading edge pressures determined form measurements and used in the calculations. Figure (e) shows the measured collar temperatures used as a boundary condition in the calculations.

comparison with the maximum temperature in the babbitt layer.

An experimental study of the influence of oil injection is presented in figure 4.14. The oil film thicknesses measured with oil injection turned on are compared to those measured with no high-pressure injection. At a load of 15 kN the oil injection raises the mean film thickness by 14 μm at 600 rpm and by 18 μm at 400 rpm. At a load of 40 kN it raises the mean film thickness by 3 μm at 600 rpm and by 7 μm at 400 rpm. The change in the tilting angle depends on the operating conditions. At both 400 rpm and 600 rpm, it results in a higher kip angle at a load of 15 kN. The kip angle is reduced at $F_z = 40$ kN when the high-pressure oil injection is turned on.

4.4.3 Lift-off oil film thickness

In figure 4.15 a comparison between measured and theoretical lift-off height is shown. The measurements are performed by hydraulically pressing the pad against the collar and measuring the offset of

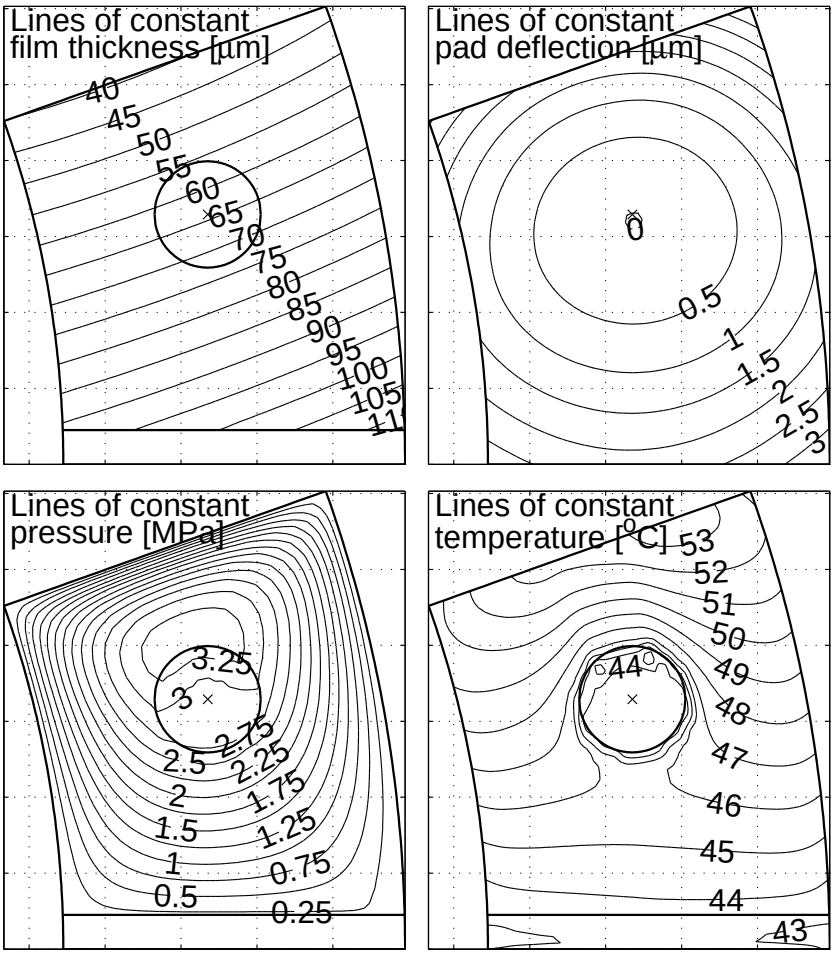

Figure 4.13: Theoretical values of oil film thickness, pad deflection, pressure and babbitt temperature for a pad operating at: $F_z = 13.92$ kN, velocity$= 400$ rpm, $\theta_{piv} = 12.05°$

the distance sensors. Subsequently the offset is measured with the high-pressure injection turned on. The differences between the offset values are shown in the figure. Eight measurements at random positions on the collar are performed at each load. The corresponding simulations are performed with a speed of 0.01 rpm, a collar temperature of 40 °C and with the nominal values of load and position of the pivot. The results are higher than the experimental values. This is as expected as the unevenness of the collar causes a remaining layer of oil between the pad and collar when the initial offset measurement is performed. The errors between the theoretical values of oil film thickness and the measured values are within the values of the standard deviations on the variation on the collar surface $\sigma \approx [12, 17, 11, 16]$ μm for the sensors $[h_1,\ h_2,\ h_3,\ h_4]$ as they were calculated in section 4.2. Assuming the pivot located further towards the trailing edge could explain the differences in the measured and calculated trailing edge oil film thickness. As was previously shown, the trailing edge lift-off film thickness is very sensitive to small variations in the pivot location.

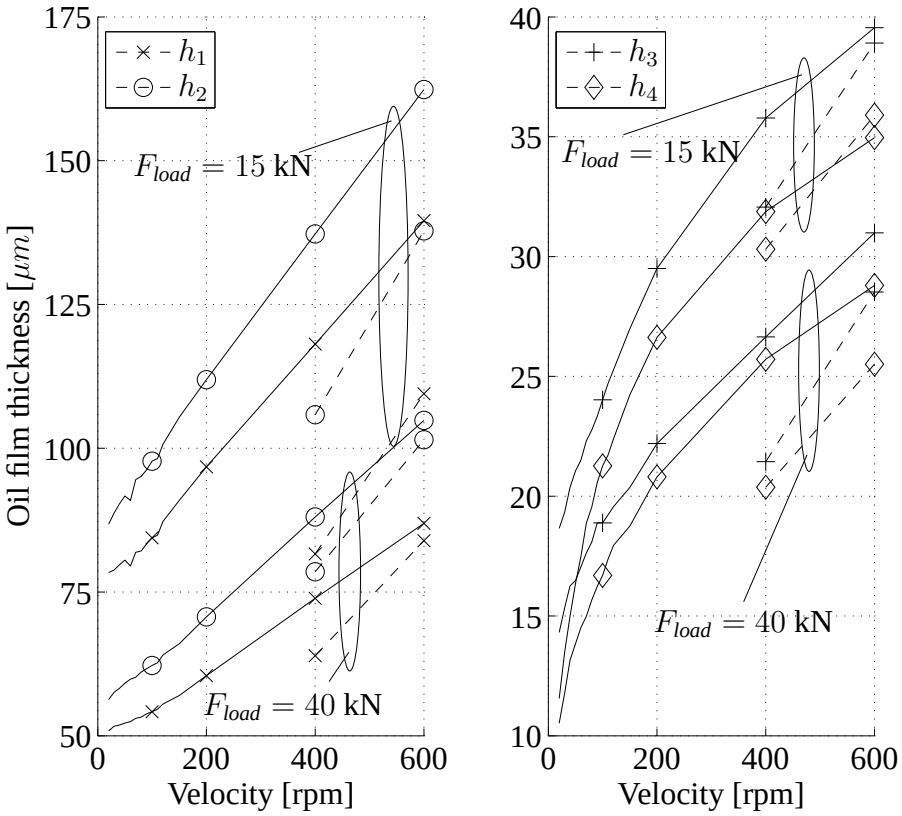

Figure 4.14: Comparison of measured oil film thicknesses with (full lines) and without (dashed lines) 400 cm^3/min oil injection. Left: Leading edge film thicknesses. Right: Trailing edge values.

4.4.4 Thermal bending

The bending of the pad due to thermal gradients is measured using a strain gauge arrangement as seen in figure 4.16(top). 350 Ω, 6 mm gauges with gauge factor $k = 2.06$ are used. They are compensated for the smallest available linear thermal expansion coefficient which has a value of $\alpha = 0.5 \cdot 10^{-6}$ K^{-1}, approximately 4.5 % of the value for steel. The influence of temperature on the measured strain is thereby minimized. The strain-gauges are arranged in two half bridges for respectively the inner radius and the trailing edge. The theoretical values of strain in the positions of the strain-gauges are calculated using Taylor expansions of the deflections as described in figure 4.16(bottom).

In figure 4.17 experimentally and theoretically determined values of strain in the positions of the strain-gauges are shown for two different speeds and loads varying from 15 kN to 65 kN. It is seen that the calculated strains obtained with a corrected pivot point are within a 20 % difference from the experimental values. The average deviation from the experimental values is 7 % . These results indicate that the flat plate approximation used for the calculation of the bending of the pad yields results which are within a reasonable accuracy of the actual behaviour.

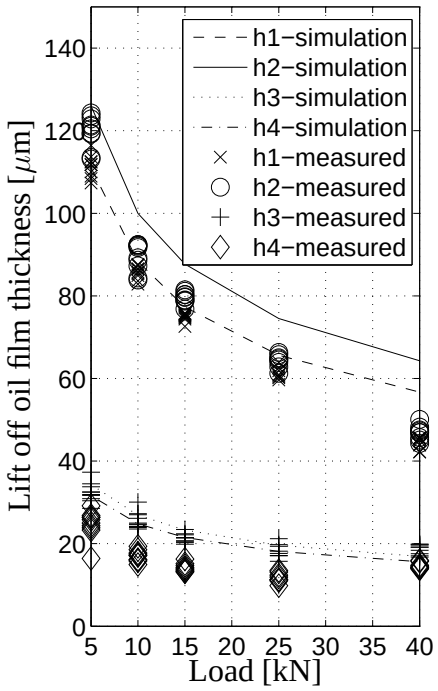

Figure 4.15: Lift off oil film thickness.

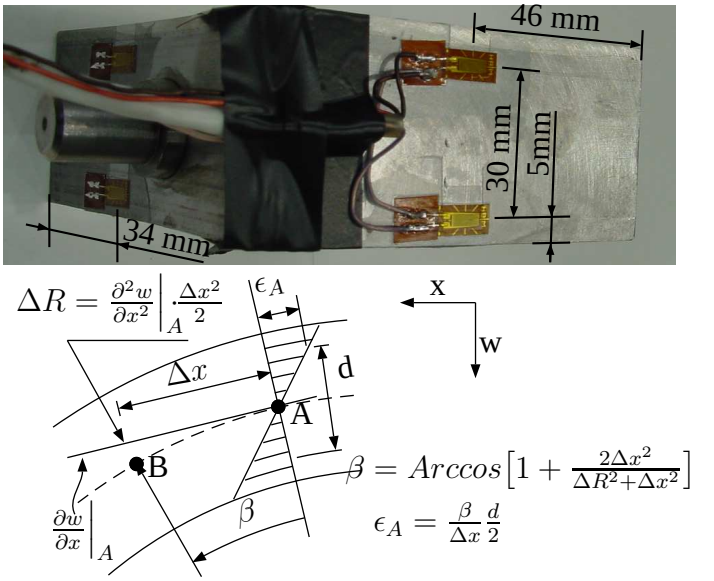

Figure 4.16: Top: Picture showing the position of the strain gauges mounted at the inner radius and trailing edge. Bottom: Drawing showing the calculation of the strain in the position of the strain-gauges from the second derivative of the simulated values of pad deflection w.

The influence of thermal bending on the oil film thickness as well as the pressure and temperature distributions for a pad operating at 15 kN, 400 rpm can be seen in figure 4.13 showing simulation values. The figure shows results for a pad with an injection pocket in order to show the influence of the pocket on the pressure and temperature distributions. The values of deflection for pads with and without injection pockets deviate little.

4.5 Conclusion

Oil film thickness and pressure profiles have been measured for two different thrust bearing pads of approximately 100 cm^2 surface area. One is a plain bearing which is measured for reference. The other is a pad with a leading edge taper and a high pressure injection pocket which is measured with and without constant volume flow high pressure oil injection. The pads operate at loads of approximately 1.5 and 4.0 MPa and velocities of up to 33 m/s. The measurements have been performed in order to study the influence of injection pockets on key bearing parameters and to validate a numerical model.

Simulations and measurements of oil film thickness agree well at low loads. As the load is increased discrepancies become larger at the trailing edge. This is due to a measuring error which is proportional to the difference between the oil bath and pad temperatures. For the plain pad operating at 15 kN, 400 rpm the calculated values are 2 μm or 6 % lower than the measurements. At 40 kN,

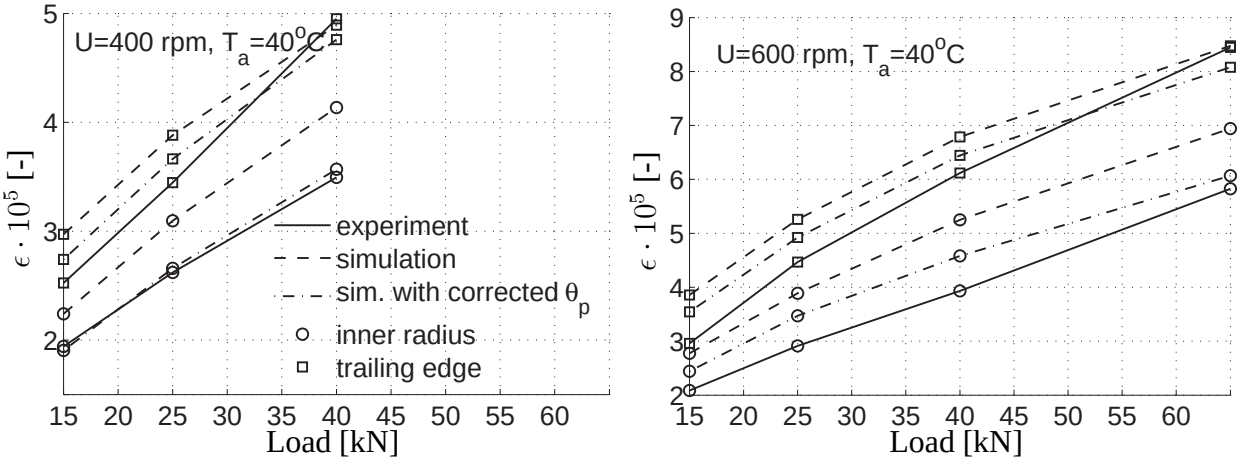

Figure 4.17: Comparison between measured and theoretically determined values of strain.

1000 rpm the calculated values are 9 μm or 25 % lower than the measurements. The results when oil is injected at high pressure show that the start-up oil film thickness depends strongly on the pivot location. The start-up behaviour is predicted well by the model.

The pressure measurements indicate that there is a moment in the circumferential direction at the nominal position of the pivot point. As no external forces are found it seems that the pivot point is shifted towards the trailing edge compared to the nominal position. This is likely to be due to construction tolerances. When the pivot point used in the numerical model is shifted $0.6 - 3.4$ mm ($0.5 - 3.1$ % of the pad length) in the direction of the trailing edge the theoretical pressure profiles for both pads correspond well to those experimentally obtained for low loads. The influence of the pocket is slightly under predicted at low loads, i.e. the calculations predict a slightly higher pressure rise over the pocket than documented by the experiments. At high loads the theoretical pressure profiles correspond less accurately as the experiments document a strong pressure rise after the pocket, which is not predicted by the model. It is assessed that these discrepancies are due mainly to geometric inaccuracies of the collar surface although they may to some extend be due to the simplifications employed in a Reynolds equation description of the pocket flow.

Using a strain-gauge arrangement the deflection of the bearing pad due to pressure bending and thermal gradients has been measured at various operating conditions. An average deviation of 7 % between the measured values of strain at the inner radius and at the trailing edge and the values theoretically determined from the model is recorded. It is concluded that the model determines the bending of the pads to a reasonable level of accuracy.

Chapter 5

Analysis of Standard Tilting-Pad Thrust Bearings

In this chapter bearings of conventional design with and without oil injection pockets at the pivot point are studied. An investigation of the influence of various parameters on the friction loss, the load carrying capacity and the optimal position of the pivot point is performed. The influences of pockets, of pad bending and of the pad length-to-width ratio is analysed. The 3-dimensional TEHD model is used.

Calculations have shown that a good performance, i.e. close to the minimum friction loss for a given minimum oil film thickness is achieved when the bearing pads tilt so that the minimum oil film thickness is located at the centre of the trailing edge. This is generally not the case in a tilting-pad thrust bearing with the pivot located at the mean radius. In a bearing in which the thermal crowning of the pads is insignificant the minimum oil film thickness may be located at the inner or outer trailing edge corner depending on the geometry of the pads. A Michell type bearing with a line pivot can be constructed with the pivot aligned with the trailing edge to fulfill the criterion of minimum film thickness at the mean radius. This corresponds to moving the pivot in the radial direction in bearings with spherical pivots. In order to generalize the results and study the improvement on the friction loss, calculations in which the pivot position is radially adjusted to achieve a minimum oil film thickness at the centre of the trailing edge are performed as well as calculations with the pivot positioned at the mean radius. Although some boundary conditions do not in this case correspond to those employed in the analysis of a Michell type bearing the differences are small and the predicted performance in effect corresponds to the performance of a Michell type bearing with the pivot aligned with the trailing edge.

5.1 Influences of Oil Injection Pockets and Thermal Bending

Bearing pads both with and without cylindrical oil injection pockets are investigated. Pads with two different pocket sizes are studied. The diameters of the pockets are chosen to span the sizes normally used for hydrostatic jacking. The influence of the pivot position on the load carrying capacity and friction loss is investigated. Furthermore, the influence of pad bending is analysed.

Calculations are performed on an 8-pad example bearing with a pad length-to-width ratio of

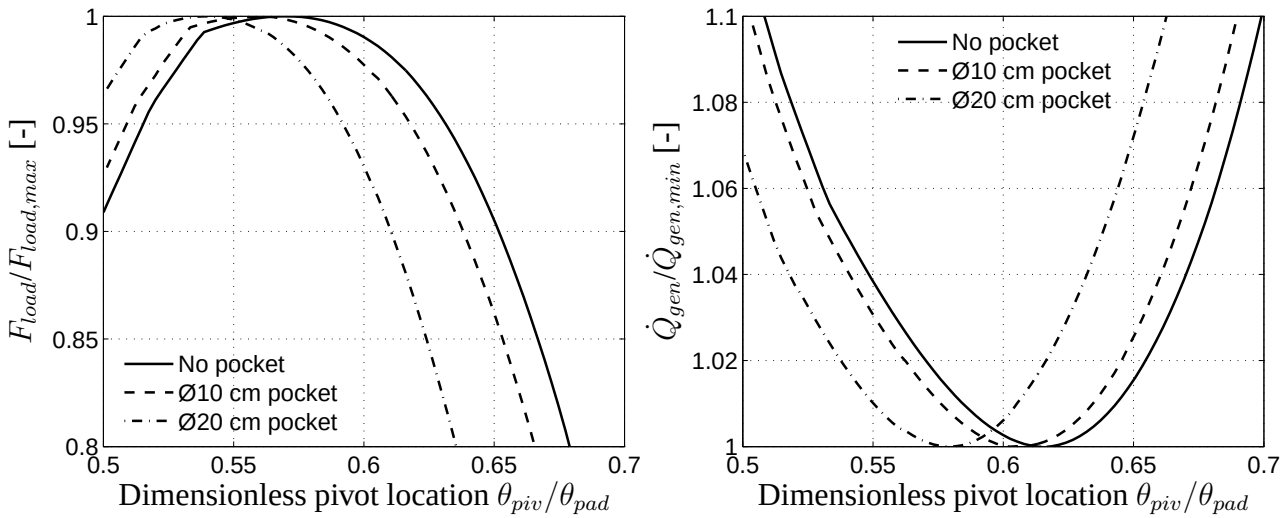

Figure 5.1: The influence of oil injection pockets. Left: Load carrying capacity at different pivot locations. Right: Power loss at different pivot locations. The results are nondimensionalized to give values of 1 in the optimum points.

0.9. The bearing operates using a VG32 mineral oil under fully flooded conditions. A cylindrical pocket with diameter d_p and depth h_p centred at the pivot point allows for hydrostatic lift-off. Data for the bearing and oil are: $\theta_0 = 37.5°$, $r_1 = 0.509$ m, $r_2 = 1.091$ m, $r_{piv} = 0.800$ m, $h_p = 2.0$ mm, $\mu_{40^oC} = 27.1$ mPas, $\mu_{80^oC} = 6.8$ mPas, $\rho = 848$ kg/m^3, $c = 2090$ J/kg/K, $k = 0.13$ W/m/K, $F_z = 5.00$ MN, $\omega = 400$ rpm, $T_a = 40$°C, $T_c = 55$°C. A variable sized grid with $n_r \times n_\theta \times (n_z + n_{z_{pad}})$=24×24×(10+10) control volumes is used in the calculations. The average density of the volumes in the area of the pocket is 1.5 times higher than in the oil film. Bearing pads with pockets of $d_p = 100$ mm and $d_p = 200$ mm and plain bearing pads (without pockets) are studied. Two different grids designated grid$_1$ and grid$_2$ are used for respectively the bearing with the small pocket and the bearing with the large pocket.

Using the procedures explained in chapter 2.4 the effect of varying the dimensionless pivot location $\bar{\theta}_{piv} = \theta_{piv}/\theta_{pad}$ on the load carrying capacity and on the power loss is studied. A minimum oil film thickness of 75 μm is the criteria used in the calculations. Thus, for the study of load carrying capacity the load is adjusted to comply with this criterion. For the study of power loss the load is kept at 5 MN while the pad surface area is adjusted to comply with the criterion. A fixed length-to-width ratio is maintained.

Curves showing the nondimensional load carrying capacity and friction loss as functions of the pivot position are given in figure 5.1. The optimal pivot locations with respect to both maximum load carrying capacity and minimum power loss move towards the leading edge with increasing pocket size. Introducing a pocket in a bearing pad increases the pitch angle due to the change in pressure pattern. To compensate for this effect the pivot location should be moved towards the centre of the pad. In figure 5.1(left) the optimal load carrying capacity is seen to be achieved at $\bar{\theta}_{piv,opt} = 0.57$ when a plain pad is analysed. $\bar{\theta}_{piv,opt} = 0.54$ with a pocket diameter of 200 mm. In figure 5.1(right) the effect of pockets on the optimal position of the pivot point is seen to be larger

as it moves from $\bar{\theta}_{piv,opt} = 0.62$ for a pad without a pocket to $\bar{\theta}_{piv,opt} = 0.58$ when a pocket of d_p =200 mm is machined at the pivot point. However, the optimum is relatively flat. If designing a bearing without taking the pocket into account and positioning the pivot at $\bar{\theta}_{piv} = 0.62$ the bearing with the Ø100 mm pocket will have a friction coefficient 0.2 % higher than the optimal while the coefficient for the pad with the Ø200 mm pocket will be approx. 2 % higher than the optimal value. This indicates that standard design charts for bearings without oil injection pockets can be used in the design process while still maintaining a near optimal design.

Figure 5.2 shows the oil film thickness, pad deflection, pressure and pad surface temperature for the three different pads with the pivot location optimized for minimizing the power loss. The tilting angle decreases with the pocket size. The effect is however relatively small. The pressure distributions in the pocket areas are almost constant. The mixing in the pockets of the hot oil at the pad surfaces with the colder oil at the collar surface results in cooling of the pads downstream of the pockets. The effect only influences the pads directly downstream of the pockets and as the hot spot is usually located at a larger radius close to the trailing edge it is not significantly lowered by the mixing in the pocket.

The effect of thermal deflection of the pads is studied. The crowning of a pad can be controlled in different ways: changing the pad thickness, multi layer constructions, changing the backing material etc. Here, it is chosen to study the effect of varying the pad deflection without considering the method of achieving such a variation. The deflection fraction described in chapter 2.4 and figure 2.5 is used to control the amount of crowning. A deflection fraction of 1 corresponds to the nominal conditions with the deflection distribution shown in figure 5.2(bottom row).

Figure 5.3 shows the nondimensional load carrying capacity and friction loss for the plain pad at four different deflection fractions: 0, 0.2, 0.5 and 1, indicating ratios from no deflection to the nominal crowning with a pad thickness of 0.3 m. The optima are much more clearly defined when the pads are considered rigid than when thermal crowning is included. This indicates that positioning the pivot correctly in the circumferential direction is more important in bearings with insignificant thermal bending than in the typically larger bearings where the oil film distribution is strongly influenced by thermal bending. The optimal position of the pivot point with respect to the load carrying capacity is strongly influenced by the bending. Without bending $\bar{\theta}_{piv,opt} = 0.62$ while it is $\bar{\theta}_{piv,opt} = 0.57$ at the nominal conditions. The values of $\bar{\theta}_{piv}$ minimizing the friction loss is less influenced by the crowning. $\bar{\theta}_{piv,opt} = 0.63$ without deflection, while it is approx. $\bar{\theta}_{piv,opt} = 0.62$ at the other conditions. Designing the pivot location of a bearing without considering thermal deflection therefore only results in a minor increase in the friction loss for this bearing geometry. At $\bar{\theta}_{piv} = 0.63$ the friction loss with the nominal deflection is 0.25 % higher than the minimum value. It should be noted that the influence of the deflection fraction on the optimal pivot location depends on the bearing geometry. Calculations with a 6-pad bearing with length-to-width ratios of 1.2 show a stronger variation with the deflection. With respect to minimizing the friction loss $\bar{\theta}_{piv,opt} = 0.65$ without thermal crowning while it is $\bar{\theta}_{piv,opt} = 0.615$ when pad bending is included.

In the following the deflection fraction is varied between zero and one so that only a fraction of the deflections shown in figure 5.2 are used in the calculations. The optimal pivot location and the corresponding minimum power consumption are seen in figure 5.4(a). In figure 5.4(b) the radial pivot location is adjusted so that the minimum oil film thickness is located at the mean radius at the trailing edge. As is also seen in figure 5.3(right), figure 5.4(a-right) shows that with increased bending of the pad the optimal position of the pivot moves towards the leading edge of the pad. The

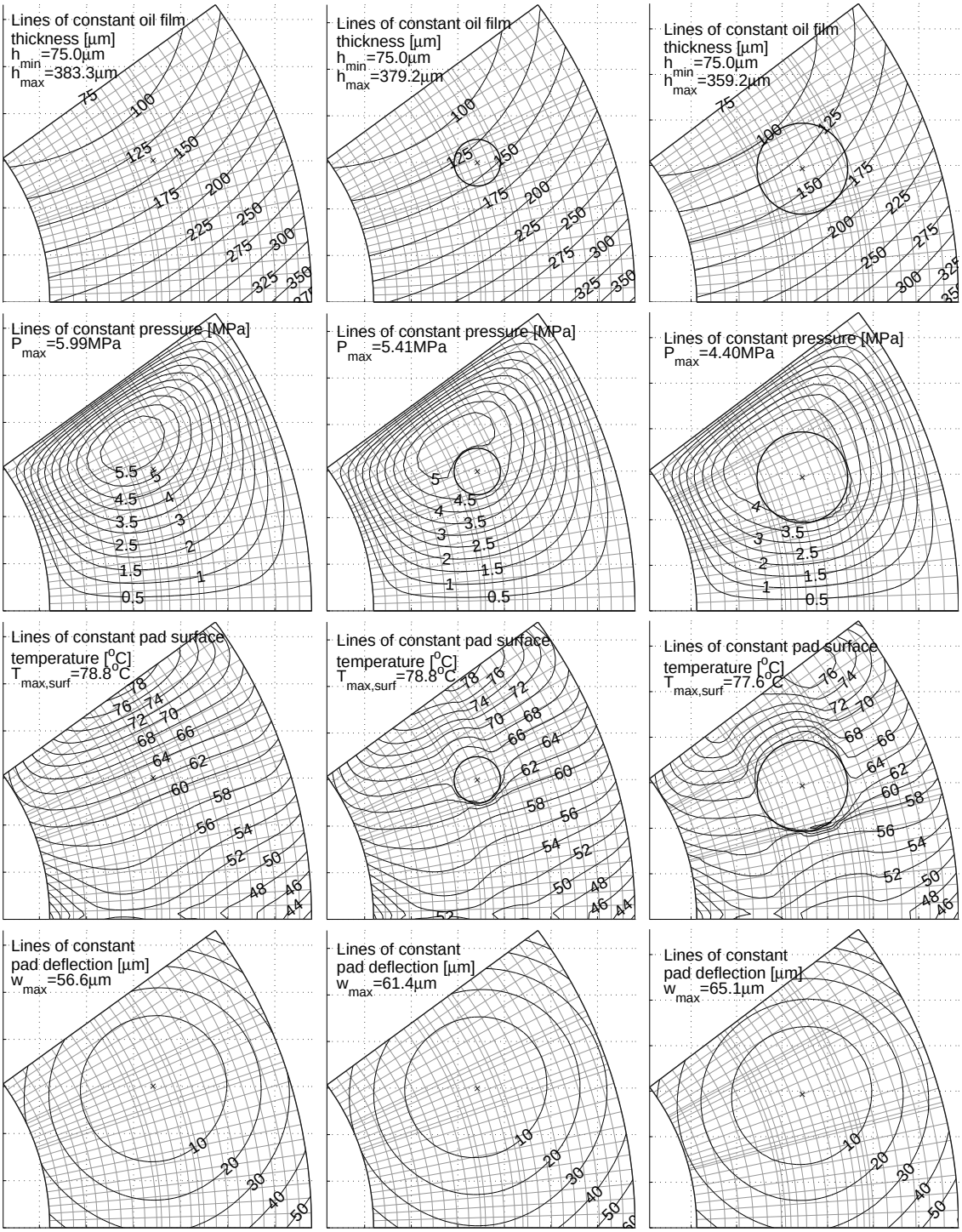

Figure 5.2: From left to right: Simulation results without a pocket, with a Ø100 mm pocket and with a Ø200 mm pocket. The simulations are performed with the pivot location minimizing the power loss. From top to bottom the figures show: oil film thickness, pressure, pad surface temperature and pad deflection.

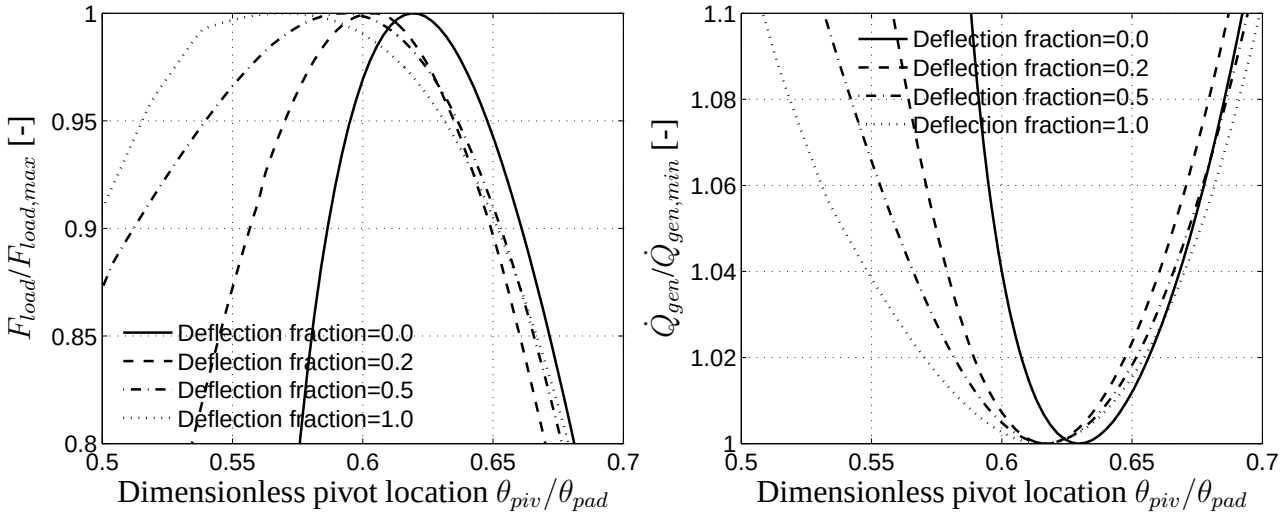

Figure 5.3: The influence of thermal bending (Pad without injection pocket). Left: Load carrying capacity at different pivot locations. Right: Power loss at different pivot locations. The results are nondimensionalized to give values of 1 in the optimum points.

optimal value of deflection is seen to be approximately 40 % of the nominal value. With this amount of bending the friction loss is 5 % lower than the loss when the pad is flat. The example bearing is of a large size. In such bearings the deflection has a large influence on the oil film thickness. In smaller mass-produced bearings the influence of deflection is smaller and sometimes negligible. It is however seen that an amount of bearing deflection or pad curvature is preferable to a flat surface. The reason is that curvature in the radial direction results in a better oil film thickness distribution in which the minimum value is located somewhere around the centre of the trailing edge and not in either of the two trailing edge corners as is the case of a flat pad. The bearing with Ø200 mm pockets produces a larger friction loss than the plain pad. The bearing with Ø100 mm pockets produces a smaller friction loss than the plain pad - at least for a range of deflection fractions. The results indicates that introducing pockets in a bearing pad could lower the friction loss. The results of figure 5.4(b-left) show that when the radial tilt of the bearing is controlled a flat pad not subjected to any curvature is preferable as it produces the smallest friction loss. The figure also shows that both pads with oil injection pockets have smaller friction coefficients than the pad without a pocket. With an Ø200 mm pocket the reduction in friction is up to 2.5 % relative to the plain pad. Figure 5.4(b-right) presents the corresponding pivot locations in the circumferential direction. These would be the optimal positions of the pivots if designing with line-pivots.

5.2 The Influence of the Length-to-Width Ratio

The length-to-width ratio of the individual pads influences the performance of the bearing due to the differences in the convergence of the oil film. In the following the influence of the length-to-width ratio is examined. Tilting-pad thrust bearings with 4, 5, 6, 8 and 12 pads are studied. The mean

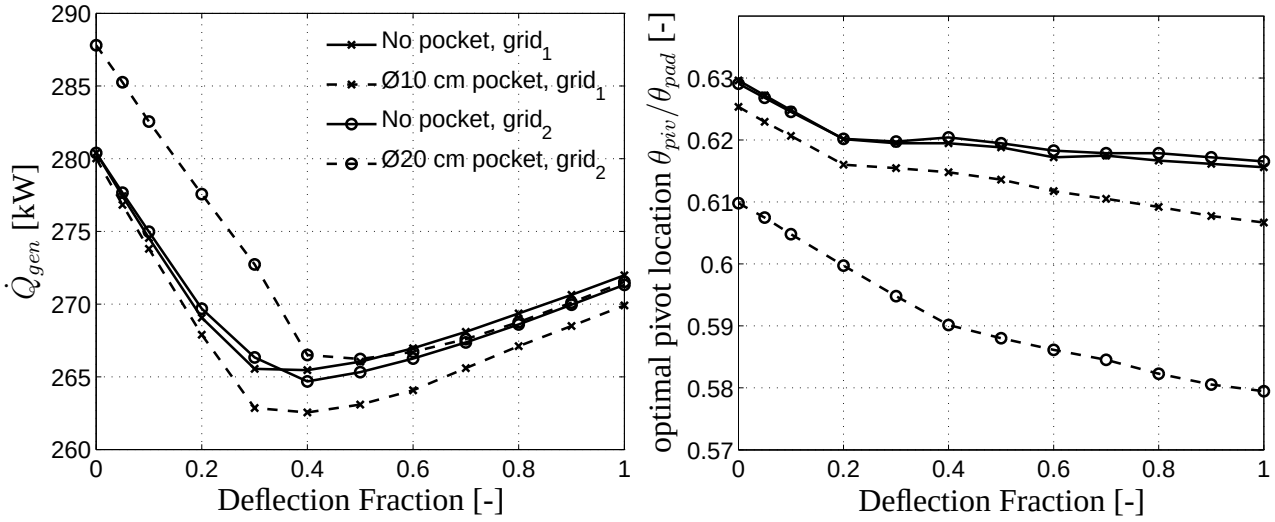

(a) Calculations with r_{piv}=0.80 m

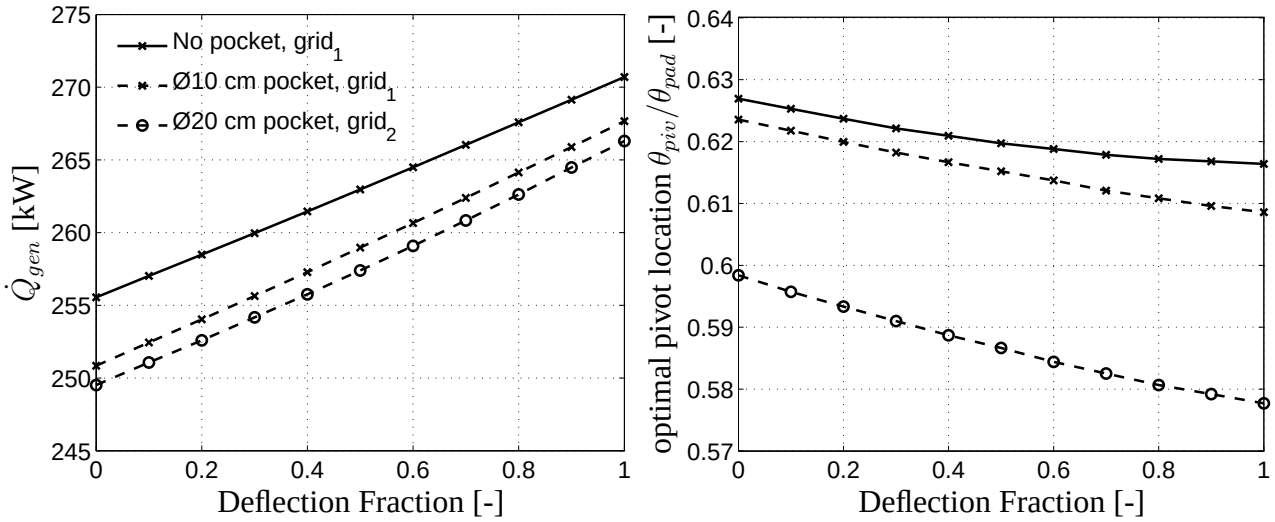

(b) r_{piv} is adjusted so that h_{min} is positioned at the centre of the trailing edge.

Figure 5.4: Left: Minimum obtainable power consumption with different pocket sizes and different values of pad deflection. Right: The corresponding optimal pivot locations.

radius is 0.8 m. The width of the bearings vary from 0.55 m to 0.65 depending on the number of pads and the angular extend of all the pads. All pads have a thickness of 0.3 m.

In figure 5.5 power losses, optimal angular pivot positions and optimal radial pivot positions are shown. For rigid pads with the pivot positioned at the mean radius the optimal length-to width ratio is 1.2. This corresponds to a 6-pad bearing. The reason for this can be seen in 5.5(right) showing the radial position of the pivot point which leads to a minimum oil film thickness at the centre of the trailing edge. The usual praxis of positioning the pivot at the mean radius fulfills the criteria of a minimum oil film thickness at the centre of the trailing edge at a length-to-width ratio of approx. 1.2. At lower length-to-width ratios positioning the pivot at the mean radius leads to a minimum

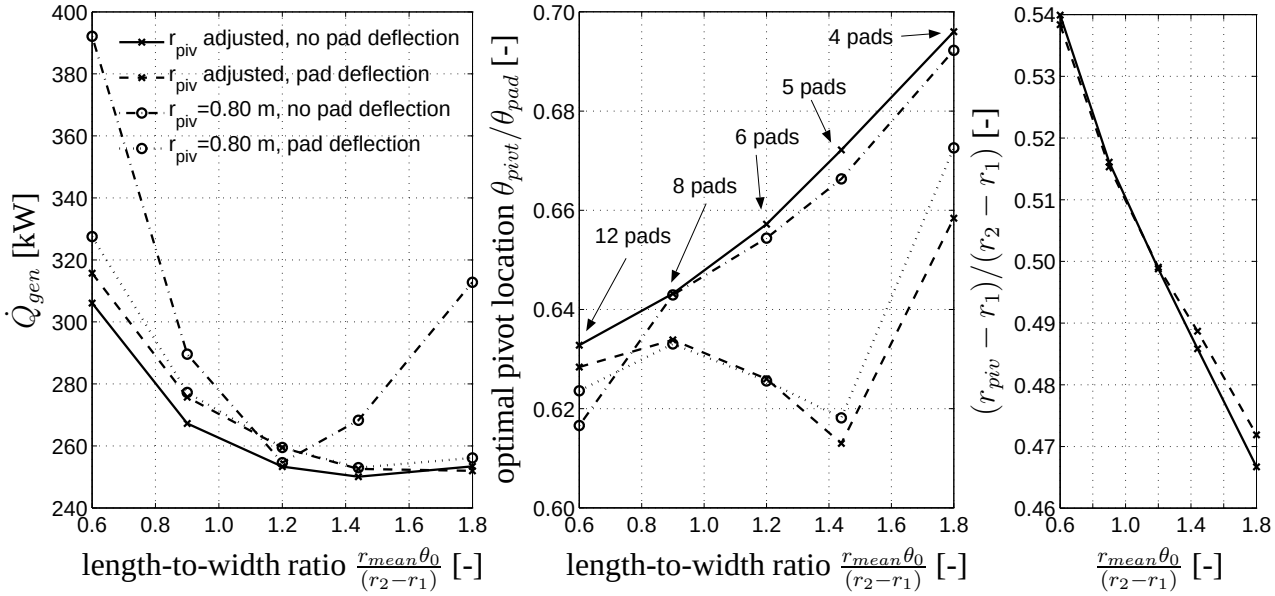

Figure 5.5: The influence of length-to-width ratio. Left: Minimum power loss. centre: The corresponding angular pivot locations. Right: Radial position of pivot point, when the oil film thickness is aligned with the trailing edge.

oil film thickness at the inner trailing edge corner while at high length-to-width ratios the minimum oil film thickness is located at the outer trailing edge corner. Pads, which experience strong thermal crowning have higher optimal length-to-width ratios (approx. $1.4-1.8$). This is also the case for bearings in which there is no radial tilting at the trailing edge. Figure 5.5(middle) shows the optimal circumferential pivot location. The optimal pivot location first rises with the length-to-width ratio from a ratio of 0.6 to 0.8 then falls from a ratio of 0.8 to 1.4. From a ratio of 1.4 to 1.8 it rises sharply. The thermal bending of the pad increases with the pad length-to-thickness ratio and to achieve an advantageous pressure distribution the nondimensional pivot location moves towards the centre of the pad for higher length-to-width ratios. At a ratio of 1.8 this leads to cavitation at the trailing edge. That is disadvantageous for the power loss because the friction loss in the regions with cavitation is large while there is no contribution to the pressure build-up. The optimal position of the pivot is therefore closer to the trailing edge leading to a higher tilting angle and no cavitation.

The optimal length-to-width ratio depends on the curvature of the pads. In the results discussed in the previous paragraph the bearing outer radius is approximately twice the inner radius. This is a typical value for mass-produced bearings. The ratio of outer to inner radius is rarely much larger than 2. It is however not unusual to use bearings in which this ratio is much smaller than 2. A ratio of 1 corresponds to a rectangular pad. Such bearings commonly use 16 or more pads of much lower circumferential curvature. In order to illustrate the variation in the optimal length-to-width ratio depending on the pad curvature a rectangular pad is studied. The rotor temperature is 55 °C, the oil bath temperature is 40 °C and the leading edge temperature is set equal to the rotor temperature. The speed is 30 m/s and one pad carries a load of 1.0 MN. The pads are 0.3 m thick. Pads with length-to-width ratios of 0.2 to 2.0 are studied.

Figure 5.6(left) shows that length-to-width ratios of $0.8-1.0$ result in small friction losses. Fig-

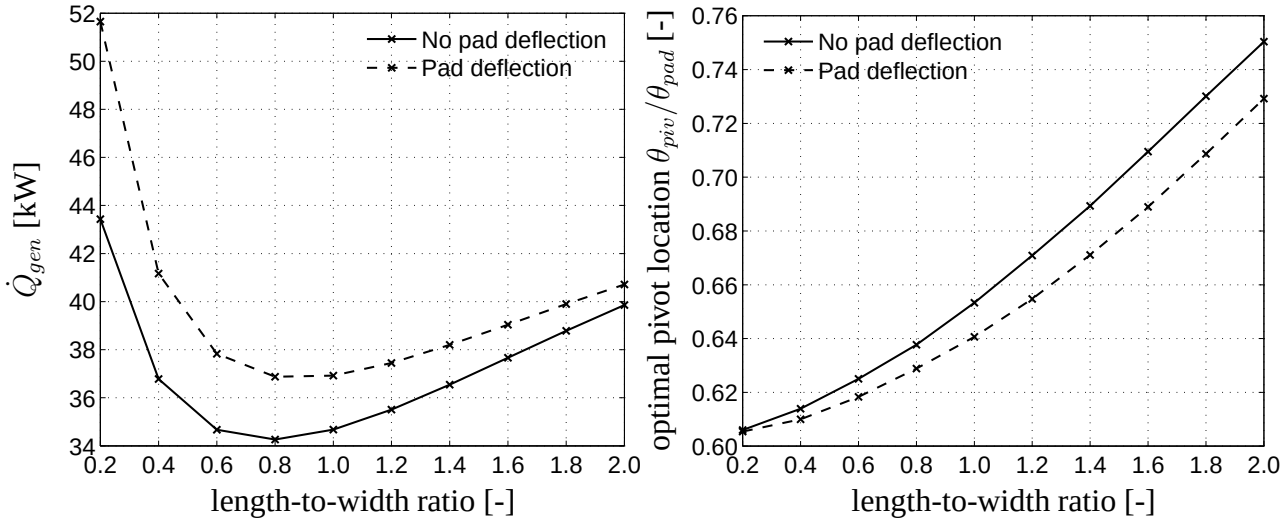

Figure 5.6: Left: Minimum power loss at different length-to-width ratios of a square bearing pad. Right: The corresponding pivot locations.

ure 5.6(right) shows optimal nondimensional pivot locations which for flat pads are between 0.01 smaller and 0.035 higher than those presented for sector shaped pads in figure 5.5(middle).

Based on the results of figure 5.5 and figure 5.6 it is concluded that the length-to-width ratios of the pads of tilting-pad thrust bearings should be kept within the interval [0.8; 1.8] to minimize friction. The choice of ratio within this interval depends on the curvature of the pads.

5.3 Conclusion

Tilting-pad thrust bearings of standard design with and without oil injection pockets have been studied. The influence of thermal bending, pad length-to-width ratio and pad curvature on the friction loss and the optimal circumferential position of the pivot point has been investigated. Furthermore, the influence of thermal bending on the load carrying capacity has been studied. In addition to studying bearings in which the pivots are radially positioned at the mean radius as is the usual praxis, a comparative study has been made with bearings in which the pivot is located so as to result in zero radial tilting at the trailing edge. This corresponds to the behaviour of a Michell type bearing with the line pivot aligned with the trailing edge.

Oil injection pockets at the pivot point - with the oil injection turned off - cause higher pitch angles than in bearings without pockets due to the changes in the pressure distribution. To compensate for this the pivot point should be moved towards the centre of the pad. Within the range of pocket sizes usually used for high pressure injection this results in optimal pivot locations up to $0.04 \cdot \theta_{pad}$ smaller than the optimal positions in plain bearing pads.

The thermal crowning of the bearing pads influences the optimal position of the pivot point. The larger the thermal crowning, the lower the optimal nondimensional pivot location. The influence is however small for the example bearing and designing without considering the crowning induces

only slightly higher (0.25 %) friction losses. The optimum is flatter when the pads are crowned. Thus, it is more important to correctly position the pivot in bearings where the pad curvature due to thermal bending is small.

Bearings with various length-to-width ratios have been studied. The optimal length-to-width ratio has been shown to be between 0.8 and 1.8. The choice of ratio within this interval depends on the curvature of the pads. The higher the curvature the higher is the optimal length-to-width ratio.

Chapter 6

Analysis of Tilting-Pad Bearings with Shallow Recesses

Parallel-step bearings have smaller friction coefficients than tilting-pad bearings. Several reasons however, disqualify this bearing type for use in many application. The performance of parallel-step bearings strongly depends on the operating conditions, i.e. the bearing must be operated at an oil film thickness close to the design value. This also implies that wear reducing the height of the step reduces the performance significantly.

This chapter analyses the theoretically obtainable performance improvement of parallel-step bearings compared to tilting-pad bearings. The possibility of applying features of the parallel-step bearing to tilting-pad bearings in order to create a double incline tilting-pad bearing with improved performance is investigated. The results of chapter 3.2 indicate that the performance of tilting-pad bearings can also be improved by the use of enclosed shallow recesses. Calculations show this to be a special case of bearings with inlet pockets - but with poorer performance. Enclosed shallow recesses are not investigated further. The results of this chapter are obtained using 1-dimensional and 2-dimensional bulk flow analysis.

6.1 1-Dimensional Double Incline Bearings

In the following a 1-dimensional isothermal analysis of a double incline tilting-pad bearing is performed. A bearing pad with a length of 0.5 m operating at a speed of 30 m/s, a load of 1.0 MN and a temperature of 55 °C is analysed. The width of the bearing is adjusted to achieve a minimum oil film thickness at the trailing edge of 75 μm. The geometry of the bearing is shown in figure 6.1(left). The height and position of the step are: $h_s/h_{te} = 0.98$ and $L_s/L_{pad} = 0.79$. These are the dimensions giving the minimum friction loss at a tilting-angle of zero. At this tilting-angle the bearing behaves as a parallel-step bearing. The values of step height and step position available in the literature (Hamrock et al., 2004) giving the maximum load carrying capacity: $h_s/h_{te} = 0.897$ and $L_s/L_{pad} = 0.718$ result in a friction loss 2.25 % higher than the minimum value. Figure 6.2(left) shows the friction loss of the double incline bearing at different tilting-angles. The results are compared to those for a single incline bearing. The best performance is achieved at a tilting-angle of zero where the power loss is 13.4 % lower than the minimum obtainable loss with the single incline

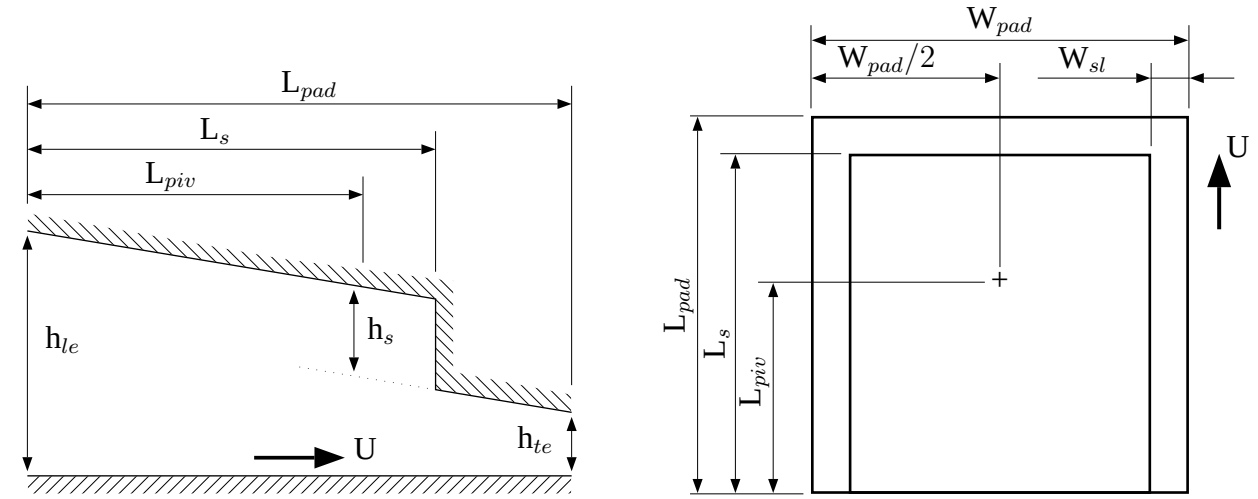

Figure 6.1: Left: The bearing used in the 1-dimensional analysis (side view). Right: The bearing used in the 2-dimensional analysis of rectangular pads (top view).

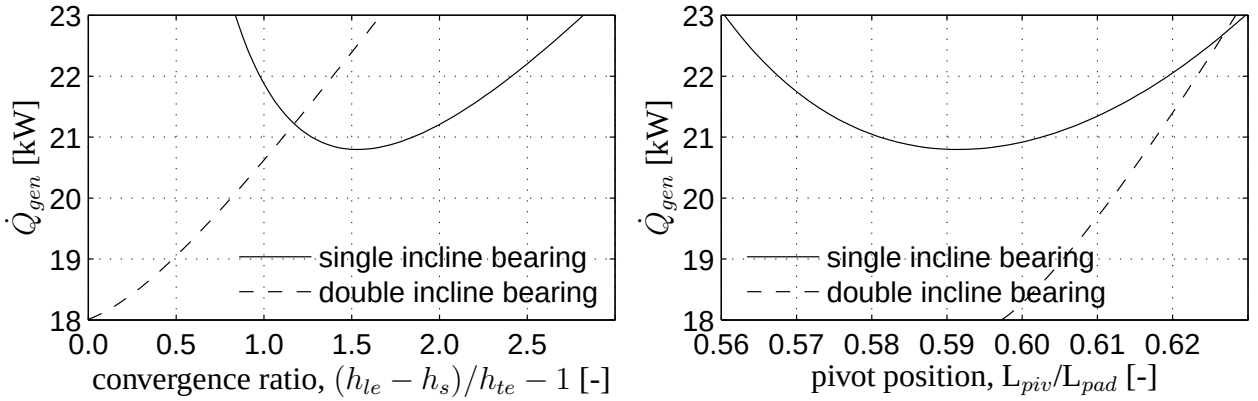

Figure 6.2: 1-dimensional analysis of a bearing with $h_s = 0.98 \cdot h_{te}$ and $L_s = 0.79 \cdot L_{pad}$. Left: Friction loss as a function of the pad convergence ratio. Right: Friction loss as a function of the corresponding nondimensional pivot position L_{piv}/L_{pad}.

bearing. Figure 6.2(right) shows the power loss as a function of the pivot position. The optimal pivot positions for the two bearings are both located at values of L_{piv}/L_{pad} between 0.59 and 0.60. The friction loss of the single incline bearing is relatively insensitive to the pivot position compared to the double incline bearing, in which the power loss rises steeply with the offset from the optimum.

6.2 Rectangular Parallel-Step Bearing Pads

Figure 6.1(right) shows a parallel-step bearing with side lands. The recess is rectangular and has a uniform depth, h_s. Figure 6.3 presents a THD-analysis of the bearing pad for various side land

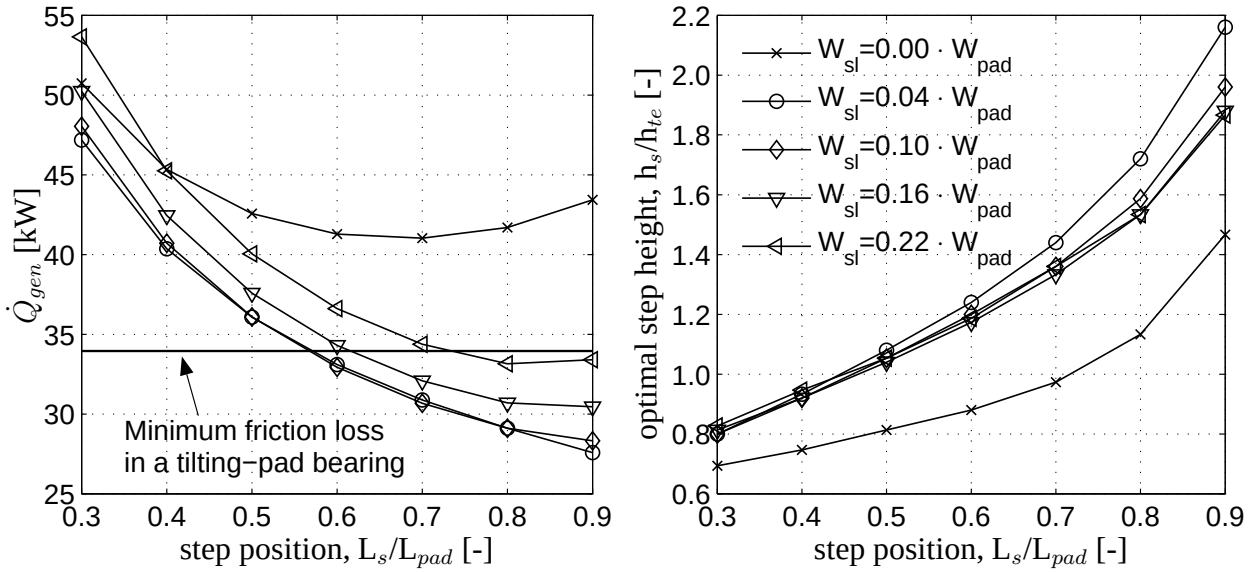

Figure 6.3: 2-dimensional THD-analysis of the design of a parallel-step bearing with side lands. Left: The minimal obtainable friction loss as a function of the step position. Results are stated for various side land widths. Right: The corresponding optimal step height.

widths, W_{sl} and step positions, L_s. The operating conditions are: $U = 30$ m/s, $F_z = 1.0$ MN, $T_a = 40$ °C and $T_c = 55$ °C. The pad area is adjusted to give a minimum oil film thickness of 75 μm. For each combination of W_{sl} and L_s the step height, h_s is optimized to give the minimum friction loss. A grid of 50×50 control volumes is used in the calculations .

In figure 6.3(left) the friction loss is shown. For comparison the minimum obtainable friction loss of a tilting-pad bearing is also presented. Figure 6.3(right) shows the corresponding step heights. For $W_{sl} = 0$, indicating a bearing without side lands, the friction loss is more than 20 % higher than the minimum obtainable friction loss of a tilting-pad bearing. The side leakage in this bearing is high and it does not perform well. When introducing side lands figure 6.3(left) shows that narrow side lands and a step position close to the trailing edge gives a good performance. The maximum step position shown in the figure is 0.9 but calculations show that the theoretically best performance is obtained for $W_{sl} \to 0$ and $L_s \to L_{pad}$. The good performance of a bearing with very narrow side lands and the step positioned very close to the trailing edge is purely theoretical. In practice the side leakage would be large due to the unevenness of the rotor and if mixed lubrication occurs during operation the wear of the bearing surface would be large. More realistic values are $W_{sl}/W_{pad} = 0.1$ and $L_s/L_{pad} = 0.9$. With this geometry and the optimal step height of $1.96 \cdot h_{te}$ a parallel-step bearing has a friction coefficient 17 % lower than that of a tilting-pad bearing. The curves of figure 6.3(right) show that the optimal step height depends strongly on the step position while the variation with the width of the side lands is less significant.

Figure 6.4 presents a study of the sensitivity of a parallel-step bearing to the height of the step. The bearing is of a length-to-width ratio of one, with $W_{sl}/W_{pad} = 0.1$ and $L_s/L_{pad} = 0.9$. The optimal step height for minimizing the friction loss is $1.96 \cdot h_{te} = 147\mu$m. The area is fixed at the

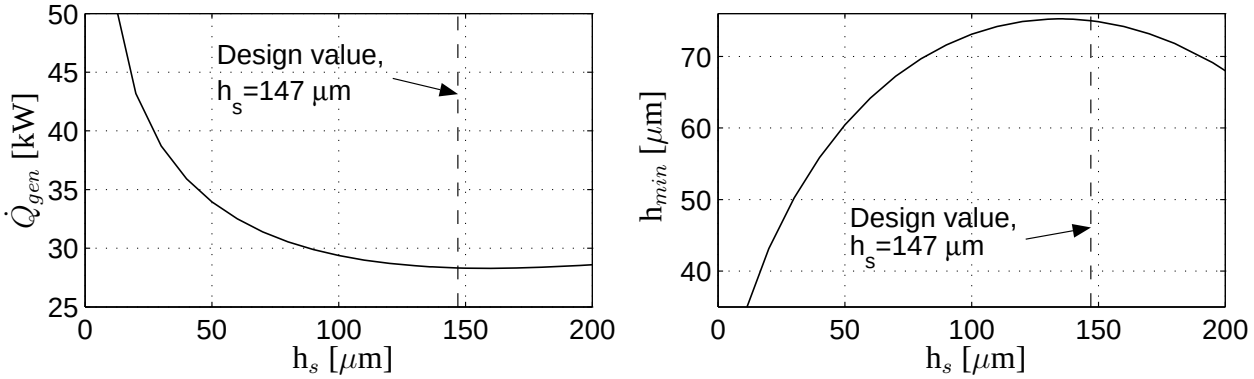

Figure 6.4: THD-analysis if a parallel step bearing with $W_{sl}/W_{pad} = 0.1$ and $L_s/L_{pad} = 0.9$. Left: Friction loss as a function of the step height. Right: Minimum oil film thickness as a function of the step height.

value giving an oil film thickness of 75 μm at this step height. The maximum load carrying capacity is achieved at a step height of 135 μm, 8 % smaller than the design value. The oil film thickness is 75.3 μm. As the maximum load carrying capacity is achieved at a lower step height than the design value, the bearing is relatively insensitive to moderate wear of the step. At a step height of 73.5 μm, 50 % lower than the optimal step height, the oil film thickness is 68.1 μm, 9 % less than the design value. The friction loss is 10 % higher than the value at $h_s = 1.96 \cdot h_{te}$. Further reducing the step height reduces the performance more rapidly.

6.3 Rectangular Double Incline Bearing Pads

This section investigates the possibility of designing a tilting-pad bearing with an inlet pocket. The parallel-step bearing with $W_{sl}/W_{pad} = 0.1$ and $L_s/L_{pad} = 0.9$ is now considered to be equipped with a spherical pivot at the $L_{piv}-$position. To evaluate the influence of thermal effects both isothermal, THD and TEHD models are used in the analysis.

Figure 6.5 shows the generated friction loss at various pivot locations for inlet pocket depths of 20, 60, 100, 140 and 180 μm. In all calculations the area of the pad is adjusted to give a minimum oil film thickness of 75 μm. Figure 6.5(a) presents isothermal results obtained with at a temperature of 55 °C. With the chosen pocket geometry the friction loss curves all have minima in the region $L_{piv}/L_{pad} = 0.64$ to $L_{piv}/L_{pad} = 0.66$. Choosing a value of $L_{piv}/L_{pad} = 0.66$ for the design gives good values of the friction loss at all recess depths. Depending on the pocket depth the friction loss is reduced by up to 12 % in comparison to a bearing with plain pads. This indicates that a tilting-pad bearing can be equipped with inlet pockets to improve the performance while still maintaining the qualities which make the tilting-pad bearing superior to the parallel-step bearing: low sensitivity to variations in the operating conditions and to reduction of the pocket depth due to wear. The reduction in friction is however achieved at the cost of a higher sensitivity to the position of the pivot point. The deeper the pocket the higher the sensitivity as can be seen in the steep rise in friction loss as the pivot point is raised from the value of $L_{piv}/L_{pad} = 0.66$. Reducing the values

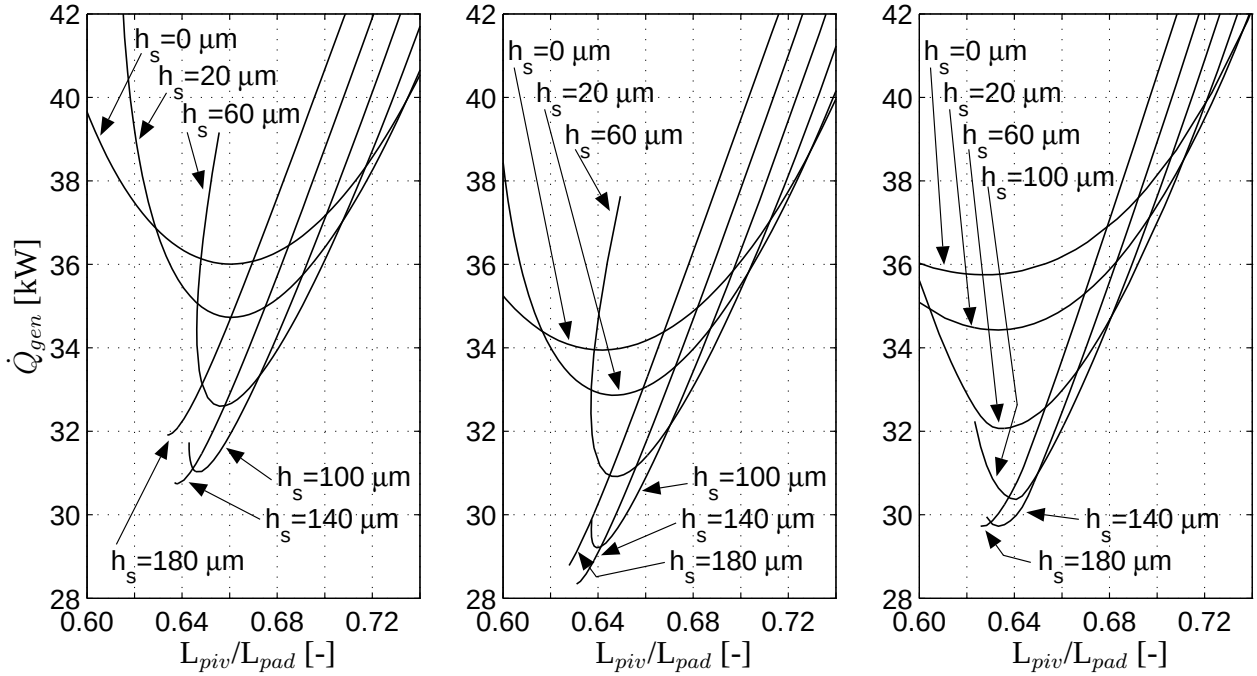

(a) Isothermal analysis (b) THD-analysis (c) TEHD-analysis

Figure 6.5: Friction loss as a function of the pivot location L_{piv}/L_{pad} for inlet pockets of various depth. Figures stating result obtained using isothermal, THD and TEHD models are presented in the three figures.

of L_{piv} to approx. $0.645 \cdot L_{pad}$ the friction curves for $h_s = 60$ μm and $h_s = 100$ μm rise sharply. Below this value of L_{piv} no equilibrium position exists and the bearing does not work. The end of the friction curves indicate the operating conditions for zero tilting angle, i.e. for a parallel-step bearing. E.g. for a pocket depth of 60 μm this operating condition is located at $L_{piv}/L_{pad} = 0.656$ and a friction loss of 39.2 kW. At pivot locations $L_{piv}/L_{pad} > 0.656$ there are two solutions to the equilibrium position of the bearing pad, one at a positive tilting angle as shown in the figure and one at a negative tilting angle. This phenomenon is studied later in this chapter. Positioning the pivot close to the smallest possible value of $L_{piv}/L_{pad} = 0.646$ may result in pad flutter.

Figure 6.5(b) shows the friction losses as calculated using the 2-dimensional THD-model. Compared to the isothermal analysis the curves move to the left, i.e. the minimum friction loss is achieved at pivot locations closer to the centre of the pad. As shown in chapter 3.1 this is due to an increased tilting-angle as a function of the viscosity variation in the sliding direction. For a plain pad the optimum is located at $L_{piv}/L_{pad} = 0.645$ whereas the isothermal analysis predicted an optimum at $L_{piv}/L_{pad} = 0.66$. Although not very well illustrated by this figure the optimal pocket depth predicted by the THD-analysis is larger than in the isothermal analysis. For a parallel-step bearing the optimal pocket depth predicted by the THD-analysis is $1.96 \cdot h_{te} = 147$ μm as shown in figure 6.4. A similar isothermal analysis indicates $h_{s,optimal} = 1.76 \cdot h_{te}$.

Figure 6.5(c) shows the results when pressure bending and thermal crowning of the pad are in-

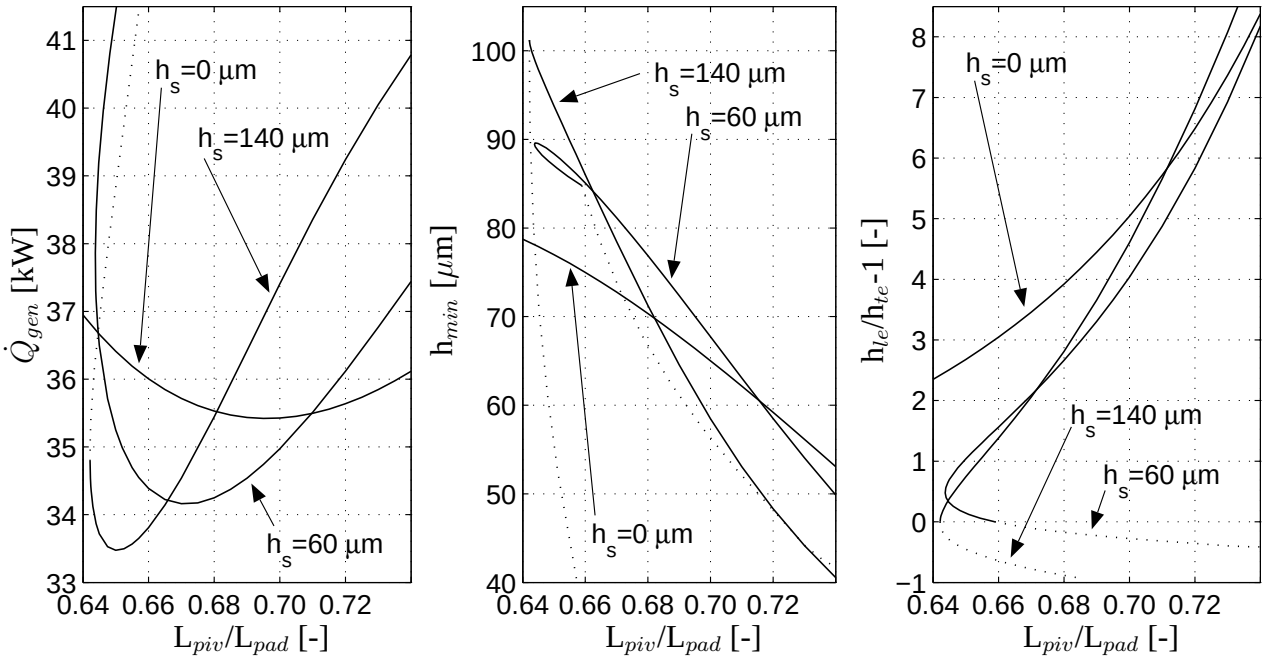

Figure 6.6: Isothermal analysis of a bearing of fixed area without inlet pocket and with pocket with depths of $h_s = 60$ μm and $h_s = 140$ μm. Results are given as functions of the pivot location L_{piv}/L_{pad}. Left: Friction loss. Middle: Minimum oil film thickness. Right: Oil film convergence ratio. Full lines indicate solutions with a positive tilting angle. Dotted lines indicate solutions with a negative tilting angle.

cluded in the analysis. The optimal pivot locations move toward the centre of the pad in comparison to the results for a rigid pad. The optima of the curves are located between $L_{piv}/L_{pad} = 0.62$ and $L_{piv}/L_{pad} = 0.64$. As was also noted in chapter 5 the bearing is less sensitive to the position of the pivot due to the curvature of the pad.

Figure 6.6 shows an isothermal study in which the pad areas of three different pads is kept constant at the value resulting in a minimum oil film thickness of 75 μm at $L_{piv}/L_{pad} = 0.66$ for a bearing without a pocket. As earlier stated for pads with inlet pockets there are two solutions to the pressure distribution which for a given pivot location results in force and moment equilibrium at the pivot point. In the figures both solutions with positive tilting angles(full lines) as well as solutions with negative tilting angles(dotted lines) are presented.

Figure 6.6(left) shows the reduction in friction when modifying the plain bearing with an inlet pocket of $W_{sl}/W_{pad} = 0.1$ and $L_s/L_{pad} = 0.9$ and pocket depths of 60 μm and 140 μm. Introducing an inlet pocket reduces the friction as well as increasing the oil film thickness as shown in figure 6.6(middle). A shallow inlet pocket results in reduced friction and higher minimum film thickness for large ranges of pivot positions. Deeper pockets gives larger improvements in the performance in small intervals of pivot locations. The bearing with the deeper pocket does however not perform well at for instance a pivot location of $L_{piv}/L_{pad} = 0.70$ where the friction loss is higher and the oil film thickness is smaller than those of the plain pad. Figure 6.6(right) shows the convergence

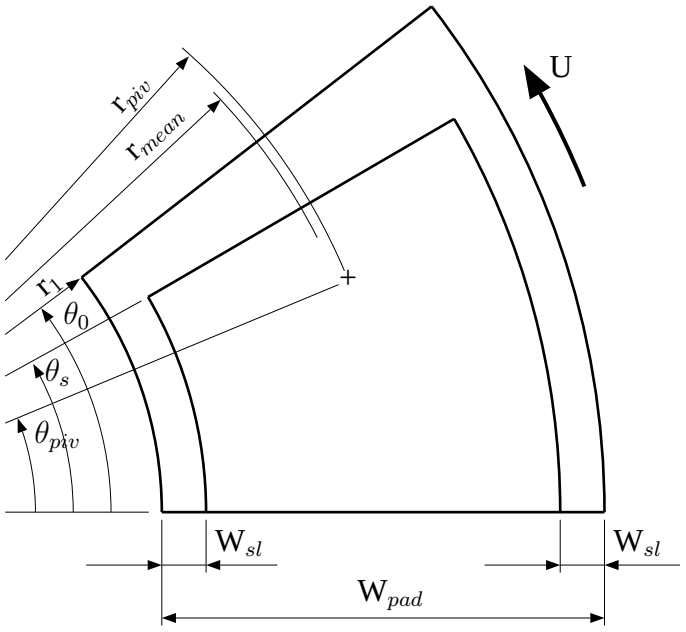

Figure 6.7: The sector shaped bearing pad considered.

ratio of the pads. When introducing inlet pockets of the chosen dimensions the convergence ratio is reduced. At $L_{piv}/L_{pad} = 0.66$ the ratio is 3 for a plain bearing pad while it is approx. 1.5 for the bearing pads with pockets.

The solutions for the pressure distribution obtained with negative tilting angles show much higher friction losses than with positive tilting angles. Only the friction loss for $h_s = 140$ μm can be seen in the figure. It rises sharply with increasingly negative tilting angle. This is due to a rapidly declining minimum oil film thickness.

6.4 Double Incline Tilting-Pad Thrust Bearings

In this section of the report the analysis previously performed on rectangular pads is extended to the study of multi-pad bearings with sector shaped pads.

A tilting-pad thrust bearing with 8 pads of a length-to-width ratio of 0.9 is studied. The mean radius is 0.8 m. The pads have a thickness of 0.3 m. The rotor temperature is 55 °C, the oil bath temperature is 40 °C and the leading edge temperature to each pad is determined from a control volume analysis of heat transfer in the groove between the pads. The speed is 400 rpm and the bearing carries a load of 5.0 MN. The numerical model adjusts the bearing surface area to achieve a minimum oil film thickness of 75 μm. Figure 6.7 illustrates the bearing. In all calculations $W_{sl}/W_{pad} = 0.1$.

In table 6.1 a grid convergence study is shown. A plain bearing and a bearing with a 60 μm inlet pocket with $\theta_s/\theta_0 = 0.8$ are studied. For the plain pad values of friction loss, maximum oil film thickness, maximum oil temperature and pad surface area converge monotonously. For the pad

No. control volumes	25×25	50×50	100×100	200×200
	Plain bearing pad (no pocket)			
$\dot{Q}_{gen}$ [kW]	272.89	274.31	274.72	274.83
h_{max} [μm]	317.13	320.51	321.34	321.51
T_{max} [°C]	61.73	61.54	61.48	61.45
Pad Area [m^2]	1.6283	1.6362	1.6377	1.6378
	Bearing pad with 60 μm recess			
$\dot{Q}_{gen}$ [kW]	254.61	251.89	252.97	253.54
h_{max} [μm]	252.96	250.34	244.98	242.02
T_{max} [°C]	65.07	63.90	64.21	64.41
Pad Area [m^2]	1.4585	1.4307	1.4309	1.4313

Table 6.1: Grid convergence study: $\dot{Q}_{gen}$ is the shear work at the collar surface. h_{max} is the maximum oil film thickness and T_{max} is the maximum temperature in the oil film. In all calculations : $h_{min} = 75.00$ μm.

with an inlet pocket the stated parameters converge monotonously only from a grid size of 50×50 control volumes. With 25×25 control volumes the boundaries of the pocket are not located at the control volume interfaces and this induces differences in the results compared to the larger grids. The results of the plain bearing converge faster for increasing grid size than when a pocket is present in the surfaces of the pads. The friction loss at 50×50 control volumes is in both cases within 1 % and the value of pad area within 0.1 % of the values at 200×200 control volumes. A grid of 50×50 control volumes is used in the calculations which follow.

Figure 6.8 shows the power loss as a function of the pivot position for various pocket depths and step positions. The pivot point is placed at the mean radius. The end of the power loss curves for declining nondimensional pivot locations indicate pad convergence ratios close to zero. Lower pivot locations result in cavitation and a steep rise in the friction loss. The numerical calculations of these cases are generally numerically instable and the solutions are therefore not stated in the figures. The end of the curves (e.g. figure 6.8(b), 100 μm and 140 μm) indicate close to the minimum friction loss with the respective pocket depths. The deviation from the minimum obtainable values of friction loss is estimated to be within 0.5 % in all the calculations.

Figure 6.8(a) shows the friction loss for $\theta_s/\theta_0 = 0.9$, i.e. dimensions of the pocket which are similar to those of the rectangular pad studied in the previous section. The minima of the power loss curves are positioned at higher θ_{piv}/θ_0-values for higher pocket depths. Positioning the pivot at $\theta_{piv}/\theta_0 = 0.61$, which is the optimum location for a pad without a recess will cause a non functioning bearing if inlet pockets are machined in the pad surfaces. Smaller friction losses and lower optimal θ_{piv}/θ_0-values are achieved with $\theta_s/\theta_0 = 0.85$ as shown in figure 6.8(b). The minima of the friction loss curves are located at almost the same nondimensional pivot location (0.61−0.62). Figure 6.8(c) presents results with $\theta_s/\theta_0 = 0.8$. The minima of the power loss curves are positioned at lower θ_{piv}/θ_0-values for higher pocket depths. Small values of friction and stable operating conditions at all values of the pocket depth can be achieved by positioning the pivot at $\theta_{piv}/\theta_0 = 0.61$. At this pivot location the reduction in the friction loss is up to 8 % for the chosen

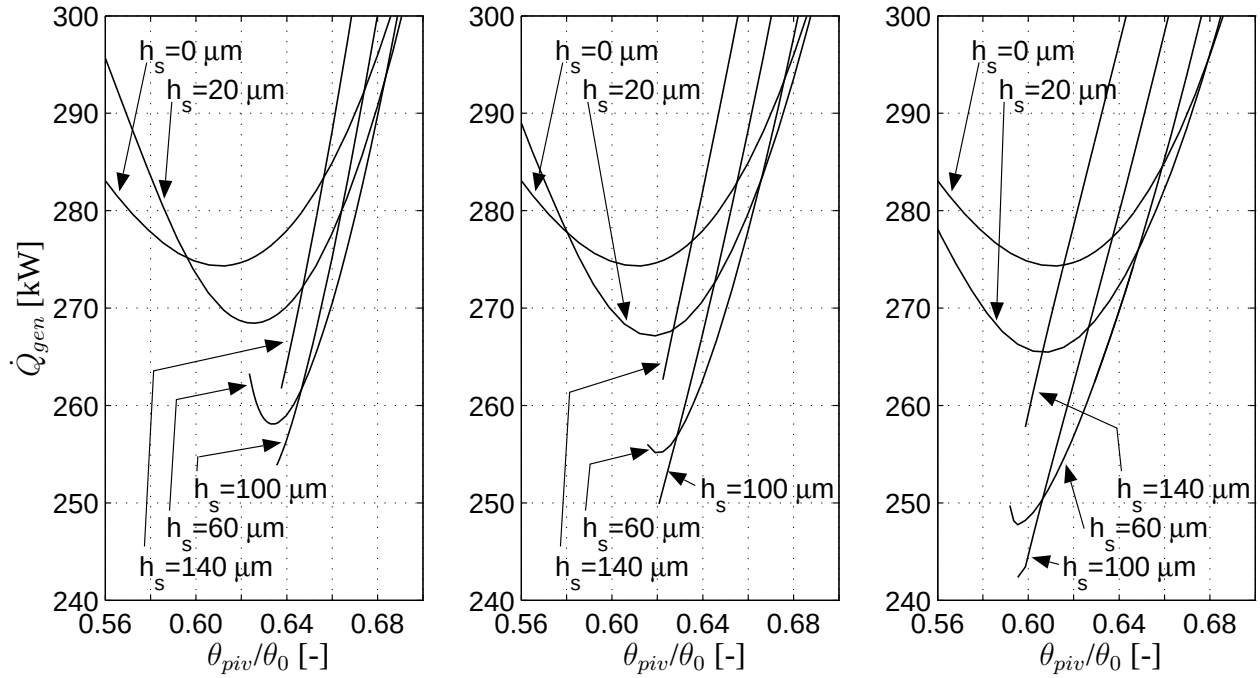

(a) $\theta_s = 0.90 \cdot \theta_0$ (b) $\theta_s = 0.85 \cdot \theta_0$ (c) $\theta_s = 0.80 \cdot \theta_0$

Figure 6.8: Friction loss as a function of the pivot location θ_{piv}/θ_0 for inlet pockets of various depth. The figures state result obtained using TEHD modelling with $\theta_s/\theta_0 = 0.90, 0.85$ and 0.80. $r_{piv} = 0.8$ m

pocket depths, compared to using plain bearing pads.

As discussed in chapter 5 a tilting-pad thrust bearing shows superior performance if the radial positions of the pivot points are adjusted so that the bearing shows no radial tilt at the trailing edges of the pads. Figure 6.9 presents friction loss curves in which this condition is imposed. The achievable friction reduction by the use of inlet pockets is in the region of $16-17$ % for all investigated values of θ_s. The closer the step is to the trailing edge the higher is the pocket depth giving a minimal friction coefficient. This was also the case for the rectangular parallel-step bearings studied in figure 6.3. With $\theta_s/\theta_0 = 0.8$ and a pivot position of $\theta_{piv}/\theta_0 = 0.61$ the bearing operates in the stable region at all pocket depths and the reduction in the friction loss is up to 12 % for the chosen pocket depths, compared to using a plain bearing pad.

Figure 6.10 show the distributions of oil film thickness, pressure and temperature for bearings with $\theta_s/\theta_0 = 0.8$, $\theta_{piv}/\theta_0 = 0.61$ and pocket depths of 60 μm and 140 μm. The minimum oil film thickness in both cases is 75 μm. The bearing with a 140 μm pocket is 17 % larger (1.68 m^2) than the bearing with a 60 μm pocket (1.43 m^2). However, due to the higher mean oil film thickness the friction loss is only 0.7 % higher. The bearing with the deep pocket has a higher convergence ratio and due to the larger area the maximum pressure is lower. The maximum temperatures are not significantly affected by the pockets. In a bearing without pockets it is calculated to be 61.6 °C. With a 140 μm pocket it is 60.4 °C while it is 63.9 °C with a 60 μm pocket.

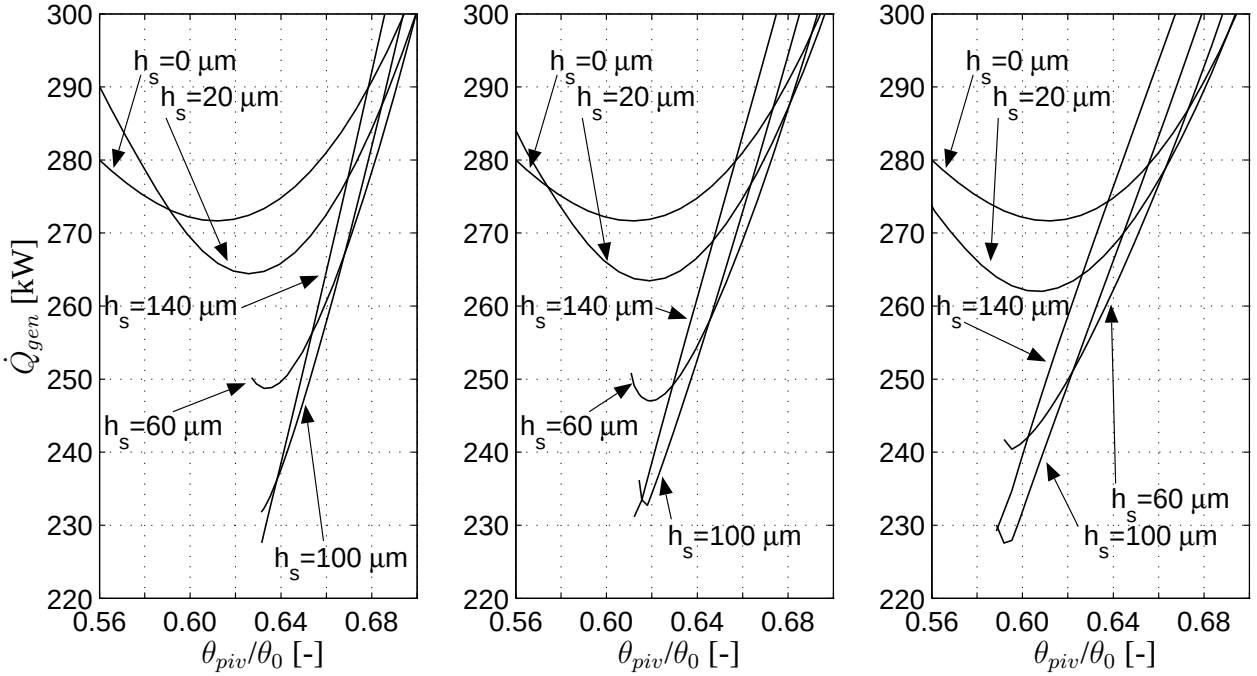

(a) $\theta_s = 0.90 \cdot \theta_0$ (b) $\theta_s = 0.85 \cdot \theta_0$ (c) $\theta_s = 0.80 \cdot \theta_0$

Figure 6.9: Friction loss as a function of the pivot location θ_{piv}/θ_0 for inlet pockets of various depth. The figures state result obtained using TEHD modelling with $\theta_s/\theta_0 = 0.90, 0.85$ and 0.80. r_{piv} is adjusted to achieve zero radial pivoting at the trailing edge.

The friction reductions of figure 6.8 are smaller than those of figure 6.9 because the optimal radial position of the pivot is located at higher offsets from the mean radius when inlet pockets are present in the bearing than when no inlet pockets are present. This is seen in figure 6.11 which presents a study of the behaviour of bearings with pocket depths of $h_s = 0$ μm, $h_s = 60$ μm and $h_s = 140$ μm when the radial position of the pivot is adjusted. The bearing surface area is dimensioned to give a minimum oil film thickness of 75 μm for a plain pad with the pivot located at the mean radius and at $\theta_{piv}/\theta_0 = 0.61$. The radial position of the pivot giving the highest oil film thickness is located further towards the outer radius for higher pocket depths. In the plain pad it is located at the radial nondimensional position: 0.515. With the shallow pocket it is located at 0.525 and with the deep pocket at 0.535. For all the radial pivot positions illustrated in the figure the bearing with the 60 μm-pocket performs better than the plain pad, i. e. the oil film thickness is higher and the friction loss is lower. The 140 μm-pocket has a better performance than both the other bearings in a small interval of radial pivot positions. The bearing however rapidly looses thickness of the oil film as the pivot is moved away from the optimum value. The radial tilting stability of this bearing is lower than in a standard tilting-pad thrust bearing. The radial tilting can be controlled by using different values of W_{sl} at the inner and outer radius.

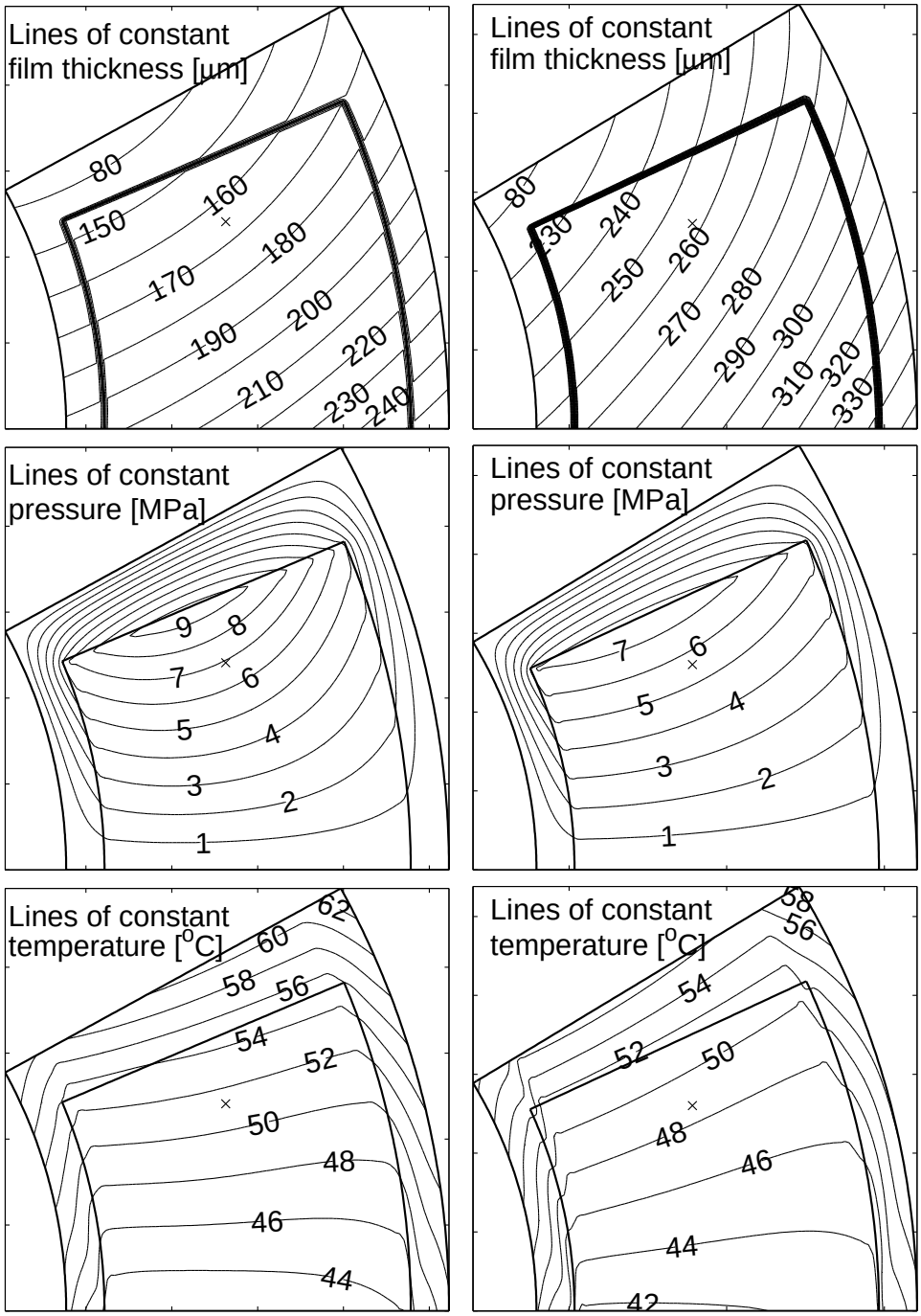

Figure 6.10: Simulation results with a 60 μm (left) and a 140 μm (right) pocket. From top to bottom: oil film thickness, pressure and oil temperature.

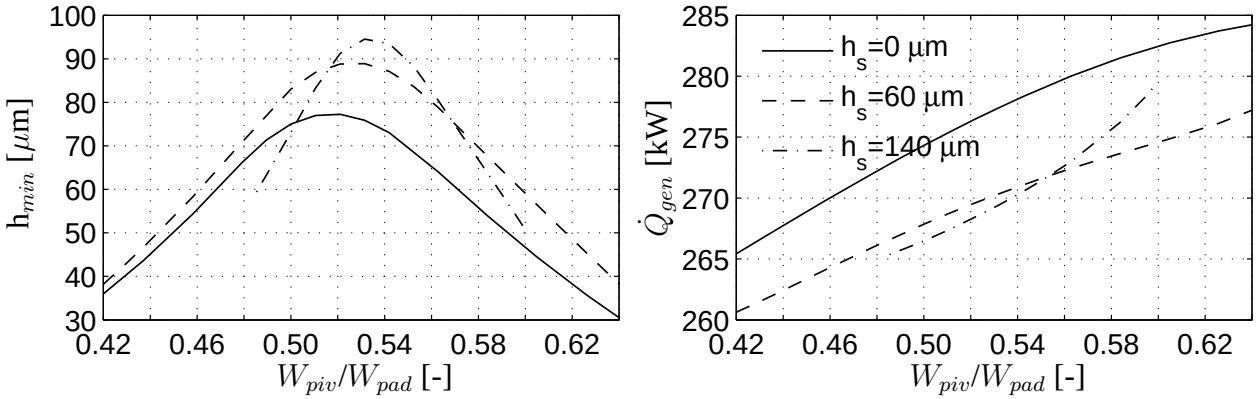

Figure 6.11: Radial stability analysis of bearings of $h_s = 0$ μm, $h_s = 60$ μm and $h_s = 140$ μm. Left: oil film thickness as a function of the radial pivot position. Right: Friction loss as a function of the radial pivot position. Due to failing convergence of the numerical calculations the curves for $h_s = 140$ μm do not cover the full interval of pivot locations.

6.5 Conclusion

Parallel-step bearings theoretically have smaller friction coefficients than tilting-pad bearings. 1- and 2-dimensional studies predict friction coefficients 13-17 % lower than those obtainable in tilting-pad bearings. Parallel-step bearings however suffer from the disadvantage that they do not perform well at varying operating conditions. This also implies that the performance is reduced as the step wears down. This chapter studies the feasibility of combining the two types of bearings in order to benefit from the advantages of both.

Significant performance improvements are possible by designing bearings with inlet pockets or by modifying existing bearings. By combining the features of parallel-step bearings and tilting-pad bearings it is possible to reduce the friction coefficient by 10-15 %. The step can be positioned to give small friction losses and stable operating conditions at all pocket depths from zero up to the design value. Thereby the bearing is tolerant to wear of the pad surfaces.

The reduction in friction is achieved at the cost of a higher sensitivity to correct circumferential positioning of the pivot. The correct position depends strongly on the thermal conditions of the bearing and the amount of thermal crowning of the pads. Positioning the pivot too close to the centre of the pad causes the bearing to entirely loose its load carrying capacity while positioning the pivot too far towards the trailing edge results in a smaller oil film thickness than would be achieved with plain bearing pads. An example thrust bearing has shown an interval of $\theta_{piv}/\theta_0 \epsilon [0.59; 0.66]$ in which the bearing performs superior to a standard bearing. Due to the relatively small interval in which a good performance is achieved and the danger of positioning the pivot in a position in which the bearing will not work the design of bearings based on this principle is not trivial.

Chapter 7

Analysis of Tilting-Pad Bearings with Deep Recesses

The results of chapter 5 showed reductions in the generated friction when oil injection pockets are machined in the surfaces of the pads. The reductions were however small and required relocation of the pivot point.

This chapter further investigates the influence of equipping the surfaces of tilting-pad thrust bearings pads with deep recesses . The 3-dimensional TEHD model is used. In deep recesses (one or more orders of magnitude deeper than the oil film thickness) there is recirculation and no positive effect on the pressure build up. The pressure distribution is therefore scalable with the Sommerfeld number and the design suggestions stated in this chapter of the report are generally applicable at all operating conditions - with the reservation that the influence of thermal effects vary with the operating conditions. Due to the large depth the shear stress at the collar surface is small inside the recess area. Thus, the purpose of the recess is to create a high-pressure and low friction zone.

In the volume of a deep recess, the reductions of the flow equations leading to the Reynolds equation are not strictly valid. In particular, the assumption of inertialess flow seems unreasonable. The recirculation flow accelerates the oil entering the recess causing an inertial pressure drop at the recess leading edge. At the trailing edge of the recess, the oil is stagnated leading to an inertial pressure rise. In tilting-pad bearings with recesses, this may cause a smaller tilting angle than the one predicted by using the Reynolds equation. In conventional bearings effects of inertia in the groove between the pads lead to an inlet pressure build-up at the leading edge. In large and slow speed tilting-pad bearings the inlet pressure build-up is usually negligible indicating that, for such bearings, the effect of inertia on the pressure in a recess is also likely to be small. In sector shaped bearing pads the centrifugal term may cause a shift of the pressure maximum towards the outer radius resulting in a radial tilt of the pad. Shinkle & Hornung (1965) showed the recess flow to be turbulent at $Re = \rho U h_p/\mu > 1.0 \cdot 10^3$. For some of the recess geometries and velocities used in this report, turbulence is to be expected. The function of a deep recess is to create a low friction zone. When inertial end effects in the recess are negligible, the pressure inside it is close to constant regardless of whether the flow is laminar or turbulent. Although the use of the Reynolds equation inside the recess is not strictly valid, the inaccuracies arising from using this equation in a laminar formulation are therefore small. Determining the friction loss in the recess poses a more delicate problem. The friction loss in the bearing is calculated from the shear stress at the collar surface.

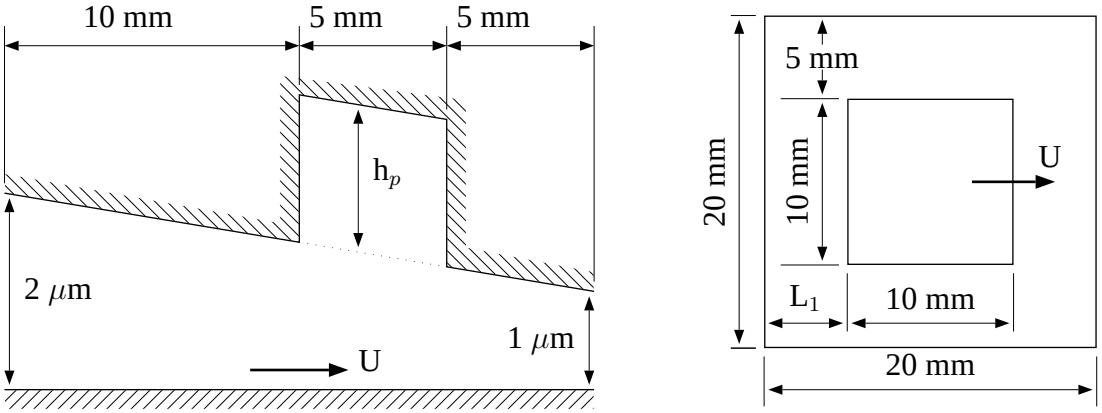

Figure 7.1: Left: The bearing pad used in Brajdic-Mitidieri et al. (2005) for the 1-dimensional analysis. Right: The bearing pad used for the 2-dimensional analysis. The recess is 20 μm deep.

Due to the thick oil film in the recess, the friction is small in this area when the flow is laminar and inaccuracies have a negligible influence on the calculation of the total friction loss. In turbulent flow recesses, the friction is larger and may significantly influence the total friction loss. Based on the work by Shinkle & Hornung (1965) the inaccuracy on the recess and total friction loss is analysed later in this chapter of the report.

The main contribution of this part of the report is related to the study of the influence of equipping tilting-pad bearings with deep recesses in the high-pressure region. It is shown that a significant reduction of the friction loss is possible compared to conventional tilting-pad bearings and it is shown that recesses placed in the high-pressure region can be used for high-pressure jacking.

7.1 Comparison to CFD-Model Results

In an isothermal study, using a CFD-code Brajdic-Mitidieri et al. (2005) investigated the effect of equipping fixed incline bearings with recesses. They found that the friction factor $\eta =$ Friction/Load was significantly reduced when a recesses was placed in the high-pressure region. They presented theoretical results for the 1- and 2-dimensional bearings shown in figure 7.1. The bearings operate at a speed of 1 m/s, a viscosity of 10^{-5} m^2/s and a density of 1000 kg/m^3. In both cases the leading edge oil film thickness is $h_{le} = 2\ \mu\mathrm{m}$ while the trailing edge thickness is $h_{te} = 1\ \mu\mathrm{m}$. In tables 7.1 and 7.2 their results are compared to results obtained with the Reynolds equation based model used in this report. In the 1-dimensional model $n_x \times n_z = 200 \times 10$ control volumes are used. In the 2-dimensional model $n_x \times n_y \times n_z = 100 \times 100 \times 10$ uniformly distributed control volumes are used. Increasing the number of control volumes does not change the values of η_{h_p}/η_0 stated in the tables on the three decimals given. In both the 1-dimensional and 2-dimensional cases, the calculations by Brajdic-Mitidieri et al. show higher friction reductions by the use of recesses than the calculations using the Reynolds equation. The results are however, within 10 % difference and the trends in the calculations are the same suggesting that the analysis of problems of this nature can be performed using the Reynolds equation. It should be noted that the chosen speed and fluid film thickness are

h_p [μm]	Load [kN/m]		Friction [kN/m]		Friction coef. $\eta \cdot 10^4$		η_{h_p}/η_0	
	Bra	Rey	Bra	Rey	Bra	Rey	Bra	Rey
0	634	636	0.153	0.155	2.42	2.43	1	1
5	619	626	0.139	0.141	2.25	2.25	0.926	0.924
10	613	622	0.126	0.133	2.06	2.13	0.845	0.878
20	611	612	0.115	0.126	1.89	2.04	0.779	0.838
30	611	620	0.113	0.124	1.85	2.00	0.762	0.822
40	610	620	0.113	0.122	1.84	1.97	0.759	0.812

Table 7.1: Comparison of results for the 1-dimensional analysis presented by Brajdic-Mitidieri et al. (2005)(Bra) and results obtained using the Reynolds equation(Rey). Results are presented for various recess depths h_p.

L_1 [mm]	Load [kN/m]		Friction [kN/m]		Friction coef. $\eta \cdot 10^4$		η_{h_p}/η_0	
	Bra	Rey	Bra	Rey	Bra	Rey	Bra	Rey
n/p	276	277	0.150	0.145	5.44	5.24	1	1
5.0	220	227	0.119	0.119	5.40	5.26	0.992	1.004
7.5	242	248	0.116	0.116	4.81	4.69	0.884	0.896
8.0	241	247	0.113	0.116	4.79	4.69	0.881	0.895
8.5	235	239	0.115	0.115	4.88	4.79	0.896	0.915

Table 7.2: Comparison of results for the 2-dimensional analysis presented by Brajdic-Mitidieri et al. (2005)(Bra) and results obtained using the Reynolds equation(Rey). Results are presented for various recess positions L_1 (See figure 7.1). n/p indicates a pad without a recess.

small. Effects of inertia become more important with increasing Reynolds number. The Reynolds equation based model may therefore be less accurate at operating conditions usual for thick film bearings. The 1-dimensional analysis shows a reduction of the friction coefficient of approx. 20 % while the 2-dimensional analysis shows a reduction of approx. 10 %. These results are obtained using a fixed convergence ratio $h_{le}/h_{te} = 2$ which is not optimized for achieving a minimum friction coefficient. In the 2-dimensional case $h_{le}/h_{te} = 3\mu\mathrm{m}/1\mu\mathrm{m} = 3$ is a more optimal convergence ratio leading to $\eta = 4.54 \cdot 10^{-4}$ for a non-recessed bearing. This is 3 % less than the minimum value stated in table 7.2.

7.2 Analysis of Tilting-Pad Thrust Bearing

In the following, the effect of equipping the surfaces of tilting-pad thrust bearings with recesses is analysed and design suggestions minimizing the friction loss are stated.

In order to isolate the effects leading to improved performance the problem is investigated using

	$12 \times 12 \times (5+5)$	$24 \times 24 \times (10+10)$	$48 \times 48 \times (20+20)$	$96 \times 96 \times (40+40)$
	Plain bearing pad (8-pad bearing) - (TEHD)			
$\dot{Q}_{gen}$ [kW]	266.39	276.32	279.26	280.02
$\dot{Q}_{out}$ [kW]	274.95	280.46	281.24	281.09
h_{min} [μm]	75.00	75.00	75.00	75.00
T_{max} [°C]	81.80	80.52	78.53	77.69
	Recessed bearing pad (8-pad bear.) - (TEHD)			
$\dot{Q}_{gen}$ [kW]	215.69	231.56	236.42	237.17
$\dot{Q}_{out}$ [kW]	532.42	275.59	241.09	235.43
h_{min} [μm]	75.00	75.00	75.00	75.00
T_{max} [°C]	91.16	76.85	74.76	74.32

Table 7.3: Grid convergence study: $\dot{Q}_{gen}$ is the shear work at the collar surface . $\dot{Q}_{out}$ represents the sum of all heat flows out of the computational domain. h_{min} is the minimum oil film thickness and T_{max} is the maximum temperature in the oil film.

increasingly complex modelling. 1-dimensional modelling shows the potential in reducing friction. Isothermal and 3-dimensional modelling of a rectangular bearing pad documents the influence of finite width, temperature and thermal bending. Finally, modelling of a thrust bearing with sector shaped pads verifies that the method is applicable to real bearings and an analysis of start-up behaviour including hydrostatic jacking shows that recesses placed in the high-pressure region can be used as oil injection pockets as well as for reducing the power loss.

Calculations are carried out on example bearings of large dimensions typical for the use in hydro power plants. In all calculations, the bearings are assumed to operate using a VG32 mineral oil under fully flooded conditions. The data for the oil are: $\mu_{40^oC} = 27.1$ mPas, $\mu_{80^oC} = 6.8$ mPas, $\rho = 848$ kg/m^3, $c = 2090$ J/kg/K, $k = 0.13$ W/m/K. The recess depth is 4 mm corresponding to $53h_{min}$.

Table 7.3 shows a grid convergence study performed on a sector shaped 8-pad bearing. Results are stated for bearings both with and without a recess covering approx. 18 % of the pad area. For a fixed minimum oil film thickness and variable pad area, the top study shows the convergence of friction loss, total heat loss, minimum oil film thickness and maximum temperature for a non-recessed pad. The heat loss converges towards the generated shear work, $\dot{Q}_{gen}$ which is the parameter used throughout this chapter of the report for the friction loss. The bottom study shows the convergence of the calculations of the recessed pad. They converge much more slowly with increasing grid size. At the grid size used throughout this chapter: $n_r \times n_\theta \times (n_z + n_{z_{pad}}) = 24 \times 24 \times (10+10)$ the heat loss is 19 % higher than the generated friction loss. At larger grid sizes, the values converge towards each other. $\dot{Q}_{gen}$ for the grid of $24 \times 24 \times (10+10)$ control volumes is within 2.5 % of the value obtained using $96 \times 96 \times (40+40)$ control volumes. For comparing friction losses between recessed and non-recessed pads this is a reasonable accuracy on the generated friction.

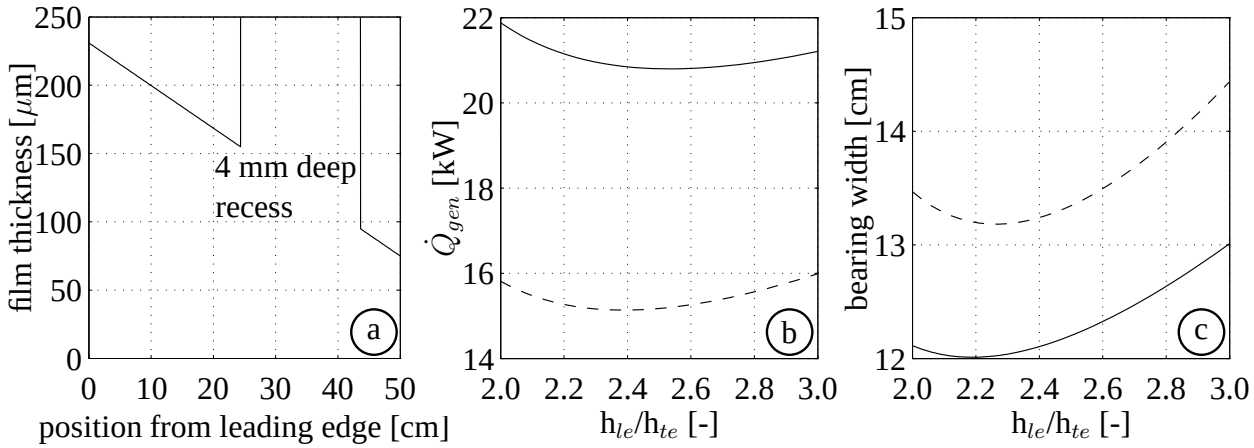

Figure 7.2: (a) Figure showing the position of the pocket. (b) The generated friction loss. By introducing the recess shown the minimum friction loss is reduced by 27 %. (c) Bearing width leading to a minimum oil film thickness of 75 μm for a load of 1.0 MN. In (b) and (c) full lines indicate a plain bearing pad and dashed lines indicate a bearing with a 4 mm recess.

7.2.1 1-dimensional isothermal analysis of a linear bearing

The problem is analysed using the 1-dimensional Reynolds equation and isothermal operating conditions (55 °C). A bearing pad with a length of 0.5 m operating at a speed of 30 m/s and a load of 1.0 MN is considered. A 4 mm deep recess is machined in the surface of the bearing. A parameter study has shown that a recess of width and position as shown in figure 7.2(a) gives the minimal friction loss. The recess covers 38 % of the bearing area. The width of the bearing is adjusted to give a minimum oil film thickness of 75 μm. Figure 7.2(b) presents the generated friction loss with and without a recess for different oil film thickness convergence ratios. By introducing the recess, the minimum friction loss is reduced by 27 %. Figure 7.2(c) shows the bearing width. Introducing the recess increases the necessary width corresponding to a reduction in load carrying capacity per unit width of approx. 10 %.

7.2.2 Analysis of a bearing with rectangular bearing pads

Rectangular pads of different length-to-width ratios are studied. The rotor temperature is 55 °C, the oil bath temperature is 40 °C and the leading edge temperature is set equal to the rotor temperature. The speed is 30 m/s and one pad carries a load of 1.0 MN. The numerical model adjusts the bearing surface area to achieve a minimum oil film thickness of 75 μm. As the pads are considered symmetrical, the minimum oil film thickness is located at the centre of the trailing edge. Rectangular and elliptical pockets have been studied and the elliptical pockets have proven more optimal. In the following only elliptical pockets with a uniform depth of 4 mm are considered. In figure 7.3 a drawing of a pad is seen and the nomenclature used to define the recess and pad geometries is presented. All pads have a thickness of 0.3 m. Pads with length-to-width ratios of 0.2 to 2.0 are studied. $n_r \times n_\theta \times (n_z + n_{z_{pad}}) = 24 \times 24 \times (10 + 10)$ control volumes are used in the calculations.

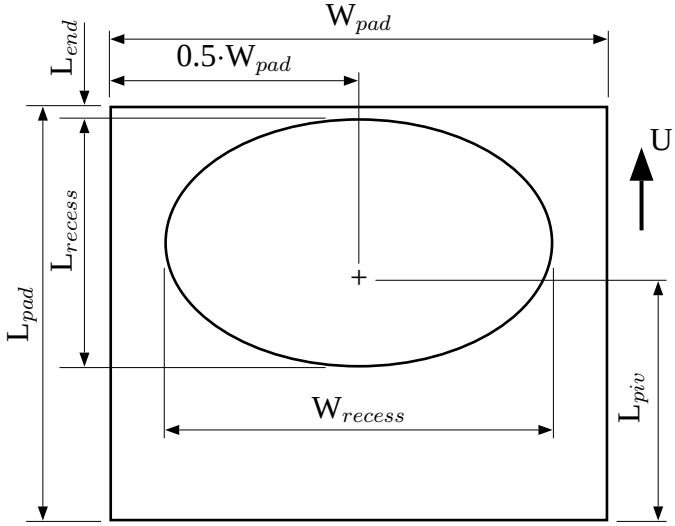

Figure 7.3: Drawing of a rectangular pad with a recess. L_{pad} and W_{pad} define the pad length and width. L_{piv} denotes the distance of the spherical pivot from the leading edge of the pad. L_{recess} and W_{recess} denote the minor and major axis of the elliptical recess and L_{end} defines the position of the recess relative to the trailing edge.

An isothermal parameter study has determined optimal values of L_{recess} and L_{end} as stated in figure 7.4(a), while $W_{recess} = 0.78 \cdot W_{pad}$ is a good value for the recess width at all length-to-width ratios. With these values, the optimal positions of the pivot point for pads with and without recesses are shown in figure 7.4(b). The positions are given for isothermal (ISO) calculations, thermo-hydrodynamic (THD) calculations not including the bending of the bearing pad and for thermo-elasto-hydrodynamic (TEHD) calculations including bending. The pads, which are considered, are of large sizes where thermal bending has a significant influence on the oil film thickness. In smaller bearings, thermal bending has a smaller influence. For most bearing dimensions the optimal position of the pivot is therefore located between the positions suggested by the THD- and the TEHD-analysis. For recessed pads with small or no thermal deformation, the isothermal analyses determine optimal pivot positions close to those suggested by THD-analyses. For conventional bearing pads, isothermal analyses are less accurate. In figure 7.4(c) two sets of curves are shown. The curves marked with (I) represent the percentage increase in the pad surface area with a recess in the pad surface relative to the area of a pad without a recess. The curves marked with (II) represent the area of the recess relative to the area of a pad without a recess. In the THD-analyses the increase in total pad area $L_{pad} \cdot W_{pad}$ when introducing recesses in the surfaces is much smaller than the recess areas. Following the design suggestions given in figure 7.4(a)$-$(b), the pad areas should be increased by approximately $10-15$ % relative to the areas of pads without recesses in order to achieve the same minimum oil film thickness. When pad bending is included, this result is more complex. At small and large length-to-width ratios, the mean pad bending is large as can be seen in figure 7.4(d). Due to larger pad areas, the recessed pads experience larger thermal bending and this reduces the load carrying capacity. In figure 7.4(e) the power consumption is shown. The THD-analysis indicates that a length-to-width ratio of approx. 0.6 is optimal for a recessed bearing pad.

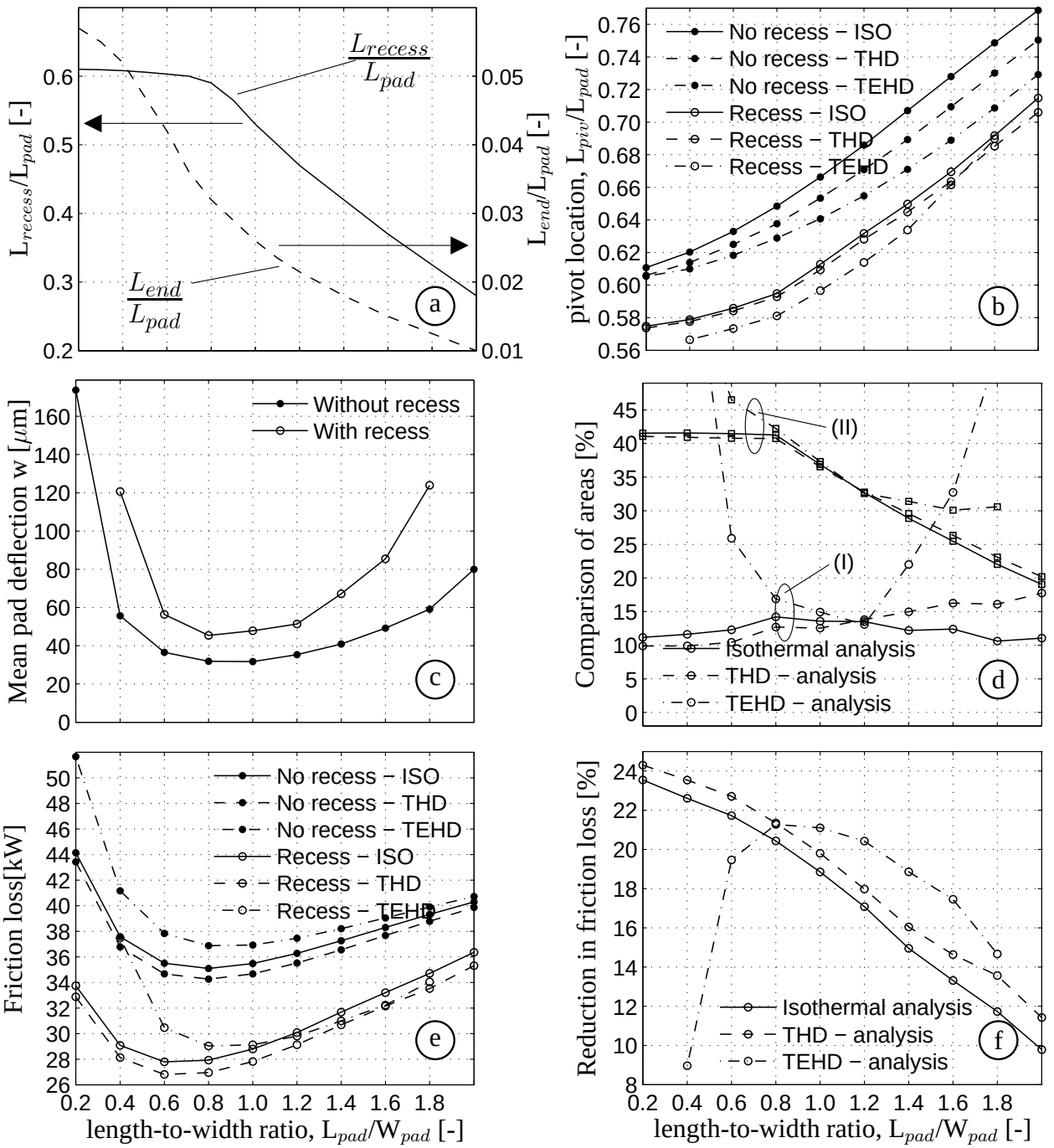

Figure 7.4: (a) and (b) state design parameters defining the recess geometry and the pivot position for rectangular pads. The values are chosen to minimize the friction loss. In (c) two sets of curves are shown. The curves marked with (I) represent the percentage increase in the pad surface area with a recess in the pad surface relative to the area of a pad without a recess. The curves marked with (II) represent the area of the recess relative to the area of a pad without a recess. (d) shows values of thermal bending, (c) states the friction loss and (d) the reduction in friction for recessed bearing pads relative to non recessed pads.

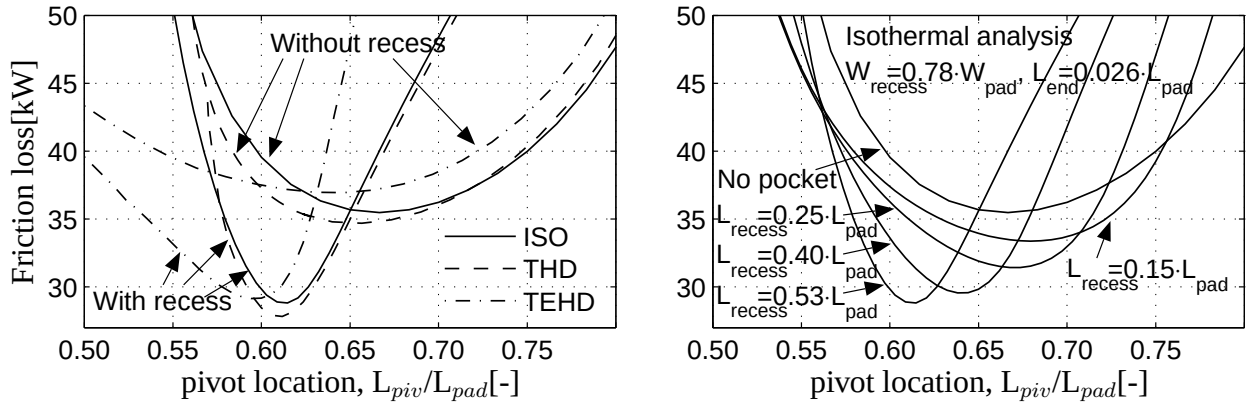

Figure 7.5: Left: Friction loss as a function of pivot position. Right: Isothermal analysis showing the influence of the length of the recess on the friction loss.

The value is approx. 0.8 for a non-recessed pad. With pad bending included larger ratios give good results. At low length-to-width ratios, the bending of the pad in the direction perpendicular to the sliding direction is very large. In a non-recessed bearing, this leads to a higher pressure-maximum than when there is no thermal bending. In the recessed bearing, the area of maximum pressure stretches radially into areas of large film thickness leading to a large amount of side leakage. For low length-to-width ratios, the recessed pads therefore do not perform well. Figure 7.4(f) states the percentage reduction in friction loss when using recessed pads - compared to bearings with plain pads. With small length-to-width ratios, the improvement in performance is close to the 27 % obtained in the 1-dimensional analysis for an infinitely wide slider bearing. As the length-to-width ratio increases, the improvement is less significant.

Figure 7.5 shows a study of the influence of the pivot location on the friction loss of the bearing with a length-to-width ratio of 1.0. In figure 7.5(left) it is seen that the optimum is more clearly defined when a recess with the suggested dimensions is machined in the pad surface. It is therefore important to place the pivot point correctly in order to achieve an energy saving. Figure 7.5(right) shows an isothermal analysis of the influence of the recess length. For decreasing recess size, the optimum becomes more flat and the bearing is therefore less sensitive to incorrect positioning of the pivot point. This improvement in behaviour is a trade off against a larger friction loss. In all the examples studied in figure 7.5(right) the position of the recess is chosen so that $L_{end} = 0.026 \cdot L_{pad}$. This has proven to be a good strategy when trying to make the bearing less sensitive to pivot positioning while still obtaining a relatively small friction loss. However, as seen in figure 7.5(right) the optimal position of the pivot point moves in the direction of the trailing edge as the recess size decreases. The suggestions for positioning of the pivot point given in figure 7.4(b) are therefore only valid for the recess lengths given in figure 7.4(a). With the size suggested in figure 7.4 ($L_{recess} = 0.53 \cdot L_{pad}$), the value is 0.615 while it is 0.68 for a pad with $L_{recess} = 0.15 \cdot L_{pad}$.

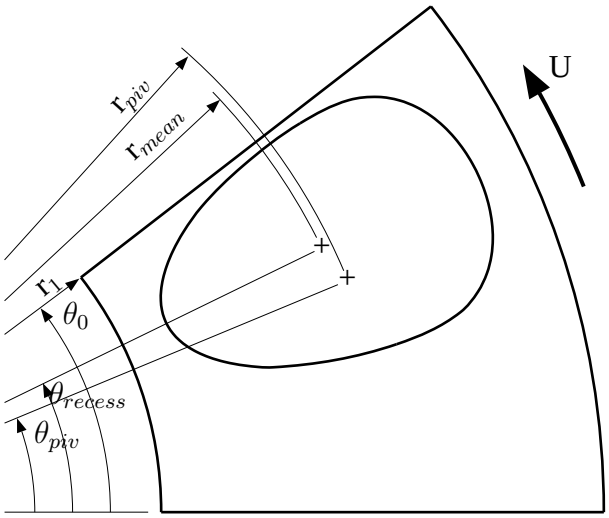

Figure 7.6: The sector shaped bearing pad considered. The recess size and position are defined by equation 7.1.

7.2.3 3-dimensional analysis of tilting pad thrust bearing

Tilting-pad thrust bearings with 4, 5, 6, 8, 12 and 18 pads are studied. The mean radius is 0.8 m. The widths of the bearings vary from 0.55 m to 0.65 m depending on the number of pads. The angular extend of all pads in a bearing is $280-320°$. All pads have a thickness of 0.3 m. The rotor temperature is 55°C and the oil bath temperature is 40°C. The leading edge temperature to each pad is determined from a control volume analysis of heat transfer in the groove between the pads as described in Heinrichson et al. (2006). The speed is 400 rpm and the bearings carry loads of 5.0 MN. The numerical model adjusts the bearing surface area and the radial position of the pivot point to achieve a minimum oil film thickness of 75 μm at the centre of the trailing edge. As discussed later in this chapter, positioning the pivot at the mean radius does not yield good results for pads with recesses as it may result in significant radial tilting of the pads. Therefore, this restriction is introduced on the pivot position. The sizes and positions of the recesses are as stated in figure 7.4(a) for rectangular bearing pads. A drawing of a sector shaped pad is seen in figure 7.6. The elliptical recess is stretched with the circumferential length of the pad and the recess circumference is given by the equation:

$$\frac{(r \cdot \cos[\theta - \theta_{recess}] - r_{mean})^2}{(W_{recess}/2)^2} + \frac{(r \cdot \sin[\theta - \theta_{recess}])^2}{(L_{recess}/2)^2 \cdot r/r_{mean}} = 1 \tag{7.1}$$

where θ_{recess} is the angular centre of the recess determined so that L_{end} as given in figure 7.4(a) is the distance between the recess and the trailing edge at the mean radius. W_{recess} is the maximum extent of the recess in the radial direction. L_{recess} denotes the extent of the recess perpendicular to the radial direction in the point defined by θ_{recess} and r_{mean}.

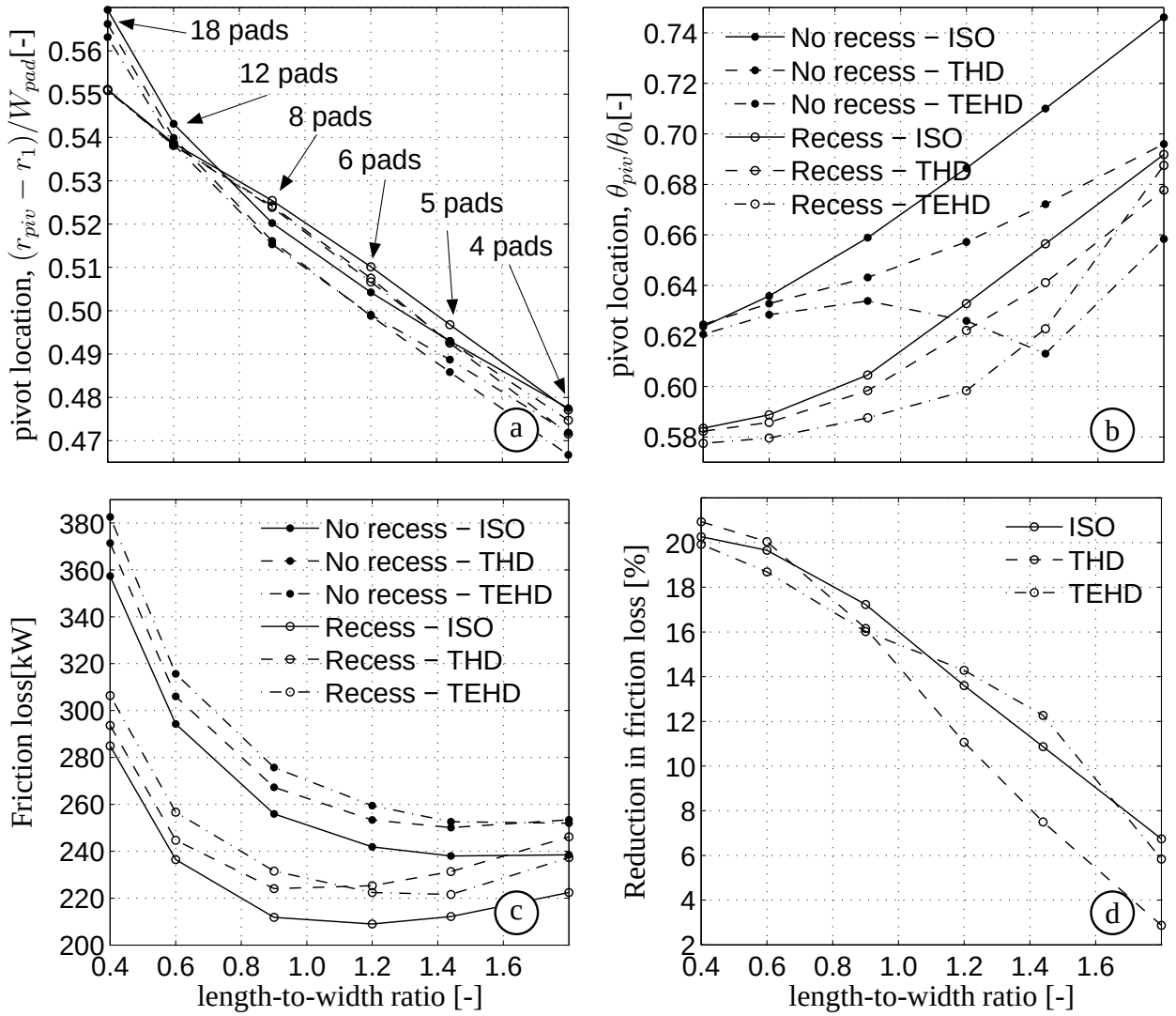

Figure 7.7: (a) and (b) state the radial and circumferential pivot position for sector shaped pads with and without recesses. The values are chosen to minimize the friction loss and are stated for various length-to-width ratios. The pad length is defined as $L_{pad} = \theta_{pad} \cdot r_{mean}$. (c) states the friction loss and (d) the reduction in friction for recessed bearing pads relative to non recessed pads.

Figure 7.7(a) shows the radial position of the pivot point which leads to a minimum oil film thickness at the centre of the trailing edge. The results of the different simulations are hard to distinguish from each other as they show the same trend. The usual praxis of positioning the pivot at the mean radius fulfils the criteria of a minimum oil film thickness at the centre of the trailing edge at a length-to-width ratio of approx. 1.2. Positioning the pivot at the mean radius leads to a minimum oil film thickness at the inner trailing edge corner at low length-to-width ratios. At high ratios, the minimum oil film thickness is located at the outer trailing edge corner. Figure 7.7(b)

shows the optimal position of the pivot point in the circumferential direction. The THD-analyses of the recessed bearing pads lead to positions almost identical to those obtained with a rectangular pad. The TEHD-results cannot be compared as the pad thickness relative to the pad area is different in the analyses of rectangular and sector shaped pads. The non-recessed bearing behaves in a peculiar way under the influence of pad bending. The optimal pivot location first rises with the length-to-width ratio from a ratio of 0.4 to 0.8 then falls from a ratio of 0.8 to 1.4. From a ratio of 1.4 to 1.8 it sharply rises. The thermal bending of the pad increases with the pad length-to-thickness ratio and to achieve an advantageous pressure distribution the nondimensional pivot location moves towards the centre of the pad for higher length-to-width ratios. At a ratio of 1.8, this leads to cavitation at the trailing edge. That is disadvantageous for the power loss because the friction loss in the regions with cavitation is large while there is no contribution to the pressure build-up. The optimal position of the pivot is therefore closer to the trailing edge leading to a higher tilting angle and no cavitation. The same phenomenon is responsible for the position of the pivot of the 4-pad bearing equipped with a recess. Figure 7.7(c) shows the friction loss. THD-analysis indicates an optimal length-to-width ratio of approx. 1.5 for a non-recessed bearing while it is approx. 1.0 for a recessed bearing. Both with and without recesses the optimum length-to-width ratio is larger when thermal bending is considered. Figure 7.7(d) shows the reduction in friction loss when using recessed bearing pads - compared to bearings with plain pads. The reduction is smaller than what was obtained for rectangular pads. This is as expected as the recess sizes and positions have been optimized for rectangular pads and not for sector shaped pads. For the common 6 to 8-pad bearings with length-to-width ratios of 0.8 to 1.2 the reduction in friction is around 10-15 %.

The recess creating a high-pressure zone inside the recess controls the pressure distribution. The bearing pads therefore loose some of their tilting stability in the radial direction as seen in figure 7.8(top-left) showing the minimum oil film thickness obtained when radially moving the pivot point of the 8-pad bearing. The recessed bearing pad is much more sensitive to radial positioning of the pivot point than the non-recessed pad. The pad is therefore also sensitive to inertial effects in the radial direction in the recess. The centrifugal force acting on the recess oil may cause an oil flow towards the outer trailing edge leading to a radial tilt of the pad. Figure 7.8(middle-left) shows the effect of reducing the recess width on the radial tilting stability while 7.8(bottom-left) shows the corresponding friction losses. A narrower recess improves the tilting stability but at the cost of a much higher friction loss. The reduction in radial tilting stability compared to conventional tilting-pad bearings makes it difficult to obtain an improvement in performance by the use of enclosed recesses when using point pivots. Spring bed bearings or Michell type bearings with line pivots instead of point pivots do not suffer from tilting stability problems in the radial direction. Such a characteristic suggests that designing with enclosed recesses may result in good design alternatives reducing the friction in these types of bearings.

Figure 7.8(top-right) shows the minimum oil film thickness as a function of the circumferential position of the pivot point. The optimum is more clearly defined when a recess is machined in the surface. Figure 7.5(left) documented a similar characteristic for a rectangular pad. Figure 7.8(middle-right) shows an isothermal analysis of the influence of the circumferential length of the recess on the behaviour of the optimum. Equivalent to the results presented in figure 7.5(right) for a rectangular pad, figure 7.8(middle-right) documents that a reduction of the recess length reduces the circumferential sensitivity to the pivot location. Within the range of dimensionless pivot locations shown a recess length of $L_{recess} = 0.20 \cdot L_{pad}$ gives a flatter and therefore more desirable

Dependency of the radial position of the pivot point and the radial size of the recess.

Dependency of the circumferential position of the pivot point and the circumferential size of the recess.

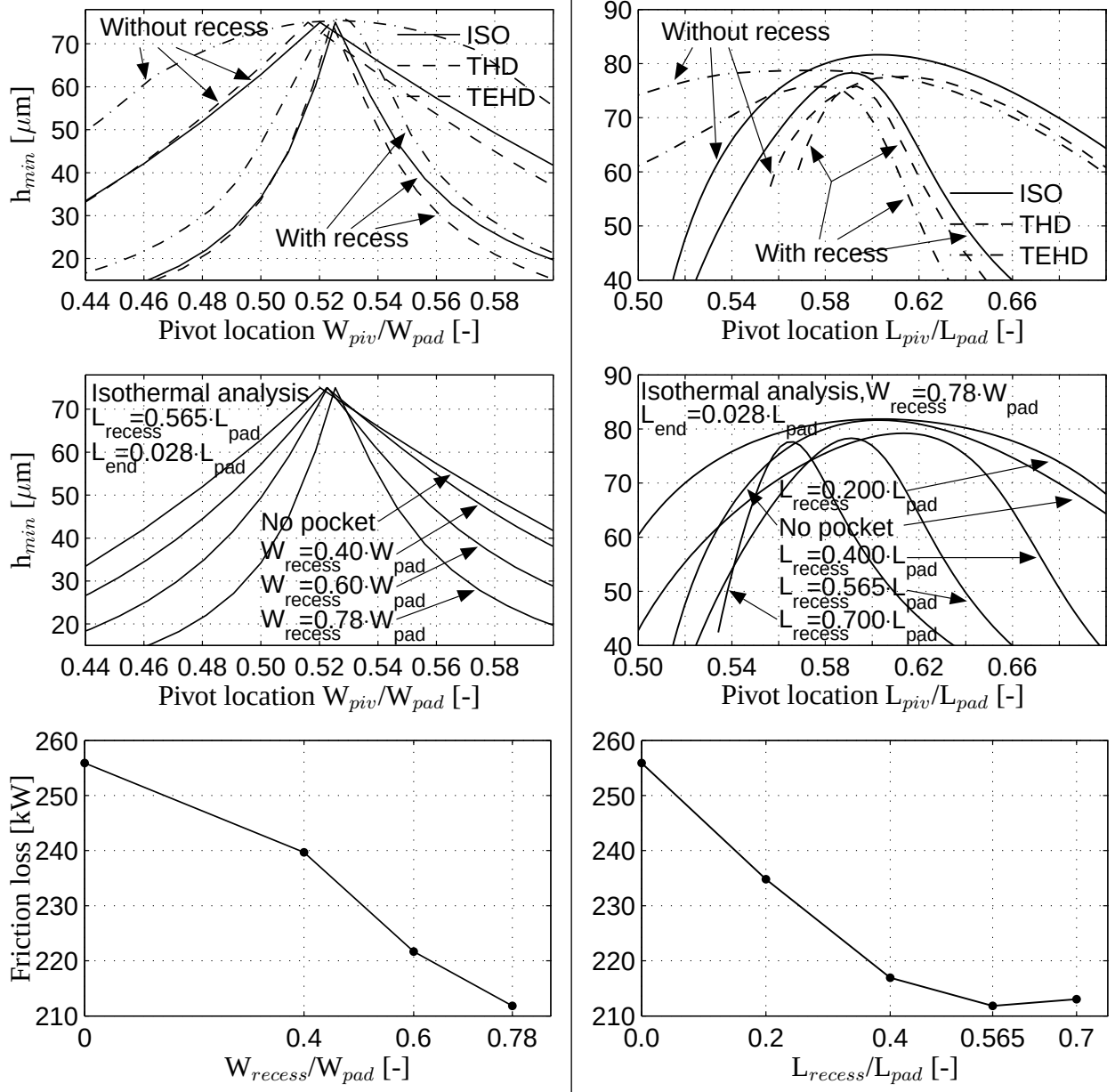

Figure 7.8: The influence of varying the pivot location radially (left) and circumferentially (right). Top: Minimum film thickness as a function of the pivot position for the 8 pad bearing. Middle: Isothermal analysis of the influence of recess size on the minimum film thickness. Bottom: The minimum obtainable friction loss for the recess sizes shown in the middle figure.

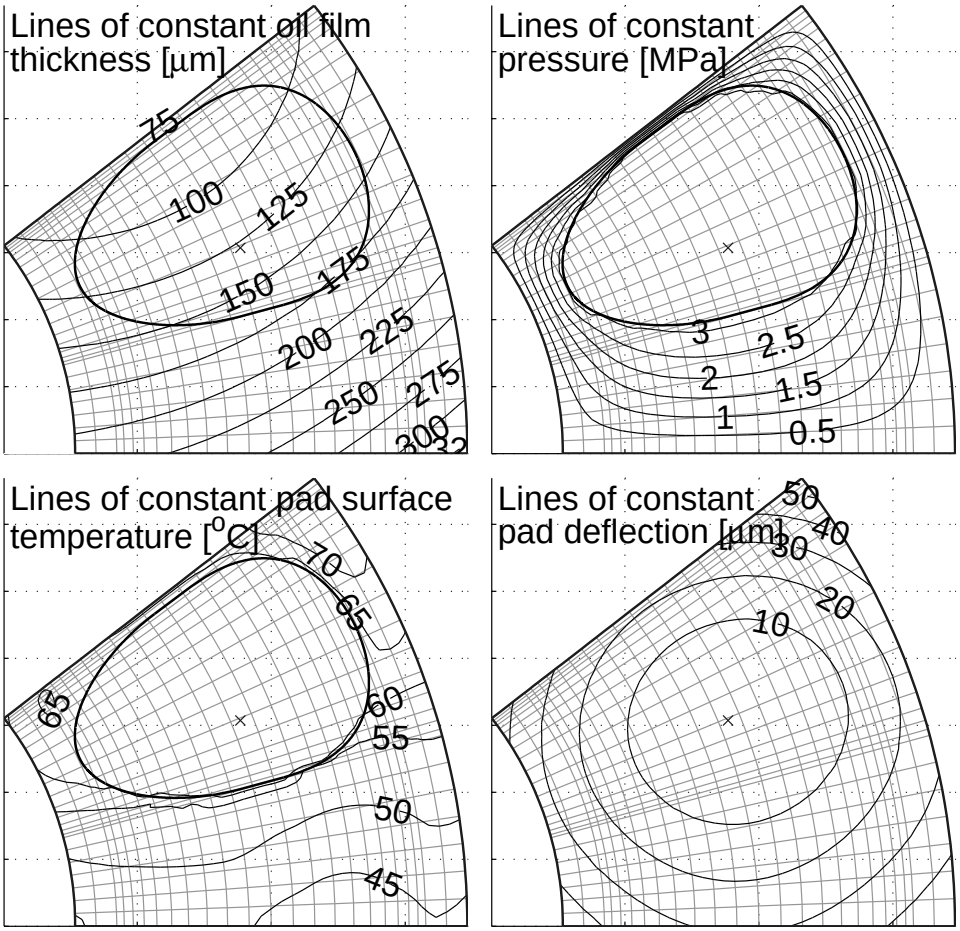

Figure 7.9: Results from the TEHD-analysis of the 8 pad bearing.

behaviour than the non-recessed bearing pad while still reducing the friction by 9 % (see figure 7.8(bottom-right)).

Figure 7.9 illustrates simulation results for the 8-pad bearing. The figure shows graphic illustrations of oil film thickness, pressure, pad surface temperature and pad bending. The analysis has shown that the minimum friction loss is achieved when the pressure maximum covers the recess area as it is seen in the figure. Positioning the recess closer to the pad centre causes a pressure peak downstream of the recess.

7.2.4 The influence of recess depth

The depth of the recess influences the shear stress at the collar surface and thereby the friction loss. Figure 7.10 presents a study of the influence of the recess depth on the friction loss in the 8-pad bearing defined by the design values stated in figure 7.7. A recess depth of $h_p = 4$ mm corresponding to a recess Reynolds number of $Re = 4.2 \cdot 10^3$ is used throughout this chapter of the report. Using a laminar formulation the friction loss inside the pocket is 11.8 kW corresponding to

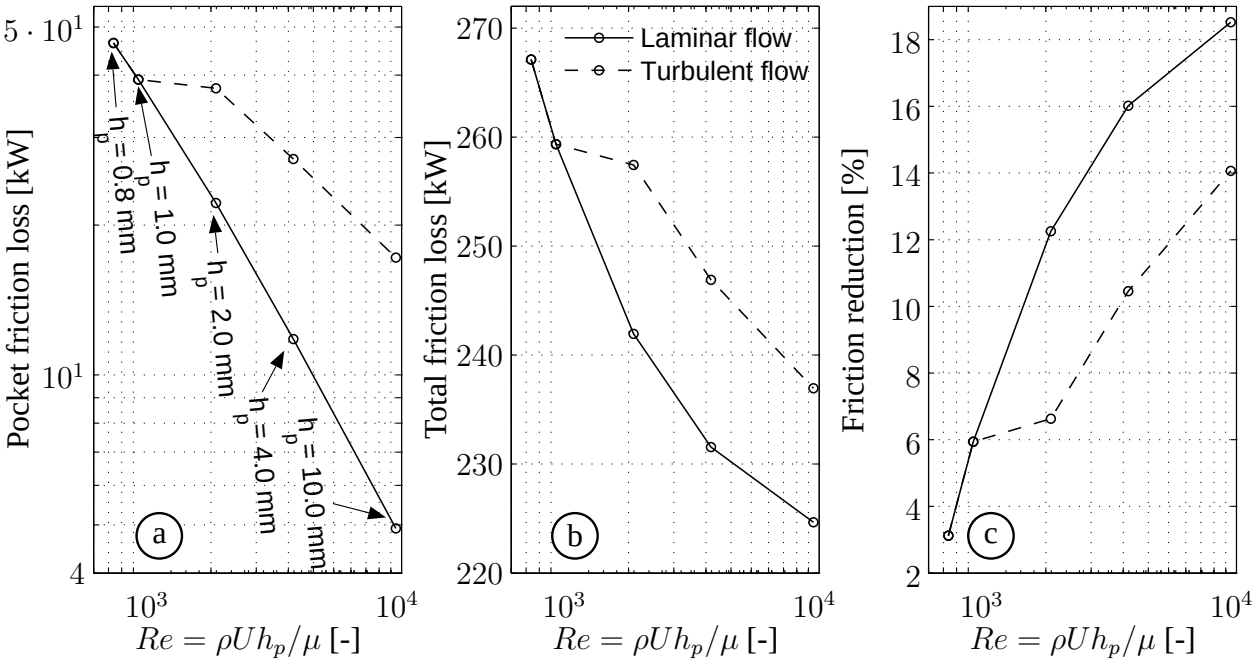

Figure 7.10: The influence of recess depth on the friction loss. Full lines indicate results obtained with the laminar model. Dashed lines indicate estimates of the influence of turbulent recess flow. (a) The friction loss in the pocket area. (b) The friction loss in the bearing. (c) The friction reduction relative to an optimal non-recessed bearing.

5 % of the total friction loss. However, at $Re = 4.2 \cdot 10^3$ the flow is turbulent as determined by Shinkle & Hornung (1965). They presented measurements of the friction factor for a hydrostatic journal bearing with various pocket depths. For $Re < 1.0 \cdot 10^3$ the friction factor is proportional to Re^{-1} and the recess flow laminar. At the shift to turbulent flow the friction factor increases slightly (< 10 %). At increasing turbulent Reynolds numbers the factor decreases. The results of Shinkle & Hornung (1965) are used to estimate the influence of turbulence on the results presented in this chapter. At $Re = [2 \cdot 10^3, 4 \cdot 10^3, 1 \cdot 10^4]$ the amounts of turbulent friction are [1.7, 2.3, 3.5] times the values for laminar flow. Estimates using these amounts are presented in figure 7.10(a). For the 4 mm deep recess this raises the recess friction by a factor of approx. 2.3 and the total bearing friction loss is increased by 6.6 %(figure 7.10(b)). Figure 7.10(c) shows the reduction in friction relative to a non-recessed bearing of optimal design as defined by the design values of figure 7.7. The reduction in friction is significantly smaller when turbulence is taken into account. This does not generally change the results presented in figures 7.4 and 7.7. The designs suggested in these figures are applicable irrespective of size and operating conditions. The influence of turbulent recess flow on the friction loss however depends on the Reynolds number and thereby the bearing design, operating velocity and oil.

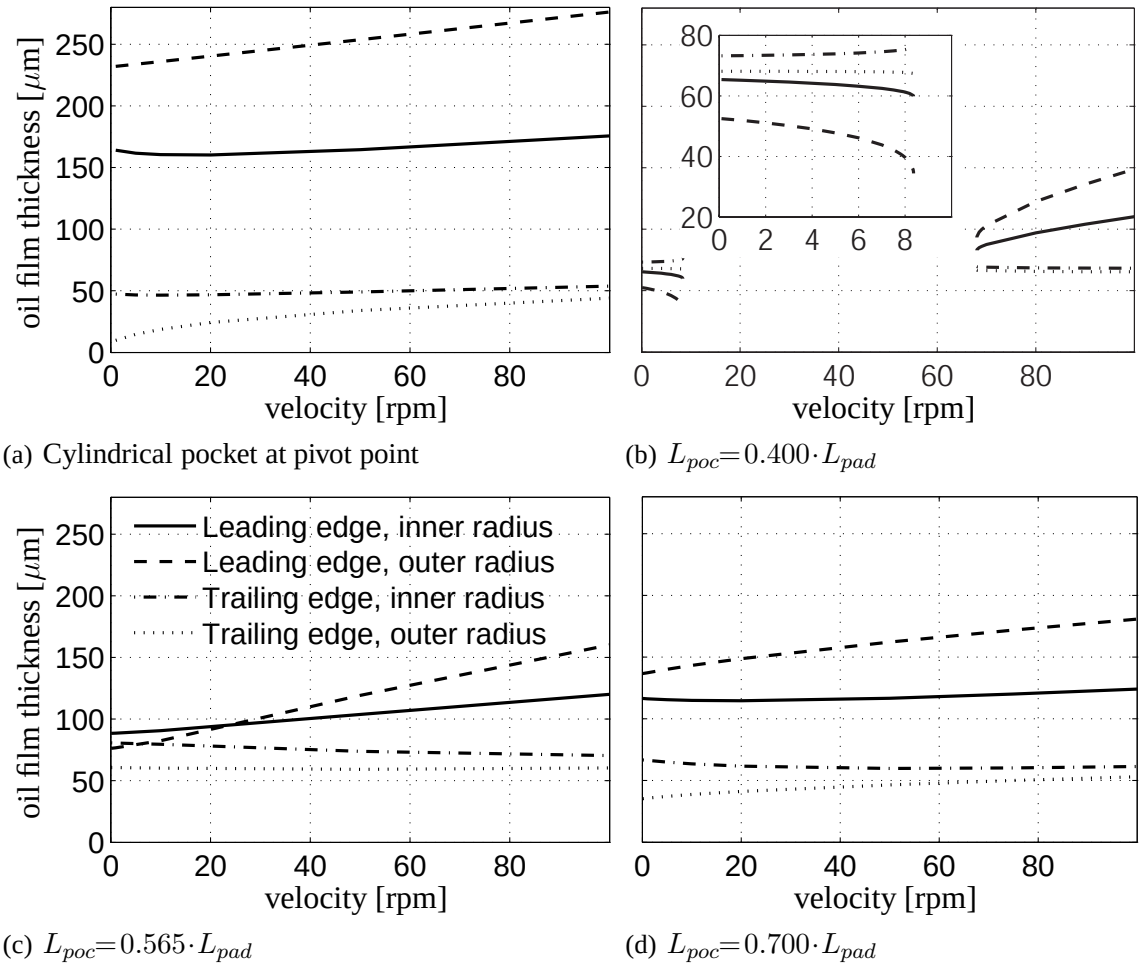

(a) Cylindrical pocket at pivot point

(b) L_{poc}=$0.400 \cdot L_{pad}$

(c) L_{poc}=$0.565 \cdot L_{pad}$

(d) L_{poc}=$0.700 \cdot L_{pad}$

Figure 7.11: Behaviour of bearings with various recess sizes subject to hybrid lubrication at different velocities. The oil film thicknesses at the four corned points are presented. The line legend for all four figures is stated in (c).

7.2.5 Recesses used for hydrostatic jacking

An isothermal analysis is performed in order to study the behaviour of the bearing pads when operated using hybrid lubrication. Pads similar to those studied in figure 7.8(middle-right) without high pressure jacking are now operated with a $2{\cdot}10^{-4}$ m^3/s volume flow of oil injection at the centres of the recesses. The conventional bearing pad without recess is equipped with a cylindrical oil injection pocket covering 5 % of the bearing surface area and located at the pivot point.

In figure 7.11 the oil film thicknesses at the four corners of the pads are shown for velocities ranging from 0 to 100 rpm. Figure 7.11(a) shows oil film thicknesses for the conventional pad with an oil injection pocket. The pad has a significant radial tilt at start-up with a minimum oil film thickness of 10 μm. When increasing the speed the circumferential tilting angle remains close to constant. Figure 7.11(b) shows that there is a negative circumferential tilting angle at start-up for the bearing with a recess of length $L_{recess} = 0.400 \cdot L_{pad}$. As rotation is initiated the minimum

oil film thickness at the leading edge of the pad drops. For velocities of 8 to 68 rpm the numerical solution of the problem has not been possible. In this region of velocity the tilting angle changes from negative to positive. This behavior of the pad at start up is undesirable as the increasingly negative tilting angle as the collar is accelerated from zero velocity could lead to mixed lubrication and wiping of the bearing pad. Flutter of the pad may occur at the transition from a negative to a positive tilting angle. In figure 7.11(c) the pad with $L_{recess} = 0.565 \cdot L_{pad}$ is seen to have a slight positive tilting angle at zero velocity while figure 7.11(d) shows a better start-up behavior for $L_{recess} = 0.700 \cdot L_{pad}$. Due to the smaller tilting angle the minimum oil film thickness at zero velocity is larger for this bearing than it is in bearings with conventional oil injection pockets. The figure shows that recesses can be used as oil injection pockets provided that care is taken toward achieving positive tilting angles at the start-up conditions. This can be achieved by increasing the length of the recess. Alternatively, the recess can be moved towards the centre of the pad. The good behavior seen in figure 7.11(d) is achieved at the cost of a slightly higher friction loss as it was shown in figure 7.8(b-right). However, as shown in figure 7.8(b-left) a bearing with a longer recess is more sensitive to the circumferential positioning of the pivot point.

7.3 Conclusion

A 3-dimensional thermo-elasto-hydrodynamic laminar flow model based on the Reynolds equation has been used to study the effect of equipping tilting-pad thrust bearings with deep recesses with the purpose of reducing the friction loss. A comparison to results obtained using a CFD-code to analyse recesses in fixed incline bearing pads published by Brajdic-Mitidieri et al. (2005) has been performed. The two methods of analysis give similar results indicating that problems of this nature can be analysed using the Reynolds equation.

A 1-dimensional isothermal analysis of an infinitely wide slider bearing has shown that by placing a recess in the high pressure zone close to the trailing edge it is possible to reduce the minimum friction loss by 27 %.

In a bearing pad of finite width the potential for reducing friction is smaller. A study of rectangular bearing pads shows a 10 % reduction with a length-to-width ratio of 2.0 while a larger energy saving is possible for low length-to-width ratios. At a ratio of 0.2, a saving of 24 % is possible. Optimal values of recess lengths and widths, and the corresponding optimal positions of the pivot points are stated for length-to-width ratios ranging from 0.2 to 2.0. An analysis shows that the sensitivity of the bearing pads to the circumferential positioning of the pivot is greater than in conventional bearings. In order to achieve a performance superior to that of a conventional bearing it is therefore imperative that the pivot is placed close to the optimal position.

The design suggestions given for rectangular pads have subsequently been applied to sector shaped thrust bearings. For the common 6 to 8-pad bearings an energy saving of $10 - 15$ % is obtained. The bearing pads are very sensitive to the radial position of the pivot point. Spring bed bearings or Michell type bearings with line pivots are therefore preferable to bearings with spherical pivots.

The design charts presented in figure 7.4(a)$-$(c) are intended to state the necessary geometric changes when redesigning a tilting-pad thrust bearing from a conventional design with plain pads to a design with deep recesses in the high-pressure regions. However, it has been shown in figure 7.5

that the sensitivity of the bearing operating parameters to small changes in the design and to changes in the boundary conditions is larger than when using conventional bearing pads. For instance, the influence of the leading edge pressure build-up or geometric inaccuracies on the oil film distribution is larger than in conventional bearings.

At recess Reynolds numbers higher than $1.0 \cdot 10^3$ the recess flow is turbulent. This does not change the design suggestions but the energy saving is reduced.

Recesses with the suggested sizes and positions can be used as oil injection pockets for hydrostatic jacking at start-up. Because they are positioned to the trailing edge side of the pivot point, the pads may however tilt backwards at start-up. This could lead to pad flutter and mixed lubrication when accelerating the rotor. Using recesses with larger circumferential dimensions can solve this problem by guaranteeing positive circumferential tilt at lift off.

Chapter 8

Summary and Conclusion

Historically the analyses of tilting-pad thrust bearings have generally not included cutouts in the pad surfaces. Pockets are however often machined in the surfaces to allow for hydrostatic jacking in the start-up phase and inlet tapers are sometimes used to aid the build-up of the oil film. The question is therefore raised, how such cut-outs influence the bearing operation and whether the position of the pivot point leading to the smallest friction coefficient is significantly affected by such features. A more general question is whether cutouts of arbitrary shape and position, deep or shallow could enhance the performance of tilting-pad thrust bearings by reducing the friction loss.

A theoretical approach is chosen in the attempt to answer these questions. Numerical models are constructed which include the phenomena treated in state of the art models of tilting-pad thrust bearings. These are the hydrodynamic pressure build-up as described by the Reynolds equation, temperature variations along and across the fluid film and through the pads, bending of the bearing pads due to pressure and thermal gradients and heat transfer phenomena at the free sides of the pads and in the grooves between the pads. Furthermore, the models allow for the inclusion of recesses of arbitrary shape in the bearing surfaces. Models are constructed for two separate classes of recesses. "Deep recesses" which are two or more orders of magnitude deeper than the oil film thickness are studied using a model including 3-dimensional treatment of the temperatures in the oil film and in the pads. In such recesses, there is a recirculating flow and a large amount of mixing of the oil. This mixing may be helped by turbulence. While the temperatures in the oil film are calculated on a 3-dimensional grid the oil in the recess is considered isothermal. "Shallow recesses" constitute another class of recesses. They have a depth of the same order of magnitude as the oil film. In such recesses, there is no backflow and the oil does not mix as it does in deep recesses. A 2-dimensional bulk flow treatment of the oil film temperatures is used for the analysis of bearings with this feature.

Both models are validated against measurements available in the scientific literature performed on a bearing with plain bearing pads. Furthermore, the 3-dimensional model is validated against measurements made on a bearing of large size, which has pockets for hydrostatic jacking at the pivot points. The results show reasonable agreement with the measurements although some discrepancies exist concerning the tilting-angle. The measurements in the plain bearing pads indicate a higher circumferential tilting-angle than the angle predicted by the models. An independent comparison available in the literature shows the same discrepancy. The ability of the 3-dimensional model to predict the pressure distribution in an oil injection pocket is validated through an experimental study. Individual pads with conical oil injection pockets are tested in a test-rig. At moderate loads (0.5 $\rightarrow$

1.5 MPa mean pressure), measured pressure profiles show good resemblance with the theoretically predicted pressures. At a mean pressure of 4 MPa the discrepancies between results are larger. It is argued that this may be due to the unevenness of the collar.

Tilting-pad thrust bearings of standard design are studied. The influences of varying the length-to-width ratio, varying the pocket sizes and varying the deformation of the pads are studied. Design suggestions are stated based on the results. The oil injection pockets influence the pressure distribution and thereby the optimal position of the pivot point, which moves towards the centre of the pad with increasing pocket size. Length-to-width ratios of $0.8 \rightarrow 1.8$ are shown to give the lowest friction loss. The best choice in this interval depends on the curvature of the pads.

Parallel-step bearings theoretically have smaller friction coefficients than tilting-pad bearings. They however suffer from the disadvantage, that they do not perform well at varying operating conditions. The advantages of tilting-pad bearings can be combined with those of parallel-step bearings by machining shallow inlet pockets in the surfaces of the tilting-pads. The friction loss can thereby be reduced by 10 - 15 % in comparison to that of a standard tilting-pad bearing. Suggestions for the dimensions of the inlet pocket are stated in the report and it is shown that the modified bearings are tolerant to varying operating conditions and wear of the pad surfaces. Such bearings however suffer from a high sensitivity to the position of the pivot point, i.e. the oil film thickness is reduced more rapidly with the offset of the pivot from the optimal position than is the case in standard tilting-pad bearings. Placing the pivot too far in the direction of the leading edge may cause the bearing to entirely loose its load carrying capacity.

A deep recess in the surface of a bearing pad constitutes a low friction zone of nearly constant pressure. Placing such a recess in the high-pressure area of a bearing pad can reduce the friction coefficient, as the reduction of friction due to the low friction zone is higher than the loss of load carrying capacity due to the reduced area of converging oil film. Depending on the length-to-width ratio of the bearing pads the reduction in the friction coefficient can be as much as 27 %. Just as is the case with the bearings with inlet pockets, this bearing design also suffers from a higher sensitivity to the circumferential position of the pivot. This sensitivity can however be reduced, even to a lower level than in standard bearings by changing the pocket geometry. This raises the friction coefficient but substantial savings are still possible when comparing to standard bearings. The recess creates a zone of constant high pressure. Therefore, the radial tilting-stability of such bearings is very low. The pressure distribution is affected little by radial tilting and the compensation which occurs within standard bearing pads by the shift of the pressure maximum is much smaller in recessed bearings. It is therefore not recommended to use this approach of reducing friction in bearings with spherical pivots. Michell-type bearings with line pivots and spring bed bearings do not suffer from radial tilting-stability problems and are therefore good alternatives.

Bibliography

Arghir, M., Alsayed, A. & Nicolas, D., 2002, "The finite volume solution of the Reynolds equation of lubrication with film discontinuities", International Journal of Mechanical Sciences, Vol. 44, pp. 2119-2132.

Arghir, M., Roucou, N., Helene, M. & Frene, J., 2003, "Theoretical Analysis of the incompressible Laminar Flow in a Macro-Roughness Cell", ASME Journal of Tribology, Vol. 125, pp. 309-318.

Brajdic-Mitidieri, P., Gosman, A. D., Ioannides, E. & Spikes, H. A., 2005, "CFD Analysis of a Low Friction Pocketed Pad Bearing", ASME Journal of Tribology, Vol. 127, pp. 803-812.

Braun, M. J. & Dzodzo, M., 1995, "Effects of the Feedline and the Hydrostatic Pocket Depth on the Flow Pattern and Pressure Distribution", ASME Journal of Tribology, Vol.117, pp. 224-233.

Capitao, J.W., 1974, "Influence of Turbulence on Performance Characteristics of the Tilting Pad Thrust Bearing", ASME Journal of Lubrication Technology, January, pp. 110-117.

Dobrica, M. B. & Fillon, M., 2006, "Thermohydrodynamic Behavior of a Slider Pocket bearing", ASME Journal of Tribology, Vol. 128, pp. 312-318.

Dowson, D., 1962, "A Generalized Reynolds Equation for Fluid-film Lubrication", Int. Journal of Mechanical Science, Vol. 4, pp. 159-170.

Etsion, I. & Klingerman, Y., 1999, "Analytical and Experimental Investigation of Laser-Textured Mechanical Seal Faces", Tribology Transactions, Vol. 42, No. 3, pp. 511-516.

Etsion, I., Halperin, G., Brizmer, V. & Klingerman, Y., 2004, "Experimental investigation of laser textured parallel thrust bearings", Tribology Letters, Vol. 17, No. 2, pp. 295-300.

Ettles, C. M., 1976, "The Development of a Generalized Computer Analysis for Sector Shaped Tilting Pad Thrust Bearings", ASLE Transactions, Vol. 19, 2, pp. 153-163.

Ettles, C. M. & Donoghue, J. P., 1971, "Laminar Recess Flow in Liquid Hydrostatic Bearings", Proc. Instn Mech Engers, Vol. C27/71, pp. 215-227.

Ettles, C. M., 1980, "Size Effects in Tilting Pad Thrust Bearings", Wear, 59 , pp. 231-245.

Ettles, C. M., 1991, "Some Factors Affecting the Design of Spring Supported Thrust Bearings in Hydroelectric Generators", ASME Journal of Tribology, Vol. 113, No. 3, pp. 626-632.

Ettles, C. M. & Anderson, H. G., 1991, "Three-Dimensional Thermoelastic Solutions of Thrust Bearings Using Code Marmac 1", ASME Journal of Tribology, Vol. 113, No. 2, pp. 405-412.

Fuerst, A. , 2003, "Simulation von Traglagern mit Weißmetal- und Polymerbeschichtung", SIRM 2003, Schwingungen in rotierenden Maschinen, ISBN 3-528-03956-6, Seite 11-20

Fust, A., 1981, "Dreidimensionale thermohydronamische Berechnung von Axialgleitlagern mit punktörmig abgestützten Segmenten", Dissertation, Eidgenössischen Technischen Hochschule Zürich.

Glavatskikh, S. B., 2000, "On the Hydrodynamic Lubrication in Tilting Pad Thrust Bearings", Doctoral thesis, Luleå University of Technology.

Glavatskikh, S. B., 2001, "Steady State Performance Characteristics of a Tilting Pad Thrust Bearing", ASME Journal of Tribology, Vol. 123, pp. 608-615.

Glavatskikh, S. B., Fillon, M. & Larsson, R., 2002, "The Significance of Oil Thermal Properties on the Performance of Tilting-Pad Thrust Bearings", ASME Journal of Tribology, Vol. 124, pp. 377-385.

Glavatskikh, S. B., McCarthy, D. M. C. & Sherrington, I., 2005, "Hydrodynamic Performance of a Thrust bearing with Micropatterned Pads", Tribology Transactions, Vol. 48, pp. 392-498.

Gould, P. L., 1988, "Analysis of Shells and Plates", Springer-Verlag, pp. 272-289.

Hamrock, B. J., Schmid, S. R. & Jacobson, B. O., 2004, "Fundamentals of Fluid Film Lubrication, Second Edition", Marcel Dekker, Inc., p. 97.

Hashimoto, H., 1990, "Performance Characteristic Analysis of Sector-Shaped Pad Thrust Bearings in Turbulent Inertial Flow Regime Under Three Types of Lubrication Conditions", ASME Journal of Tribology, Vol.112, No.3, pp.477-485.

Heckelman, D. & Ettles, C. M., 1987, "Viscous and Inertial Pressure Effects at the Inlet to a Bearing Film", STLE Transactions, Vol. 31, No. 1, pp. 1-5.

Heinrichson, N. & Santos, I. F., 2005, "Comparison of Models for the Steady-State Analysis of Tilting-Pad Thrust Bearings", Proc. 18th Int. Congr. of Mech. Engin. (COBEM 2005), Ouro Preto, Brazil, Nov 6-11, 2005

Heinrichson, N. & Santos, I. F., 2005, "Optimal Design of Tilting-Pad Thrust Bearings with High Pressure Injection Pockets", Proc. 12th Nordic Symposium in Tribology (Nordtrib 2006), Elsinore, Denmark, June 7-9, 2006 , NT2006-10-51.

Heinrichson, N., Santos, I. F. & Fuerst, A., 2006, "The Influence of Injection Pockets on the Performance of Tilting-Pad Thrust Bearings: Part I - Theory", Proc. 8th Biennial ASME Conference on Engineering Systems Design and Analysis, Turin, Italy, July 4-6, 2006, ESDA2006-95285. (Accepted for publication in ASME Journal of Tribology.)

Heinrichson, N., Fuerst, A. & Santos, I.F., 2006, "The Influence of Injection Pockets on the Performance of Tilting-Pad Thrust Bearings: Part II - Comparison Between Theory and Experiment", Proc. 8th Biennial ASME Conference on Engineering Systems Design and Analysis, Turin, Italy, July 4-6, 2006, ESDA2006-95287. (Accepted for publication in ASME Journal of Tribology.)

Heinrichson, N. & Santos, I. F., 2006, "Reducing Friction in Tilting-Pad Bearings by the use of Enclosed Recesses", (Accepted for publication in ASME Journal of Tribology.)

Helene, M., Arghir, M. & Frene, J., 2003, "Numerical Study of the Pressure Pattern in a Two-Dimensional Hybrid Journal bearing recess, Laminar, and Turbulent Flow results", ASME Journal of Tribology, Vol. 125, pp. 283-290.

Hemmi, M. & Inoue, T., 1999, "The Behavior of the Centrally Pivoted Thrust Bearing Pad With Hydrostatic Recesses Pressurized by a Constant-Rate Flow", Tribology Transactions, Vol. 42, No. 4, pp. 907-911.

Heshmat, H. & Pinkus, O., 1986, "Mixing Inlet Temperatures in Hydrodynamic Bearings", ASME Journal of Tribology, Vol. 108, April, pp. 231-248.

Huebner, H. , 1974, "Solutions for Pressure and Temperature in Thrust Bearings Operating in the Thermohydrodynamic Turbulent Regime", ASME Journal of Lubrication Technology, January, pp. 58-68.

Huebner, H. , 1974, "A Three-Dimensional Thermohydrodynamic analysis of Sector Thrust Bearings", ASLE Transactions, Vol. 17, October, pp. 62-73.

Jeng, M., Zhou, G.R. and Szeri A.Z., 1986, "A Thermohydrodynamic Solution of Pivoted Thrust pads: Part I - Theory", ASME Journal of Tribology, Vol.108, No.2, pp.195-207.

Kays, W. M. & Crawford, M. E., 1993, "Convective Heat and Mass Transfer, Third Edition", McGraw-Hill, Inc..

Kim, J. S. & Kim, J. S., 2002, "Effect of Distance Between Pads on th Inlet Pressure Build-Up on Pad Bearings", ASME Journal of Tribology, Vol. 124, pp. 506-514.

Kim, K. W., Tanaka, M. & Hori, Y., 1983, "A Three-Dimensional Analysis of Thermohydrodynamic Performance of Sector-Shaped, Tilting-Pad Thrust Bearings", ASME Journal of Lubrication Technology, Vol. 105, No. 3, pp. 406-413.

Mahieux, C. A. , 2005, "Experimental Characterization of the Influence of Coating Materials on the Hydrodynamic Behavior of Thrust Bearings: A Comparison of Babbitt, PTFE, and PFA", ASME Journal of Tribology, Vol. 127, No. 3, pp. 568-574.

Mikula, A. M. & Gregory, R. S., 1983, "A comparison of Tilting-Pad Thrust Bearing Lubricant Supply Methods", ASME Journal of Lubrication Technology, Vol. 105, January, pp. 39-47.

Mikula, A. M., 1988, "Further Test Results of the Leading-Edge-Groove (LEG) Tilting Pad Thrust Bearing", ASME Journal of Tribology, Vol. 110, January, pp. 174-1988.

New, N. H. , 1974, "Experimental Comparison of Flooded, Directed, and Inlet Orifice Type of Lubrication for a Tilting Pad Thrust Bearing", ASME Journal of Lubrication Technology, January 1974, pp. 22-27.

Pistner, C. A., 1996, "Some Effects of Start-Up Transient Loads on Shoe Bearings for Large Hydraulic Pump/Turbines", Tribology Transactions, Vol. 39, No. 1, pp. 93-98.

Raimondi, A. A. & Boyd, J., 1955, "Applying Bearing Theory to the Analysis and Design of Pad-Type Bearings", ASME Transactions, Vol. 77, No. 3, pp. 287-309.

Reynolds, D., 1886, "On the Theory of Lubrication and Its Application to Mr. Beauchamp Tower's Experiments, Including an Experimental Determination of the Viscosity of Olive Oil", Philosophical Transactions of the Royal Society of London, Vol. 177, pp. 157-234.

Rhim, J., & Tichy, J. A., 1989, "Entrance and Inertia Effects in a Slider Bearing", Tribology Transactions, Vol. 32, No. 4, pp. 469-379.

San Andrés, L., 1995, "Bulk-Flow Analysis of Hybrid Thrust Bearings for Process Fluid Applications", ASME Journal of Tribology, Vol. 122, pp. 170-180.

Santos, I. F. & Fuerst, A., 2003, "Große Axiallager mit Hybridschmierung - Theoretische und experimentelle Betrachtungen", Schwingungen in Rotierenden Maschinen, Vol. 6, pp. 51-60.

Santos, I. F. & Nicoletti, R., 1999, "THD Analysis in Tilting-Pad Journal Bearings Using Multiple Orifice Hybrid Lubrication", ASME Journal of Tribology, Vol. 121, pp. 892-900.

Shinkle, J. N. & Hornung, K. G., 1965, "Frictional Characteristics of Liquid Hydrostatic Journal Bearings", ASME Journal of Basic Engineering, Vol. 87, Issue 1, pp. 163-169.

Sternlicht, B., Carter, G., and Arwas, E.B., 1961, "Adiabatic Analysis of Elastic, Centrally Pivoted, Sector, Thrust-Bearing Pads" ASME Journal of Applied Mechanics, Vol.28, June, pp.179-187.

Sternlicht, B. & Arwas, E.B., 1962, "New Charts Simplify Design of Pivoted Thrust Bearings" Product Engineering, Vol. 33, Issue 8, pp. 124-132.

Vohr, J. H., 1981, "Prediction of Operating Temperature of Thrust Bearings", ASME Journal of Lubrication Technology, Vol. 103, No. 1, pp. 97-106.

Yuan, J. H., Medley, J. B. & Ferguson, J. H., 2001, "Spring-Supported Thrust Bearings Used in Hydroelectric generators: Comparison of Experimental Data with Numerical Predictions", Tribology Transactions, Vol. 44, No. 1, pp. 27-34.

-oOo-